Advanced Diagnostics for Lithium-ion Batteries: Decoding the Information in Electrode Swelling

by

Peyman Mohtat

A dissertation submitted in partial fulfillment
of the requirements for the degree of
Doctor of Philosophy
(Mechanical Engineering)
in the University of Michigan
2021

Doctoral Committee:

Professor Anna Stefanopoulou, Co-chair
Associate Research Scientist Jason Siegel, Co-chair
Assistant Professor Al-Thaddeus Avestruz
Professor Bogdan Epureanu

Peyman Mohtat
pmohtat@umich.edu
ORCID iD: 0000-0003-4881-1745

DEDICATION

To my loving family for their unconditional love and support.

ACKNOWLEDGMENTS

I would like to thank my Ph.D. co-advisor Professor Anna G. Stefanopoulou, for all her support and guidance throughout my graduate studies. I have learned a great deal from her vast experience and expertise. I would like to thank my Ph.D. co-advisor Dr. Jason Siegel for helping me build my scientific and experimental skills. His knowledge in the domain of battery behavior and controls is immense. I want to thank my committee members, Prof. Al-Thaddeus Avestruz and Prof. Bogdan Epureanu, for their critical feedback and insightful comments.

My work on this project was made possible because of the intellectual and financial help from the Automotive Research Center in accordance with Cooperative Agreement W56HZV-14-2-0001 with the U.S. Army GVSC. I would also like to acknowledge funding from the National Science Foundation under Grant No. 1762247.

It has been a pleasure working with all of my present and past colleagues in the Powertrain and Battery Controls Lab. Special thanks go to Dr. Shankar Mohan, Dr. Suhak Lee, and Dr. Valentin Sulzer. We spent countless hours working on deadlines, brainstorming, and exploring different ideas.

Thank you to all my friends in Ann Arbor and Chicago for making this such a wonderful and fulfilling journey. Special thanks go to Amir Mohtat and Sepideh Asadi.

Last but not least, I would like to dedicate this thesis to my loving family. My mother, Masi, and my father, Bahman, for believing in me and teaching me the value of learning and hard work, and my sister, Yasaman, for their never-ending support.

TABLE OF CONTENTS

CHAPTER

LIST OF FIGURES

FIGURE

LIST OF TABLES

TABLE

ABSTRACT

Lithium-ion batteries exhibit mechanical expansion and contraction during cycling, consisting of a reversible intercalation-induced expansion and an irreversible expansion as the battery ages. Prior experimental studies have shown that mechanical expansion contains valuable information that correlates strongly with cell aging. However, a number of fundamental questions remain on the usability of the expansion measurement in practice. For example, it is necessary to determine whether the expansion measurements provide information that can help the estimation of the electrode state of health (eSOH), given limits on data availability and sensor noise in the field. Furthermore, the viability of using expansion for cell diagnostics also needs more investigation considering the broad range of aging conditions in real-world applications.

This dissertation focuses on the experimental and modeling study of the expansion measurements during aging in order to assess its ability in helping battery diagnostics. To this end, mechanistic voltage and expansion models based on the underlying physics of phase transitions are developed. For the first time, the identifiability of eSOH parameters is explored by incorporating the expansion/force measurement. It is shown that the expansion measurements enhance the estimation of eSOH parameters, especially with a limited data window, since it has a better signal-to-noise ratio compared to the voltage. Moreover, the increased identifiability is closely related to the phase transitions in the electrodes.

A long-term experimental aging study of the expansion of the graphite/NMC pouch cells is conducted under a variety of conditions such as temperature, charging rate, and depth of discharge. The goals here are to validate the results of the identifiability analysis and record the reversible and irreversible expansion correlated with capacity loss for informing the electrochemical models. Firstly, the advantages of the expansion concerning the eSOH identifiability are confirmed. Sec-

ondly, the results of the expansion evolution reveal that the features in the reversible expansion are an excellent indicator of health and, specifically, capacity retention. The expansion feature is robust to charge conditions. Namely, it is mostly insensitive to the hysteresis effects of the various initial state of charge, and it is detectable at higher C-rates up to 1C. Additionally, the expansion feature occurs near the half-charged point and therefore diagnostics can be performed more often during naturalistic use cases. Thus, the expansion measurement facilitates more frequent capacity checks in the field.

Furthermore, an electrochemical and expansion model suitable for model-based estimation is developed. In particular, a multi-particle modeling approach for the graphite electrode is considered. It is demonstrated that the new model is able to capture the peak smoothing effect observed in the differential voltage at higher C-rates above C/2. Model parameters are identified using experimental data from the graphite/NMC pouch cell. The proposed model produces an excellent fit for the observed electric and mechanical swelling response of the cells and could enable physics-based data-driven degradation studies at practical charging rates.

Finally, a fast-charging method based on the constant current constant voltage (CC-CV) charging scheme, called CC-CV$\eta\sigma$T (VEST), is developed. The new approach is simpler to implement and can be used with any model to impose varying levels of constraints on variables pertinent to degradation, such as plating potential and mechanical stress. The capabilities of the new CC-CV$\eta\sigma$T charging are demonstrated using the physics-based model developed in this dissertation.

CHAPTER 1

Introduction

1.1 Background and Motivation

The automotive industry is currently in a transition from conventional internal combustion power-train systems, to electrified power-train systems, that could bring millions of battery electric vehicles (BEV) on the road by the end of the decade. This fundamental transition is spurred by the scientific consensus that in order to avoid a global warming of greater than 1.5°C by the year 2030, the amount of greenhouse gas (GHG) emissions has to reduce substantially [9]. Therefore, as the transportation sector accounts for the largest portion (28%) of total anthropogenic U.S. GHG emissions [1] (see Figure 1.1), automakers have made a significant effort and research in the past decades on the development of BEVs to reduce the amount of tailpipe GHG emissions. In recent years, advancement in battery and electric motor technologies has enabled the vehicle manufacturers to commercially introduce BEVs to the market.

As a result, the BEV's market share has expanded greatly, and globally the BEV's stock has grown to over 7 millions from 2010 to 2019 [2], as can be seen in Figure 1.2 (a). It is expected that BEVs reach cost parity with internal combustion engine vehicles (ICEV) in the next ten years [10]. Reaching cost parity relies heavily on the ongoing decline of battery-pack costs to well under $\$100/kWh$ and also the rise of resale value of BEVs by 25%. It is projected that the number of BEVs would exceed 140 millions by the year 2030 assuming cost parity is reached under current policies. However, as can be seen in Figure 1.2 (b) the projected growth is not sufficient to meet the carbon emission goals of 2030. In order to achieve the 2030 sustainability goals (to avoid a global warming of greater than 1.5°C), the number of electric vehicles has to increase from the baseline projection. Therefore, a consorted effort is needed to increase the adoption rate of BEVs to even a greater pace.

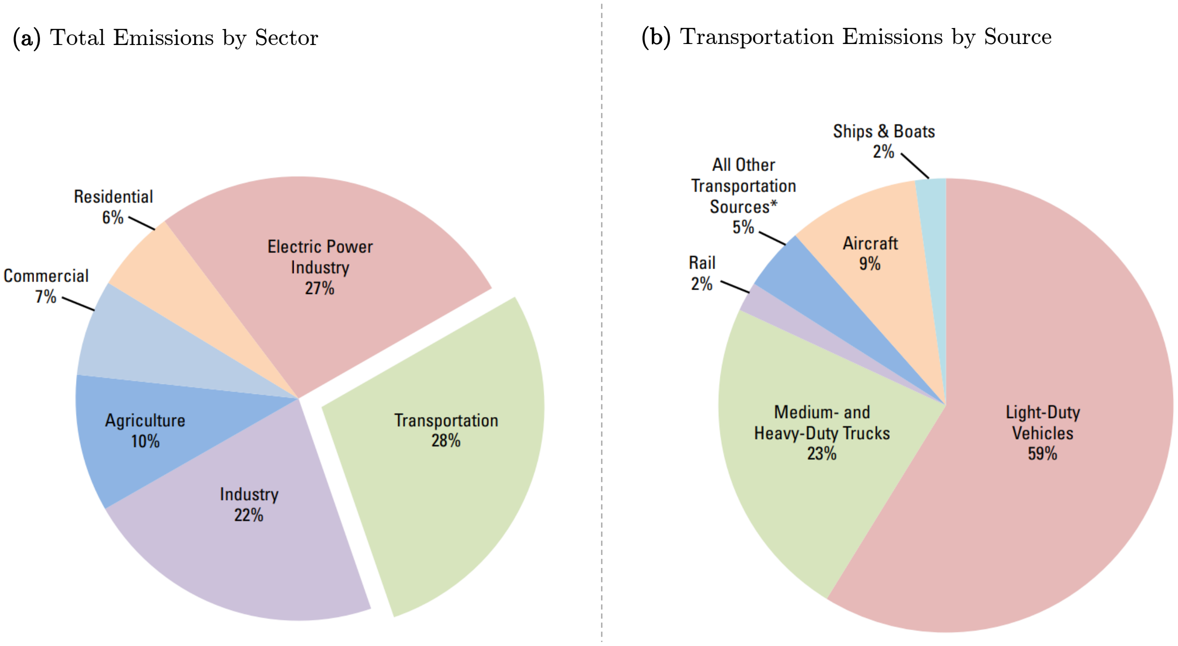

Figure 1.1: a) The U.S. greenhouse gas (GHG) emissions by sector, and b) U.S. transportation sector GHG emissions by source. Note that transportation accounts for the largest portion (28%) of total U.S. GHG emissions, furthermore, the light, medium, and heavy duty vehicles account for 82% of the transportation sector emissions [1].

To make BEVs more mainstream, not only they need to achieve cost parity with ICEV, but they also need to overcome several other barriers. First, the battery lifetime needs to increase from today's 5-7 year to 10-15 years. This is a major concern for individuals and fleet operators, as replacing battery packs is very costly. Additionally, increasing the battery lifetime also reduces the cost of ownership since it can increase the resale value of the car. Furthermore, there is an increased interest in considering a second life for such batteries as energy storage on the larger electrical grid. Re-purposing battery packs when they no longer meet the performance requirements in vehicles, has economical and environmental benefits that can be passed to consumers as cost saving [11].

Second, consumer preference motivates development of technologies that support fast charging of EVs, meanwhile, current fast-charging technology and infrastructure needs to improve considerably. Reducing lithium-ion batteries' charging time is one of the main barriers to making electric vehicles more accessible and appealing to a wide range of the population. A full charge under 12 minutes can alleviate people's concerns with limited access to charging at-home or work. Furthermore, with the widespread availability of fast charging and algorithms to mitigate degradation, it is also possible to reduce the battery pack size and, in return, reduce the cost of electric vehicles. And, third, ensuring a high level of safety for BEVs can improve consumer confidence. The safety is especially important considering with longer life and fast charging, lithium-ion batteries inevitably face larger degrees of degradation.

In order to achieve the benchmarks mentioned above, battery scientists are actively researching and developing in the areas of materials, cell design and structure, and control and estimation. Although the majority of these efforts are rightly focused on discovery of new materials and cell designs, control and estimation methods also play a crucial role in development of existing and future battery technologies. The focus area of this thesis is on modeling, estimation, and management of batteries by taking advantage of novel cell expansion measurements to allow for better and efficient utilization of these devices.

1.1.1 Battery Fundamentals

In a typical Li-ion battery, the porous electrodes consist of active material, in the form of particles, and a polymeric binder. The electrodes are attached to current collectors. Furthermore, the separator is a porous polymer, and the cell is filled up with the electrolyte.

In the discharging process lithium ions oxidized at the positive electrode (cathode) and reduced at the negative electrode (anode). The term cathode and anode refers to the electrode where oxidation and reduction happens, respectively. However, this takes place reversely while charging; the positive electrode is the anode, and the negative electrode is the cathode. Therefore, to avoid confusion in this thesis, the terms negative and positive electrode are used.

(a) Global electric car stock

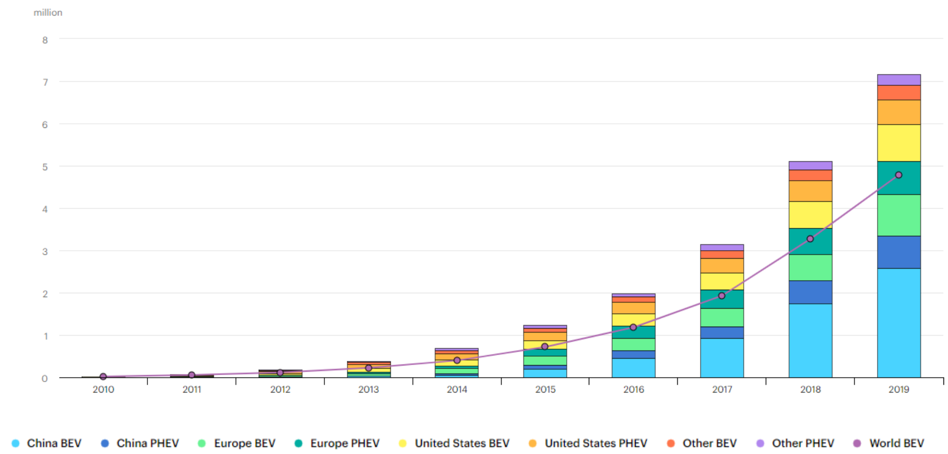

(b) Global electric car stock projected

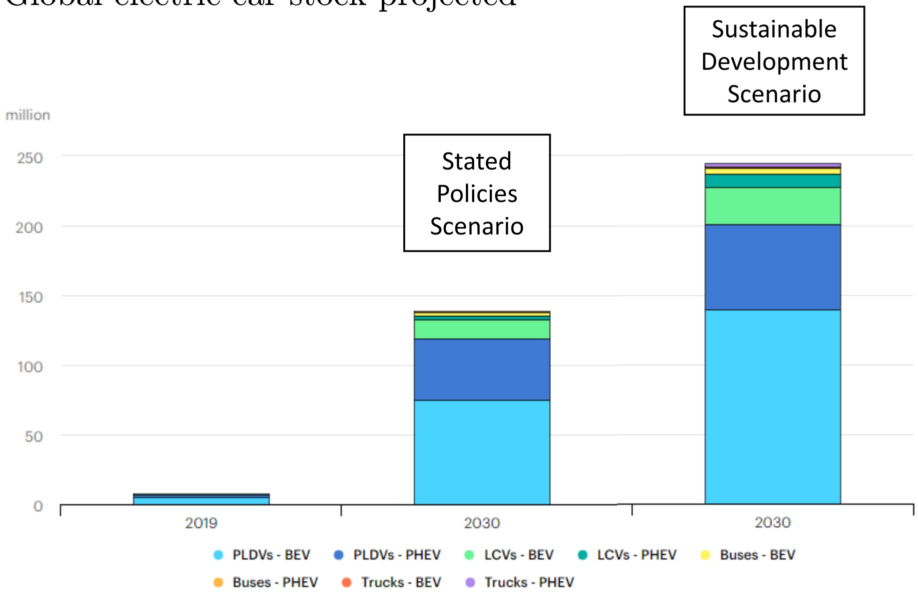

Figure 1.2: a) Global electric vehicle stock. b) Global long-term electric vehicle stock projection for the year 2030, first assuming with current policies and second assuming the sustainable development goals to avoid a global warming of greater than 1.5°C by 2030 [2].

For a Li-ion battery with graphite as the negative electrode and a lithium metal oxide (e.g. iron phosphate) as the positive electrode, while the cell is charging or discharging the following chemical reactions take place at the negative and positive electrodes, respectively

$$\mathrm{Li}_x\mathrm{C}_6 \underset{\mathrm{c}}{\overset{\mathrm{d}}{\rightleftharpoons}} \mathrm{xLi}^+ + \mathrm{xe}^- + \mathrm{C}_6$$

$$\mathrm{Li}_y\mathrm{MO}_2 + \text{(1-y)}\mathrm{Li}^+ + \text{(1-y)}\mathrm{e}^- \underset{\mathrm{c}}{\overset{\mathrm{d}}{\rightleftharpoons}} \mathrm{LiMO}_2,$$

where the forward direction indicates the discharging reactions and the backward direction indicates the charging reactions. This process is depicted in Figure 1.3 with the red arrow denoting the charging and blue arrow denoting the discharging. The stoichiometric state x and y represent the degree of lithiation of each electrode. For example, the fully lithiated state of the graphite is $x = 1$ for Li_xC_6; i.e., one lithium atom per six carbon atoms.

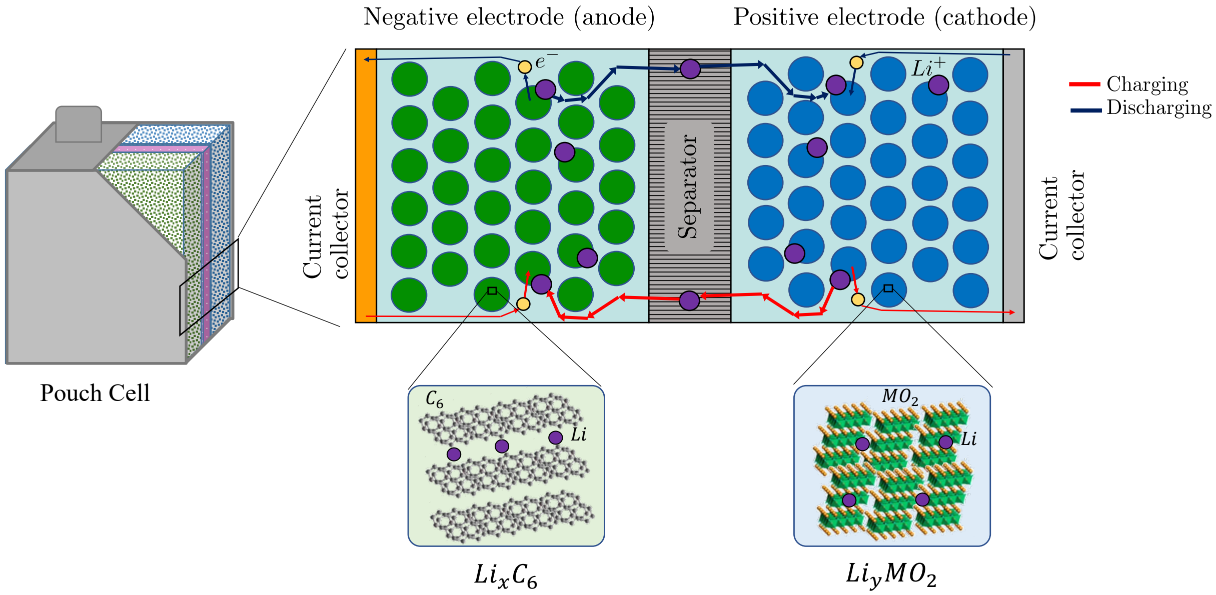

Figure 1.3: Schematic of the charging and discharging process of a lithium-ion battery.

1.1.2 Battery Degradation

There are a number of important degradation mechanisms for lithium-ion batteries [12]. Solid Electrolyte Interphase (SEI) growth and lithium plating consume the reversible lithium during cycling leading to capacity fade. Other important mechanisms are structural disordering, metal dissolution, the loss of electrical contact, particle cracking, and blockage of active materials by the resistive surface film all leading to active material of the electrode becoming unavailable for insertion and extraction of lithium, and ultimately capacity reduction [13, 14].

Due to a complex inter-correlations of these degradation mechanisms, it is extremely challenging to develop a diagnostic algorithm to classify and quantify all of them in the cell. However, it is possible to separate the effects of the mechanisms into two general modes of Loss of Lithium Inventory (LLI) and Loss of Active Material (LAM) at the positive and negative electrodes. Dubarry, et al. [15], further categorized LAM under the consideration of the LAM happening during lithiation or delithiation. Furthermore, LLI is also divided into two subcategories during; (1) charging in the negative electrode, and (2) discharging in the positive electrode. As a result of these aging modes the capacity fades, the utilization window changes, and available capacity of each electrode also decreases.

1.1.3 Expansion and Advanced Diagnostics

In state-of-the-art battery management systems, the battery state of health (SOH) is estimated by determining capacity (cyclable energy) and cell resistance (power capability). The capacity is defined by the coulombs (=Amperes*time) that can be shuttled in a battery while operating within an acceptable voltage range. The capacity can be quantified by full charge-discharge that takes time, and it is rarely feasible in real-world operations. Many studies are concerned with estimating the capacity without the need for a full discharge [16]. Several techniques to estimate capacity involve parametric estimation simultaneously with state of charge (SOC) estimation using terminal voltage measurements and coulomb counting [17, 18, 19]. Recently it was clarified that these algorithms converge to the true capacity value when the operation straddles the graphite phase transitions [20, 8]. These are the same phase transitions observed in the differential voltage (DV) analysis [21] and incremental capacity (IC) analysis [22] that are used mostly in the laboratory as effective tools for estimating SOH. These methods track the peaks observed in the derivative of the voltage with respect to the capacity during aging, and they can be done when the battery is charging under a constant low current, which avoids the confounding influence of impedance. The DV peaks can also provide information about the anode capacity and stoichiometric utilization window [23].

These methods estimate capacity based on voltage, current, and temperature measurements. However, the voltage limits alone may not be enough for managing a battery safely, since the limits may come from the anode SOH during charging and cathode SOH during discharging. For example, irreversible lithium plating, which usually happens at low temperatures or fast charging, causes LLI [15] and reduction of available capacity. The probability of lithium plating is directly connected to lithiation state of graphite at the end of charge. Lithium plating is a major safety risk as it may lead to an internal short circuit. Hence, this is a safety limit coming from anode SOH, which needs to be considered. There are a number of studies on identifying aging mechanisms using an underlying model with voltage and current measurements [24, 25, 14, 26]. However, it has been shown that aging mechanisms are weakly detectable using terminal voltage-based estimation [27, 13]. Furthermore, all these methods require full range voltage data from the open circuit (OC) state or pseudo-OC state, at a very low current rate. This is a major limitation in practice because a slow charge from a high depth of discharge is not possible in many applications (e.g. plug-in hybrid electric vehicles), and inconvenient for consumers in most cases.

Ideally we need more robust algorithms that enable the estimation of aging mechanisms during normal or even fast charging. Another interesting and important type of battery response is the mechanical response. Batteries expand as charging and contract while discharging. This response has been observed and investigated using in-situ X-ray diffraction (XRD) [28, 29] and neutron imaging techniques [30]. The mechanical response consists of a reversible expansion caused by (de)intercalation of lithium during charge-discharge [31] and irreversible expansion caused by the growth of the SEI layer, lithium plating [32], and gas generation [33]. For example, it has been shown that measuring the thickness changes with laser scanning can be a powerful tool for detecting lithium plating [34] and local aging [35]. Although the idea of using stress/strain measurements to identifying aging mechanisms, such as lithium plating [36], has been proposed, questions remain on the usefulness of this measurement. For example, given the fundamental relationship between voltage and strain [37], does the stress/strain give additional information, not available in voltage, about the battery's state. Furthermore, given limits on data availability and sensor noise is using stress/strain beneficial for observability of the aging mechanisms. Recently, the effects of mechanical conditions on aging have attracted attention with the aim of understanding and predicting the cell deformation as a function of SOC [38, 39] and SOH [40, 41].

The relationship between the evolution of capacity fade, cell thickness, and effects of the external pressure on aging and cell performance has been the subject of a number of studies [42, 43, 44, 45, 46]. However, measurement of the irreversible expansion on-board a vehicle is prone to external disturbances that can cause significant errors in a long time, such as changes in ambient temperature and changes in the pack structural rigidity. On the other hand, characterizing expansion as a differential signal is less sensitive to these external disturbances. The graphite phase transitions are also observable as peaks in the second differential of the expansion. This connection was first reported and explained in [47]. Moreover, the differential expansion (DE) signal has the advantage of better peak observability at higher C-rates [48]. Therefore, the DE can be used to develop SOH estimation methods, either by itself or in conjunction with voltage, to increase the accuracy and robustness.

1.1.4 Physics-based Expansion Modeling

To understand the electrical and mechanical response, and ultimately enable the estimation of aging mechanisms during normal or even fast charging, it is necessary to develop a mathematical model. Phenomenological voltage and mechanical models for batteries have been developed previously [38, 49], usually by applying equivalent circuit models (ECM). However, it can be shown that ECMs are unable to capture the smoothing effect in the voltage response. Hence, higher fidelity models are needed in this case. One approach is a physics-based model. Such models provide a deeper understanding into the mechanical-chemical processes inside the cell. There are number of electro-mechanical-chemical models developed for batteries [50, 51, 52]. However, most of these model are too complex to be useful for creating model-based estimators, mainly because of their high computation cost, therefore, simplified electrochemical models, such as the single particle model (SPM) [53] and the single particle model with electrolyte (SPMe) are used instead [54, 55]. Unfortunately, the SPMe is also not able to capture the smoothing dynamics of differential voltage at high charging rates. Therefore, development of alternative reduced order models is needed.

1.1.5 Fast Charging

Reducing lithium-ion batteries' charging time is one of the main barriers to making electric vehicles more accessible and appealing to a wide range of the population. Unfortunately, lithium-ion batteries degrade much faster [56] at higher C-rates needed for fast charging. The accelerated aging is primarily caused by an increased amount of lithium plating and higher mechanical stress. Irreversible lithium plating consumes lithium and decreases the capacity. Moreover, a large amount of plated lithium in the form of dendrites is a serious safety concern for the battery as it can lead to internal short circuits and fires. High currents also lead to a large concentration gradient inside the particle, which results in a great amount of mechanical stress at the particle surface. Large stresses can increase particle cracking, loss of active material, and ultimately cause a reduction in capacity. Another important degradation mechanism contributing to capacity fade is the growth of the SEI layer, which again consumes lithium inventory. This aging mechanism is largely unavoidable. However, it is widely accepted that temperature plays a significant role in the growth of the SEI. Therefore, preventing elevated temperatures can also limit the amount of SEI growth. Lastly, the degradation of the electrolyte at high voltages can also reduce the lithium-ion battery's performance and safety, which is mainly avoided by constraining the maximum voltage. At the same time, voltage limits define the cell capacity and are often prescribed by the cell manufacturer.

To reduce the degradation caused by lithium plating and stress, monitoring the plating potential and concentration distribution in the active material is needed. However, direct measurement of the variables mentioned above outside of a laboratory setting is essentially infeasible. Therefore, physics-based models are utilized instead. Many studies use models and optimization algorithms to minimize aging and charging time with a number of constraints. For example, in [57] and [58] the thermal and plating constraints are considered, and the charging problem is formulated using a nonlinear model predictive control scheme. This scheme is also utilized to minimize the aging due to SEI during fast charging in Ref. [59]. In [60], authors used simultaneous nonlinear programming approach with stress constraints on the electrode particle to develop a fast-charging algorithm. Nevertheless, the complexity of the optimization algorithm of these methods is a limiting factor for their implementation on board vehicles. The conventional way of charging batteries is to apply either a constant current (CC) or a constant power (CP) until the maximum allowable voltage is reached and then switch to a constant voltage (CV) phase until the current falls below a certain threshold. It can be shown that given a maximum current and a maximum voltage constraint, the CC-CV protocol is the fastest charging method in terms of minimizing only the charge time, for example in Ref. [61] for a Single Particle Model. Although the CC-CV protocol is easily implementable and used widely in practice, it is unaware of aging constraints discussed earlier. The CC-CV methodology has been used in Ref. [62] to develop a constant-temperature constant-voltage (CT-CV) charging technique, however, this method is also unaware of the aging constraints.

1.2 Dissertation Organization and Contributions

The main focus of this work is to study the benefits of expansion measurements for battery diagnostics. This has been done by developing models of cell expansion, long-term study of cell expansion under various stress factors, and incorporating the mechanical stress in a fast charging algorithm. The main contributions of this thesis is summarized as follows:

In the second chapter of this thesis, it is shown that using a mechanistic model with phase transitions at low charge rates the expansion/force provides better identifiability of the individual electrode parameters. It is demonstrated that this is due to a more significant signal to noise ratio of force compared to voltage. Furthermore, the results are verified by collecting and analyzing data from fresh and aged cells. As a result, with the addition of the expansion, the parameters are estimable without the need to discharge the battery to a high Depth of Discharge ($> 70\%$), which rarely happens in automotive applications. This makes eSOH estimation feasible for a wider range of real-world driving scenarios. This chapter is based on the following works,

- **Peyman Mohtat**, Suhak Lee, Jason B. Siegel, Anna G. Stefanopoulou, "*Towards better estimability of electrode-specific state of health: Decoding the cell expansion,*" Journal of Power Sources, Volume 427, pp. 101-111, 2019.
- **Peyman Mohtat**, Farinaz Nezampasandarbabi, Shankar Mohan, Jason B. Siegel, and Anna G. Stefanopoulou, "*On identifying the aging mechanisms in li-ion batteries using two points measurements,*" in American Control Conference (ACC), pp. 98–103, IEEE, 2017.

In the third chapter of the thesis, the aging data is collected and the evolution of the electrical and mechanical characteristics are documented as they are observed in the terminal voltage and mechanical measurement. The aging experiment matrix is designed with various degradation stressors, such as temperature, charging rate, and depth of discharge. The data collection campaign is very important to cover various degradation modes to extract the degradation features that will be used to inform, parameterize, and validate the electrochemical models. Moreover, all the model were calibrated to match the observed behavior while maintaining the important intrinsic shift of the phase transition of the battery material as it ages. This shift creates an "aging signature" like a wrinkle that we can observe in the measured force more clearly than in the measured voltage, especially at relevant discharge ranges and rates. This chapter is based on the following works,

- **Peyman Mohtat**, Suhak Lee, Jason B. Siegel, and Anna G. Stefanopoulou, "*Comparison of Expansion and Voltage Differential Indicators for Battery Capacity Fade,*" Journal of Power Sources, 2021.
- **Peyman Mohtat**, Suhak Lee, Jason B. Siegel, and Anna G. Stefanopoulou, "*Reversible and Irreversible Expansion of Lithium-ion Batteries Under a Wide Range of Stress Factors,*" Journal of The Electrochemical Society, 2021.

In the fourth chapter, a physics-based low-order mechanical multiple particle battery model of the coupled electro-chemical and thermo-mechanical dynamics is developed. In the differential voltage analysis (DVA) the battery's capacity is estimated by tracking the peaks observed in the differential voltage. Unfortunately, at higher C-rates (above C/2) the peaks flatten, and their locations become unobservable. Hence the capacity estimation becomes highly uncertain. The derivative of the cell expansion also include observable peaks. The peaks in the voltage derivative curve and the second derivative of the expansion curve correspond to the same phase transitions in the material. Unlike the differential voltage, the peaks are observable up to 1C rate in the differential expansion curve, which makes the differential expansion an excellent method for capacity estimation during fast charging scenarios (above C/2). The developed model is able to capture the aforementioned smoothing effect of the voltage derivative. This chapter is based on the following works,

- **Peyman Mohtat**, Suhak Lee, Valentin Sulzer, Jason B. Siegel, and Anna G. Stefanopoulou, "*Differential Expansion and Voltage Model for Li-ion Batteries at Practical Charging Rates,*" Journal of The Electrochemical Society, 167(11), p.110561, 2020.
- **Peyman Mohtat**, Jason B. Siegel, and Anna G. Stefanopoulou, "*High C-Rate Differential Expansion and Voltage Model for Li-Ion Batteries,*" in Meeting Abstracts, no. 5, pp. 434-434. The Electrochemical Society, 2019.

In the fifth chapter, a fast charging method based on the constant current constant voltage (CC-CV) charging scheme, called CC-CV$\eta\sigma$T (VEST) is presented. The new approach is simple to implement and can be used with any model to impose varying levels of constraints on variables pertinent to degradation, such as plating potential and mechanical stress. The new CC-CV$\eta\sigma$T charging is demonstraated using the electrochemical model with mechanical and thermal effects developed in the earlier chapter. This chapter is based on the following work,

- **Peyman Mohtat**, Suhak Lee, Valentin Sulzer, Jason B. Siegel, and Anna G. Stefanopoulou, "*An Algorithmic Safety VEST For Li-ion Batteries During Fast Charging,*" Modeling, Estimation and Control Conference (MECC), 2021 [In Press].

CHAPTER 2

Estimability of Electrode-specific State of Health Using Voltage and Expansion: A Fundamental Analysis

2.1 Introduction

The goal in this chapter is to study the fundamental benefits of incorporating cell expansion measurements for estimating electrode-specific State of Health (eSOH) under noisy signals and limited data range. In this chapter, individual electrode capacity and utilization window are proposed as parameters related to eSOH. Furthermore, the relationship between these parameters and aging mechanisms are introduced. It is necessary to know the usefulness of expansion before considering other difficulties associated with measurements in a realistic cell inside a pack. Hence, the model is developed using several simplifying assumptions; namely, the effects of temperature and hysteresis on voltage and expansion are omitted. However, to have a better connection to the underlying physics, fundamental electrode potential and expansion functions are developed and included in the model. The methodology for identifiability analysis is based on the Fisher information matrix which gives the Cramer-Rao bound for the estimation of eSOH parameters. Finally, the results for voltage only and voltage plus expansion measurements are obtained and compared.

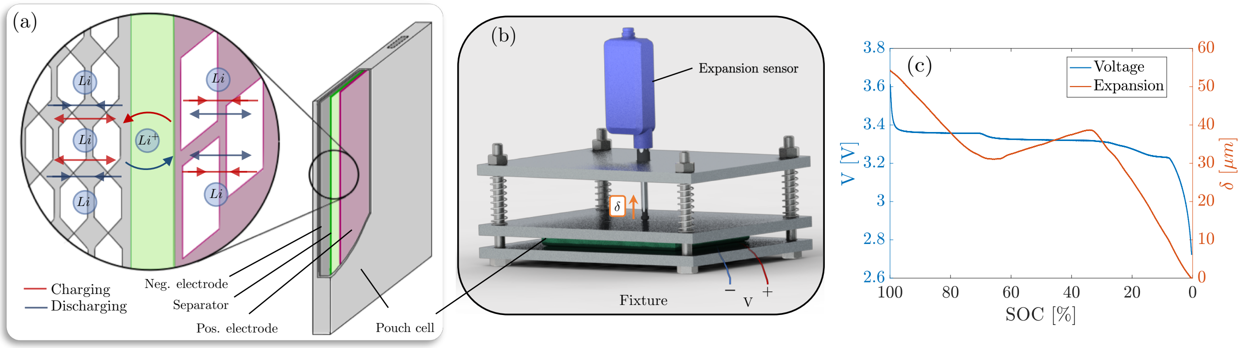

Figure 2.1: (a) The schematic drawing of the inner working of a Li-ion battery. (b) The experimental setup, and (c) the voltage and expansion result of an LFP cell vs. state of charge (SOC) at a low c-rate.

2.2 Experimental Method

The details of the pouch cell (A123) used in this chapter is shown in Table 2.3. The chemistry of the pouch cell was graphite/LFP. The process of a typical Li-ion battery is depicted in Figure 2.1(a) with the red (blue) arrow denoting the charging (discharging) and expansion (contraction) of the lattice structure. The experimental setup is shown in Figure 2.1(b). The fixture was designed such that the top and bottom plates are fixed in place while the middle plate is free moving. To avoid the non-uniformities in the expansion, the fixture applied a small pressure on the pouch cell, by using compression springs. The applied pressure was around one psi given the spring constant and displacement. Also, the spring constants were much lower than the modulus of the cell [63]. Hence, the free movement of the middle plate with the addition of these springs allowed for more uniform free expansion of the pouch cell. The expansion was measured using a displacement sensor (Keyence, Japan) mounted on the top plate. The dynamic testing was carried using a battery cycler (Biologic, France). The temperature was measured using a K-type thermocouple (Omega, USA) place on the surface of the battery.

The fixture was installed inside a climate chamber with the temperature set to 25^oC. Then the cell was cycled 10 times at C/3 between 2.5 V and 3.6 V to ensure the repeatability of the expansion data. The cell was charged with a constant current (CC) from the fully discharged state at a low rate

(C/20) to 3.6 V, followed by a constant voltage (CV) period until the current dropped below C/40, followed by a pause of 3 h. Then, the cell was discharged to 2.5 V at the same constant current. The cycle was repeated three times, and the measurements from the last cycle were reported.

2.3 Model Development

2.3.1 Aging mechanisms and eSOH

To maximize the usage without inducing further degradation, estimating the type of degradation and state of health of the individual electrodes is required. Hence, identifying the changes in individual electrode capacity and the associated shift of utilization window is important and informs the Battery Management System (BMS) about the aging mechanisms and electrode specific constraints.

The importance of eSOH estimation is clarified in Figure 2.2, using a simulated aging scenario for a graphite/LFP cell. The aging scenario corresponds to $\mathrm{LAM}_{\mathrm{deNE}}$ mode, and the methodology presented in [15] is followed when producing this figure. In this mode, the negative electrode capacity is reduced by a significant amount, which is shown by the scaling of the negative potential denoted by purple arrows. At fresh and aged states, the cell operates between the same voltage limits defined as the safe range. However, for the aged state, the utilization of graphite electrode has shifted (denoted by a green arrow) to the dangerous region of low potential which increases the risk of lithium plating (marked by a dashed red area at the bottom of graphite half-cell potential). Furthermore, it is also evident that the shift of negative electrode operation window to a low potential is obscured in the terminal voltage. In contrast, Figure 2.3 shows the effects of the same aging mechanism for the expansion of a single cell, where it suggests an observable change in the expansion of the fresh and aged cell.

In the following sections, the lithiation state of each electrode (utilization window) and the amount of available active material in each electrode (individual capacity) are introduced as eSOH parameters, using OCV and expansion. Furthermore, the equations connecting these parameters and aging mechanisms are discussed.

2.3.1.1 Open Circuit Voltage (OCV)

The OCV is the terminal voltage of a cell with no current flow, which can be written as the electrical potential difference between the positive and the negative electrodes. Let the potentials of the positive and negative electrode, measured against Lithium, as a function of y and x, be denoted by (U_p) and (U_n), respectively. Then, while the cell is at an electrical equilibrium (no current is drawn and the voltage is at steady state), the terminal voltage of the cell is equal to Open Circuit Voltage

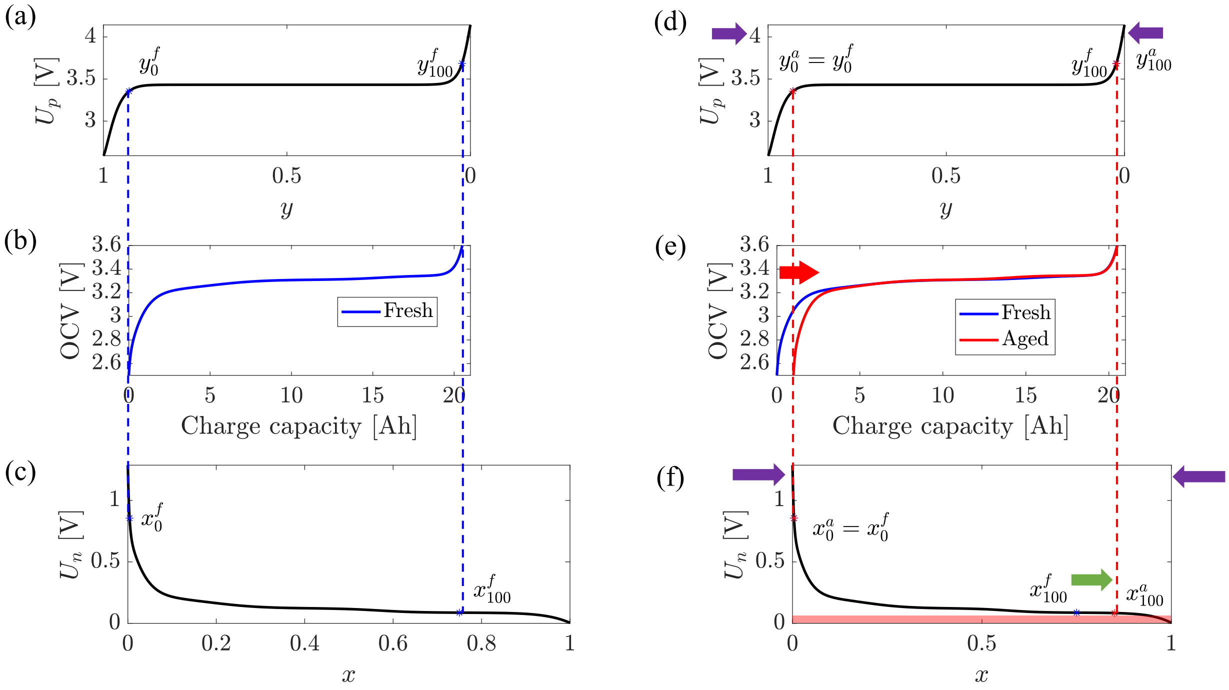

Figure 2.2: (a) The half-cell potential of the positive electrode at the fresh state. (b) The Open Circuit Voltage (OCV) of a graphite/LFP cell at the fresh state. (c) The half-cell potential of the negative electrode at the fresh state. (d) The half-cell potential of the positive electrode at the aged state. (e) The OCV at two states of life; fresh (blue) and aged (red), and (f) the negative electrode half-cell potential at the aged state with corresponding utilization window at fresh (f) and aged (a) states. The simulated degradation correspond to 28% negative electrode capacity loss which corresponds to only 5% capacity fade for aged state of cell (middle) but forces the utilization window of the negative electrode deeply in the dangerous zone of lithium plating (bottom).

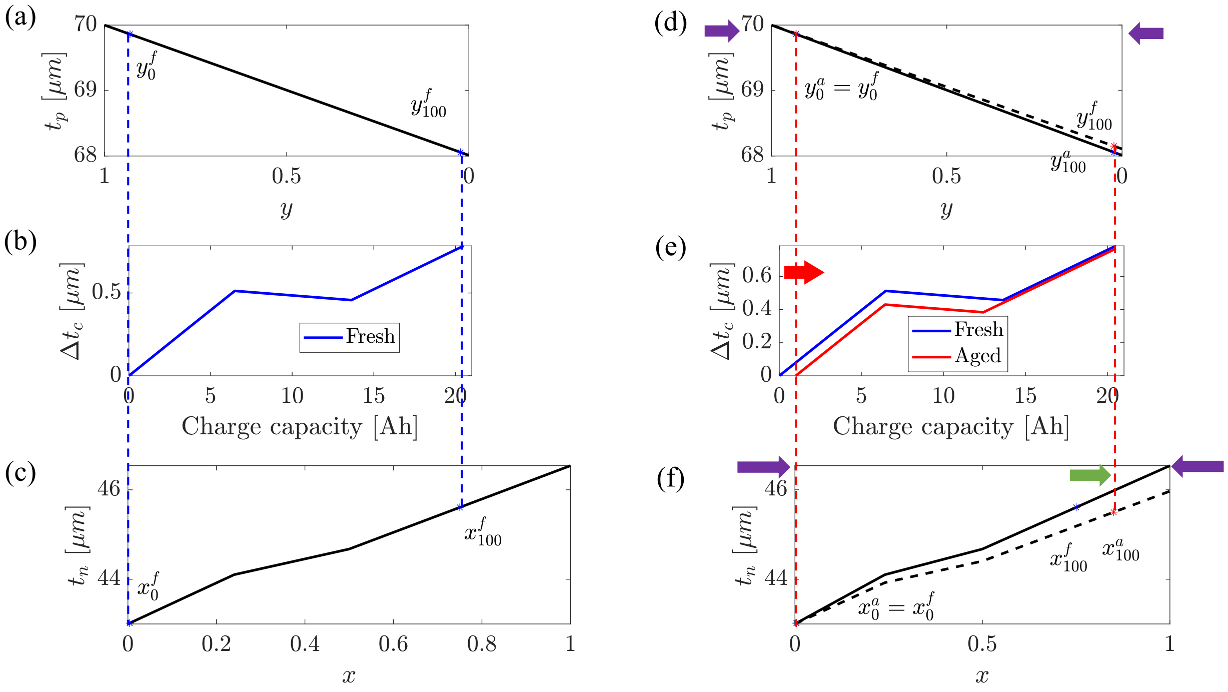

Figure 2.3: (a) The half-cell expansion of the positive electrode at the fresh state. (b) The expansion of a graphite/LFP cell at the fresh state. (c) The half-cell expansion of the negative electrode at the fresh state. (d) The half-cell expansion of the positive electrode at the aged state. The expansion at two states of life; fresh (blue) and aged (red), and (e) the negative electrode expansion at aged state with corresponding utilization window at fresh (f) and aged (a) states. The simulated degradation corresponds to 28% negative electrode capacity loss which corresponds to 5% capacity fade for the aged state of the cell. The figure suggests an observable change in the expansion of the fresh and aged cell.

(OCV) and satisfies the following

$$OCV(z) = U_p(y) - U_n(x), \tag{2.1}$$

where z is the state of charge (SOC) of the cell and x, y are the *stoichiometric state* of negative and positive electrodes, receptively.

To prevent rapid cell degradation or power depletion, x and y are not necessarily from 0 to 1 for practical cells. Hence, the term *utilization window* is introduced for each electrode to represent the actual stoichiometric range used in each electrode. The utilization window is defined using the voltage limits specified for the battery, hence

$$U_p(y_0) - U_n(x_0) = V_{min}, \tag{2.2}$$

$$U_p(y_{100}) - U_n(x_{100}) = V_{max}. \tag{2.3}$$

where 100 and 0 subscripts denote the lithiation state of electrodes at two voltage limits V_{max}, and V_{min}, respectively.

Furthermore, the stoichiometric state of each electrode, (x, y) satisfies the following relationship with z

$$z = \frac{Q}{C} = \frac{y_0 - y}{y_0 - y_{100}} = \frac{x - x_0}{x_{100} - x_0}, \tag{2.4}$$

where Q is the coulomb counting from the fully discharged state and C denotes the maximum capacity of the cell, which is defined by the voltage limits. With respect to the amount of available active material in each electrode the following equality holds

$$C = C_p(y_0 - y_{100}) = C_n(x_{100} - x_0), \tag{2.5}$$

where C_p and C_n denote the capacity of the positive and negative electrode in Amp-hours, respectively. These capacities correspond to the amount of active material in each electrode. Using Equations (2.4) and (2.5) results in the following

$$z = \frac{Q}{C} = C_p\frac{y_0 - y}{C} = C_n\frac{x - x_0}{C}. \tag{2.6}$$

Then, the individual stoichiometric states can be written as

$$y = y_0 - \frac{Q}{C_p}, \quad x = x_0 + \frac{Q}{C_n}. \tag{2.7}$$

Furthermore, the Equation (2.7) can be written as

$$y = y_{100} + \frac{C - Q}{C_p}, \quad x = x_{100} - \frac{C - Q}{C_n}. \tag{2.8}$$

Therefore, the half-cell potentials can be written as the function of the coulomb counting Q with the individual electrode parameters $(x_{100}, y_{100}, C_n, C_p)$

$$\begin{aligned} U_p(y) &= U_p\left(y_{100} + \frac{C - Q}{C_p}\right), \\ U_n(x) &= U_n\left(x_{100} - \frac{C - Q}{C_n}\right). \end{aligned} \tag{2.9}$$

In this work, the OCV measurement is approximated by a slow charge (C/20) since the overpotentials are negligible at such low currents. Finally, the OCV in Equation (2.1) as the function of the charging coulomb counting ΔQ is given by the following

$$OCV = U_p\left(y_{100} + \frac{C - Q_s - \Delta Q}{C_p}\right) - U_n\left(x_{100} - \frac{C - Q_s - \Delta Q}{C_n}\right), \tag{2.10}$$

where the eSOH parameters are utilization window and capacity of both electrodes, (x_{100}, C_n) and (y_{100}, C_p), for negative and positive electrode, respectively. Furthermore, it is assumed that the starting SOC of the cell is unknown, in case the data window is limited. Therefore, the parameter Q_s is introduced as an additional unknown parameter, which is related to the starting SOC of the cell, z_s, by the $z_s = Q_s/C$ equation.

2.3.1.2 Cell Expansion

At any given moment in time, the thickness of the cell is the sum of thicknesses of its components. Similar to open circuit potential, the thickness of the electrodes can also be measured as a function of stoichiometric state at the open circuit state. In order to model the reversible expansion, first, we need to model the volume changes of the active material particles induced by the intercalation. Second, we need to model the thickness changes of the porous electrodes induced by the expansion of all the particles, and lastly we need to model the expansion at the cell level considering all the negative and positive electrodes and inactive components like the separator. Let $(\Delta \mathcal{V}_p)$ and $(\Delta \mathcal{V}_n)$ denote the changes in volume at the particle level as a volumetric strain. The volumetric strain is a function of the stoichiometric state (y) for the positive electrode and (x) for the negative electrode.

The porous electrode, in addition to the active material, has embedded binder polymer, furthermore, the electrode is glued to the current collector whereas it has free movement on the separator side. This makes the process of going from particle to electrode expansion complicated. To simplify this process it is assumed first that because of the large electrode length to thickness ratio and high stiffness, the electrode only expands in the through-plane direction. Second, the changes in electrode thickness come only from the active material and contribution of binder and other add-ons are not considered [64]. Following these set of assumption, the electrode thickness change is given by

$$\Delta t_e^p = \frac{w_p V_{am}^p \Delta \mathcal{V}_p}{A_e^p}, \tag{2.11a}$$

$$\Delta t_e^n = \frac{w_n V_{am}^n \Delta \mathcal{V}_n}{A_e^n}, \tag{2.11b}$$

where V_{am} is the active material volume and A_e is the electrode surface area. The variable w defines the fraction of the volume changes of the particles that results in the electrode thickness changes, which depends on the porous structure of the electrode. From first principles the electrode specific capacity is given by

$$C_p = \rho_p \hat{C}_p V_{am}^p, \tag{2.12a}$$

$$C_n = \rho_n \hat{C}_n V_{am}^n, \tag{2.12b}$$

where ρ is the density and $\hat{C}$ is the specific capacity of the active material. Substituting for V_{am} in

Equations (2.11a) and (2.11b) using Equations (2.12a) and (2.12b) results in

$$\Delta t_e^p = \frac{w_p C_p \Delta \mathcal{V}_p}{A_e^p \rho_p \hat{C}_p}, \tag{2.13a}$$

$$\Delta t_e^n = \frac{w_n C_n \Delta \mathcal{V}_n}{A_e^n \rho_n \hat{C}_n}. \tag{2.13b}$$

The cell reversible expansion, t_{rev}, is equal to the summation of expansion of all electrode layers in the cell, and is written as

$$t_{rev}(z) = n_c \kappa_b (\Delta t_e^p(y) + \Delta t_e^n(x)), \tag{2.14}$$

where the number of stacked cell layer in the pouch cells is denoted by n_c and κ_b is a parameter accounting for the effects of the fixture on the expansion [48]. Utilizing Equations (2.13a) and (2.13b) results in

$$t_{rev}(z) = n_c \kappa_b \left(\alpha_p \Delta \mathcal{V}_p(y) + \alpha_n \Delta \mathcal{V}_n(x) \right), \tag{2.15}$$

where coefficients

$$\alpha_p = \frac{w_p C_p}{A_e^p \rho_p \hat{C}_p}, \tag{2.16a}$$

$$\alpha_n = \frac{w_n C_n}{A_e^n \rho_n \hat{C}_n}, \tag{2.16b}$$

are introduced for the convenience of notation.

Now, the cell thickness can be described by the following equation:

$$t_c = t_{rev} + t_{irr}. \tag{2.17}$$

The irreversible expansion denoted by t_{irr}, evolves on much longer time scale than the reversible expansion. Therefore, it is assumed that the irreversible expansion does not change during a slow charge test. Therefore, the change in the cell thickness in one cycle is given by the changes in the reversible expansion. The change in the cell thickness (i.e. the reversible expansion) with respect to the thickness at the start of charge is given by

$$\Delta t_c = t_{rev}(z) - t_{rev}(z_s), \tag{2.18}$$

where $z_s = Q_s/C$ is the starting SOC. Finally, using Equation (2.8) for stoichiometric states and Equation (2.15) for the reversible expansion, the cell thickness change is given by

$$\begin{aligned}\Delta t_c = n_c \kappa_b \Bigg[&\frac{\alpha_p C_p}{C_p^f} \left(\Delta \mathcal{V}_p \left(y_{100} + \frac{C - Q_s - \Delta Q}{C_p} \right) - \Delta \mathcal{V}_p \left(y_{100} + \frac{C - Q_s}{C_p} \right) \right) + \\ &\frac{\alpha_n C_n}{C_n^f} \left(\Delta \mathcal{V}_n \left(x_{100} - \frac{C - Q_s - \Delta Q}{C_n} \right) - \Delta \mathcal{V}_n \left(x_{100} - \frac{C - Q_s}{C_n} \right) \right) \Bigg],\end{aligned} \tag{2.19}$$

where superscript (^{f}) denotes the initial or fresh value of the electrode capacity, furthermore, it is assumed that the α_n and α_p coefficients only scale with the electrode capacity changes during aging.

2.3.1.3 Aging mechanisms diagnostics

With eSOH parameters defined in the previous sections, it is now possible to introduce the equations describing the amount of different aging mechanisms. The percentage amount of LAM in each electrode, is the reduction in available individual electrode capacity (C_p, C_n) and its given by

$$LAM_{pe}\% = \left(1 - \frac{C_p^a}{C_p^f} \right) \times 100, \quad LAM_{ne}\% = \left(1 - \frac{C_n^a}{C_n^f} \right) \times 100, \tag{2.20}$$

where the superscript f and a denote the fresh and aged state, respectively. Note that the LAM here is the overall amount of LAM of lithiation and delitiation. The amount of intercalated lithium in the electrode at any SOC is given by the following

$$n_{Li} = \frac{3600}{F}(yC_p + xC_n), \tag{2.21}$$

where F is the Faraday constant. It is straight-forward to show that the above amount is constant, assuming lithium conservation,

$$\frac{3600}{F}\left(\left(y + \frac{\Delta Q}{C_p}\right) C_p + \left(x - \frac{\Delta Q}{C_n}\right) C_n\right) = \frac{3600}{F}(yC_p + xC_n), \tag{2.22}$$

where ΔQ denotes discharging in Amp-hours. Hence, the n_{Li} can be calculated with respect to fully charged state

$$n_{Li} = \frac{3600}{F}(y_{100}C_p + x_{100}C_n). \tag{2.23}$$

Finally, the LLI is defined as the percentage reduction in the above amount

$$LLI\% = \left(1 - \frac{n^a_{Li}}{n^f_{Li}}\right) \times 100, \tag{2.24}$$

where the superscript f and a denote the fresh and aged state, respectively. LLI here denotes the total loss of lithium.

2.4 Materials with phase transitions

In this section, fundamental models of electrode potential ($U_p,\ U_n$), and particle level expansion ($\Delta\mathcal{V}_p,\ \Delta\mathcal{V}_n$) are presented. The potential is represented by approximations of the thermodynamic equilibrium potentials of the porous electrodes [65]. Furthermore, the expansion is represented by associating the expansion to the measurement changes in lattice parameters during charge/discharge. In section 2.5, it will be shown that the sensitivity matrix of OCV and expansion to the parameter is related to the slope of each electrode potential and expansion. In the following,

Electrode material	Phase coexistence	x, y range	V^0 (V)
LFP			
	$FePO_4$ & $LiFePO_4$	$0 \leq y \leq 1.0$	3.45
Graphite (C)			
	Dilute 1 & Stage 4	$0 \leq x < 0.13$	0.2
	Stage 4 & Stage 3	$0.13 \leq x < 0.24$	-
	Stage 3 & Stage 2	$0.24 \leq x < 0.5$	0.12
	Stage 2 & Stage 1	$0.5 \leq x \leq 1.0$	0.09

Table 2.1: The different phase coexistences with their plateau potential and approximate range for graphite [4] and LFP [3].

the connection between these slopes and the phase transitions of electrode material is explained for the graphite/LFP chemistry.

2.4.1 A fundamental model of the potential

A number of materials used as insertion electrode in Li-ion cells undergo different phase transitions during lithium (de)intercalation, and the potential displays several plateaus with fast changes between them, which results in the so-called ”staircase” voltage curve [66]. The plateaus correspond to the coexistence of Li-rich and Li-poor regions, where the two phases do not mix, hence the material *phase separate* into the two regions. Furthermore, the steps between the plateaus denote the boundary in which the phase transition completes.

In this study, a cell consisting of a graphite electrode and lithium iron phosphate (LFP) electrode is considered. Both of these materials display the phase separating characteristic; LFP with one vast plateau and graphite with several plateaus.

Positive electrode: Lithium iron phosphate is a cathode material gaining popularity due to its safety, low cost and relatively high rate capability and long cycle life [67]. It has a vast voltage plateau which corresponds to a strong tendency of the material to phase separate.

A simple thermodynamical model of a phase separating material is the regular solution of particles and vacancies [65]. The equation describing the chemical potential is

$$\mu(y) = \frac{\Omega}{2}(0.5 - y) + k_B T ln\left(\frac{y}{1-y}\right), \tag{2.25}$$

where Ω is the regular solution interaction parameter, k_B is the Boltzmann's constant, and T is the absolute temperature. Then the open circuit potential, U_p, measured against lithium metal as reference potential is simply,

$$U_p(y) = V^0 + \frac{\Omega}{2e}(y - 0.5) - \frac{k_B T}{e} ln\left(\frac{y}{1-y}\right), \tag{2.26}$$

where V^0 is standard potential, and e is the charge of an electron. This equation also shows that $U_p(0.5) = V^0$. For $\Omega > 2k_BT$ the material is phase separating and the chemical potential is non-monotonic. However, the actual voltage measurement is monotonic with a large flat section called the miscibility region, which is bounded by (y^-, y^+). This voltage behavior has been modeled using a multiple particle approach, which also models the voltage hysteresis of LFP. For further discussion on this subject the reader is referred to [65, 68]. The values of the bound can be find by setting the chemical potential to zero. Figure 2.4(a) shows the potential response and the concentrations bounding the plateau for LFP. Here the two phases are $FePO_4$ and $LiFePO_4$.

Inspired by the above model, a piecewise linear approximation of the potential of two phase materials (e.g. LFP) is developed. The steps are as follows:

1. The potential at the center of the plateau region, V^0, is identified (Table 2.1).
2. The concentrations bounding the plateau (y^-, y^+) are chosen empirically (Figure 2.4(a)).
3. A line is constructed on the plateau intersecting with V^0 in the (y^-, y^+) region.
4. A second line is constructed for the initial potential drop using the starting point of data, $(U_p, y) = (U_{max}, 0)$ (voltage range), and point y^- of the plateau line.
5. A third line is constructed for the end potential drop using the ending point of data, $(U_p, y) =$

$(U_{min}, 1)$ (voltage range), and point y^+ of the plateau line.

Using this methodology and data from [3], the following potential function is obtained

$$U_p(y)\ [V] = \begin{cases} -20.99y + 4.5 & y < 0.05 \\ -7e{-}06(y - 0.5) + 3.45 & 0.05 \leq y < 0.97 \\ -31.66y + 34.16 & 0.97 \leq y. \end{cases} \tag{2.27}$$

In this function the plateau boundary is $(y^-, y^+) = (0.05, 0.97)$, midpoint potential is $V^0 = 3.45\ [V]$, and potential range is $(U_{min}, U_{max}) = (2.5, 4.5)\ [V]$. The piecewise linear approximation and data from [3] are depicted in Figure 2.4(a).

Negative electrode: The graphite is used extensively as anode material. It undergoes several phase transitions in its potential response [69]. In graphite, Li intercalates between graphene planes but prefers to populate isolated layers. Each *phase* correspond to a different filling order of lithium atoms between graphene layers called a *stage*. The stage number, n, is the number of graphene layers between layers of lithium atoms with every n^{th} layer Li-rich, and the other layers Li poor.

The stages are as follows: At the very low concentrations of lithium ($x < 0.04$), the lithium atoms are randomly distributed in the graphite, and there is no apparent structure, this stage is called a dilute stage 1. As the concentration increases a more structured phase, stage 4, begins to take shape. The plateau at 200mV corresponds to dilute stage 1 and stage 4 phase transition. Next is the formation of stage 3, the transition from stage 4 to 3 happens in ($0.13 < x < 0.24$). Unlike others the phase transitions between these stages seem to be continuous, indicating a random mix of these two phases, hence there is no plateau corresponding to this phase transition. The next plateau at 120mV corresponds to stage 3 and stage 2 phase transition. Finally is the development of the densest structure, stage 1, which is one layer of graphene between layers of lithium atoms. The plateau at 90mV corresponds to stage 2 and stage 1 phase transition.

A summary of different phase transitions of graphite as well as the LFP is presented in Table 2.1, the potential of each plateau is also reported. A similar procedure to LFP is used to get a piecewise linear representation of the potential response of the graphite. The concentrations bounding the plateaus are indicated in Figure 2.4(b). Furthermore, the potential range is $(U_{min}, U_{max}) = (0, 0.5)$ $[V]$. As indicated in Table 2.1, the stage 4 to 3 transition does not produce a plateau [4], therefore, is approximated with a line. Using this methodology and potential data for

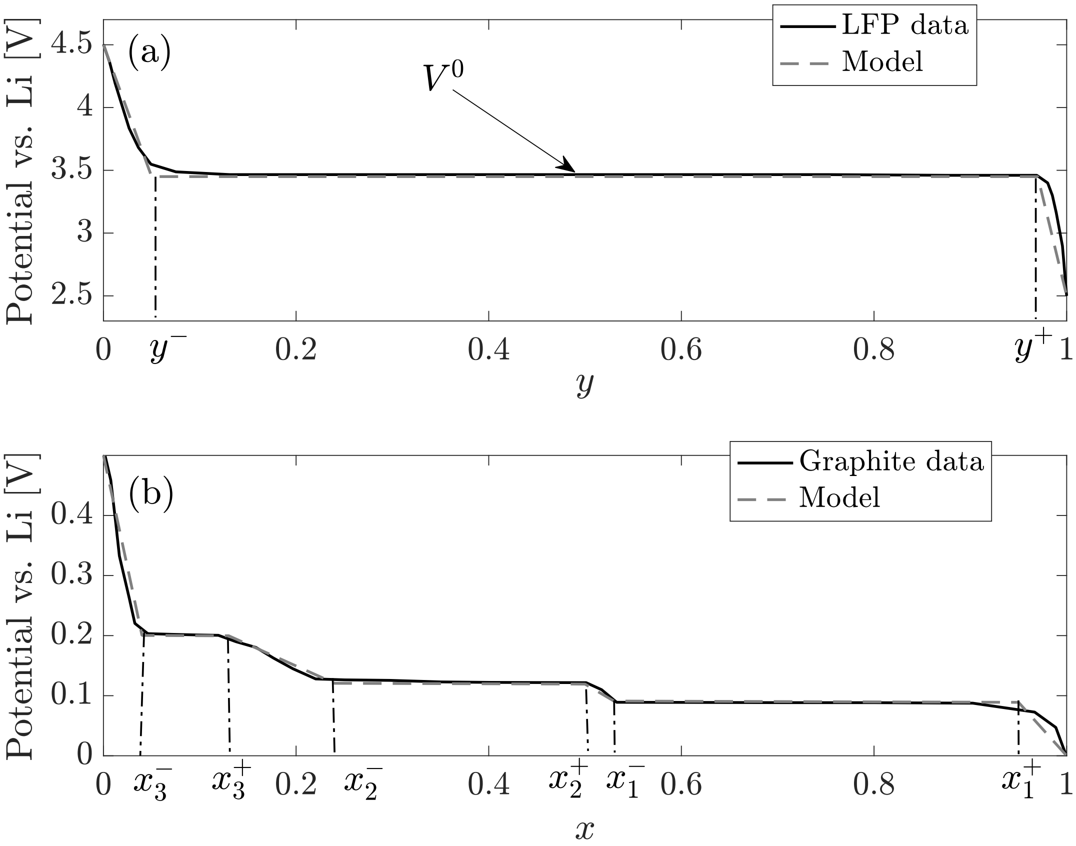

Figure 2.4: (a) The potential (solid-line) of Li_yFePO_4 [3] and its piecewise linear approximation (dashed-line). Furthermore, the potential at $y = 0.5$ is denoted by V^0, and plateau section is bounded by (y^-, y^+). (b) The potential (solid-line) of Li_xC_6 [4] and its piecewise linear approximation (dashed-line).

graphite from [4], the function used for approximating the potential is

$$U_n(x)\ [V] = \begin{cases} -7.46x + 0.5 & x < 0.04 \\ -0.008(x - 0.085) + 0.20 & 0.04 \leq x < 0.13 \\ -0.71x + 0.2931 & 0.13 \leq x < 0.24 \\ -0.005(x - 0.37) + 0.12 & 0.24 \leq x < 0.50 \\ -0.94x + 0.5893 & 0.50 \leq x < 0.53 \\ -0.005(x - 0.74) + 0.09 & 0.53 \leq x < 0.95 \\ -1.77x + 1.77 & 0.95 \leq x. \end{cases} \tag{2.28}$$

The potential response of graphite and the piecewise linear approximation are depicted in Figure 2.4(b).

2.4.2 A Model for Lattice Volume Changes

The intercalation of Li inside the electrode material induces dimension changes and internal stress generation of the electrode. Depending on the electrode material the volume changes could be as significant as 300% from the delithiated state [70], as in silicon. This expansion stems from the changes in lattice parameters and structure of the electrode while the concentration of Li increases in the electrode. Battery expansions can be measured either as thickness changes (free expansion) or as force (constrained expansion). Furthermore, it has been shown that using the expansion measurement helps in a number of scenarios relating to the state of charge and state of health estimation [38, 41].

In order to model the expansion of the cell, it is possible to utilize the changes in the lattice structure. Graphite consists of layers of graphene in a hexagonal structure, and Li intercalates in the spaces between the layers. The distance between the layers is denoted by d, and the distance between the center of adjacent hexagons is denoted by a. In Figure 2.5(a), the crystal structure of

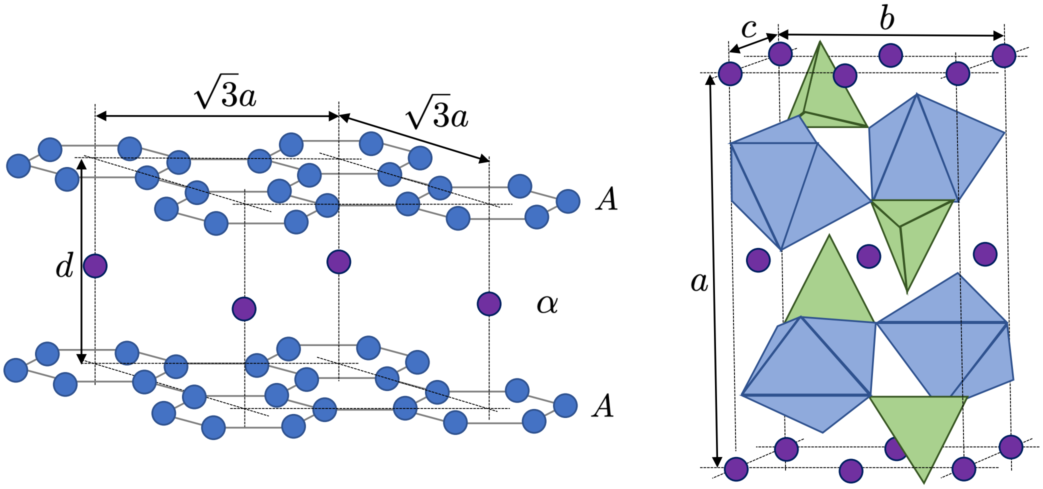

(a) (b)

Figure 2.5: (a) The crystal structure of LiC_6 (stage 1) with $A\alpha A$ stacking. The lithium atoms (represented by purple circles) are at the fictitious layer, α, midway the graphene layers [5]. (b) The crystal structure of $LiFePO_4$. The tetrahedra represent PO_4, and the octahedra represent FeO_6 [6].

lithiated graphite is depicted. The unite lattice volume is a rhombohedron. Table 2.2 shows the edge length of the unit cell and average d-spacing for different phases of graphite. The changes in the volume are calculated using these values and included in Table 2.2. The changes f lattice parameters are anisotropic since the expansion of d is greater than a. However, at the particle level, the layers are orientated randomly. Hence the electrode material can be assumed to be isotropic.

Material	Phase	Structure	x, y	Unit lattice parameters (Å)			Unit lattice volume (Å^3)	$\Delta\mathcal{V}$ (%)
LFP				a	b	c	$\mathcal{V} = abc$	
	$LiFePO_4$	orthorhombic	1.00	10.33	6.01	4.69	291.2	0
	$FePO_4$	orthorhombic	0.00	9.810	5.79	4.78	271.5	-6.76
Graphite				$\sqrt{3}a$		d	$\mathcal{V} = \frac{3\sqrt{3}a^2}{2}d$	
	C	hexagonal	0	4.239		3.35	52.13	0
	Stage 4	hexagonal	0.13	4.254		3.40	53.28	2.20
	Stage 3	hexagonal	0.24	4.255		3.46	54.25	4.06
	Stage 2	hexagonal	0.50	4.262		3.51	55.35	6.18
	Stage 1	hexagonal	1.00	4.289		3.70	58.94	13.06

Table 2.2: Unit cell lattice parameters, unit cell volume, and percentage changes in volume for different phases of graphite and LFP [4, 5, 6]

Thus, it is possible to utilize the changes in lattice parameters to calculate the volume changes in the particle.

The data reported in Table 2.2 are for the pure phases and between these states, the material is a mixture of two phases. Hence, it can be assumed that expansion evolves linearly between two pure phases. This linear behavior is also observed in the experiment (see Figure 2.1(c)). Using this assumption one can derive a piecewise linear function based on the available lattice data points. Hence, the function for volume changes of graphite is

$$\Delta\mathcal{V}_n(x)\ [\%] = \begin{cases} 16.96x & x < 0.13 \\ 16.91(x-0.3)+2.20 & 0.13 \leq x < 0.24 \\ 8.13(x-0.2)+4.06 & 0.24 \leq x < 0.50 \\ 13.76(x-0.5)+6.18 & 0.5 \leq x. \end{cases} \tag{2.29}$$

Similar steps can also be formed for LFP to go from lattice expansion to particle expansion. The unit lattice volume for LFP is a rectangular cuboid. In Figure 2.5(b), the crystal structure of LFP is depicted. The volume change is calculated with respect to the fully lithiated state and is shown in Table 2.2. The piecewise linear function for volume changes of LFP is

$$\Delta\mathcal{V}_p(y)\ [\%] = -6.76(1-y). \tag{2.30}$$

The piecewise linear functions for the volume changes of the graphite and LFP are depicted in Figure 2.6.

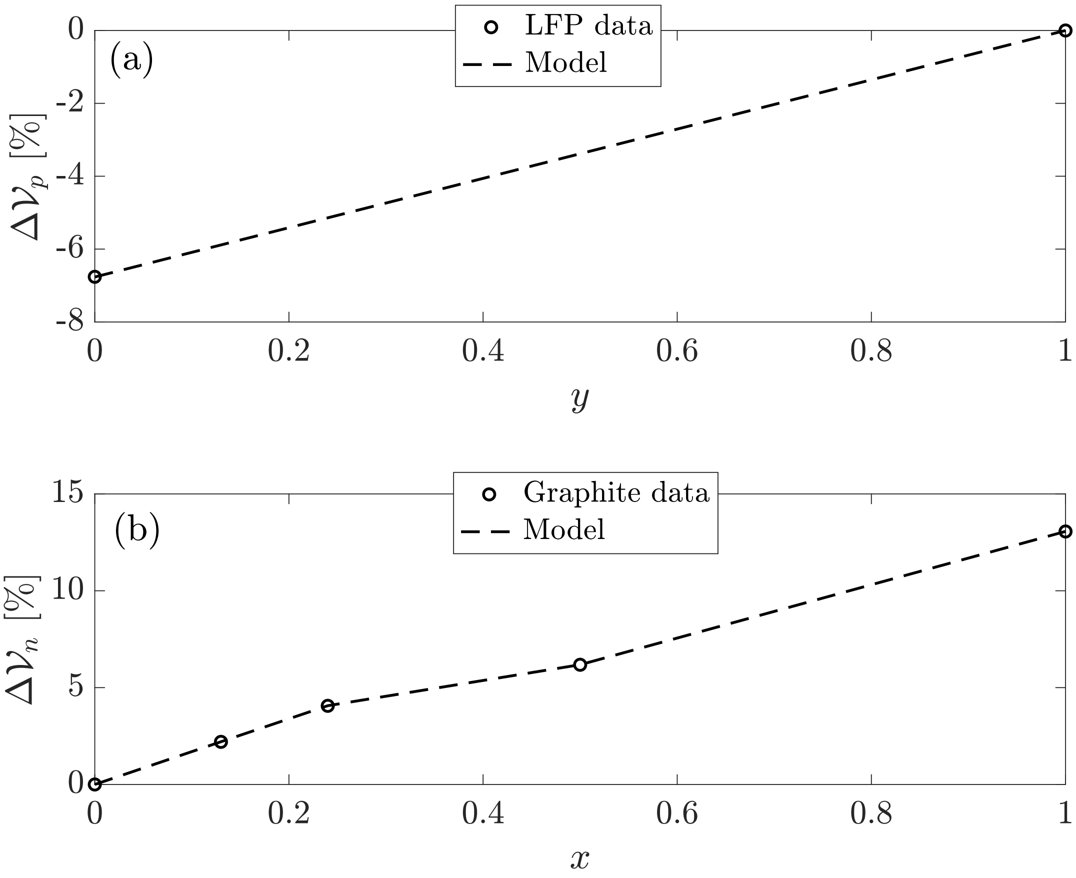

Figure 2.6: The piecewise linear approximation functions for volume changes of particle for (a) LFP and (b) graphite.

2.5 Parameter Identification

In this section, a methodology to estimate the eSOH parameters, based on voltage and expansion measurements, is presented. Furthermore, the identifiability analysis for the parameters are discussed and to carry out the identifiability analysis, a virtual model based on piecewise linear functions is introduced.

2.5.1 Estimation Problem

For the reversible expansion model incorporation in the estimation problem, we need to identify the $(n_c, \kappa_b, \alpha_n, \alpha_p)$ parameters. These parameters depend on the cell structure design as well as the fixture configuration (i.e. applied pressure on the cell), and if we have information on them a rough estimate of the parameters can be made for the purposes of eSOH estimation. However, in this work, we propose a more robust algorithm to calibrate these expansion related parameters. First, we introduce the voltage only eSOH estimation problem, which is given by

$$\begin{aligned} \min_{\theta} \quad & \sum_{i=1}^{N} \left\| OCV(\theta, \Delta Q_i) - \hat{V}_i \right\|^2 \\ \text{subject to} \quad & \\ & U_p(y_{100}) - U_n(x_{100}) = V_{max}, \\ & U_p\left(y_{100} + \frac{C}{C_p}\right) - U_n\left(x_{100} - \frac{C}{C_n}\right) = V_{min}. \end{aligned} \tag{2.31}$$

where $\theta = [y_{100}, C_p, x_{100}, C_n, C, Q_s]$ denotes the eSOH parameters. The OCV is given by Equation (2.10), and the constraints are the operating cell voltage limits defined by Equations (2.2) and (2.3). The measured voltage at ΔQ_i is denoted by $\hat{V}_i$, which is ideally measured at open circuit condition or can be approximated using a low charge rate ($< C/5$). Similarly, a second eSOH estimation problem is introduced, which utilizes the simultaneous voltage and expansion measurements, and is defined by

$$\begin{aligned} \min_{\theta} \quad & \sum_{i=1}^{N} \left\| Y(\theta, \Delta Q_i) - \hat{Y}_i \right\|^2 \\ \text{subject to} \quad & \\ & U_p(y_{100}) - U_n(x_{100}) = V_{max} \\ & U_p\left(y_{100} + \frac{C}{C_p}\right) - U_n\left(x_{100} - \frac{C}{C_n}\right) = V_{min} \end{aligned} \tag{2.32}$$

where $Y(\theta, \Delta Q_i) = [OCV(\theta, \Delta Q_i), \Delta t_c(\theta, \Delta Q_i)]^T$, vector of measurements is $\hat{Y}_i = [\hat{V}_i, \hat{\delta}_i]^T$, and Δt_c is given by Equation (2.19). The last problem is for estimating the expansion related parameters given the eSOH parameters, θ, and is defined by

$$\min_{\xi} \quad \sum_{i=1}^{N} \left\| \Delta t_c(\xi, \Delta Q_i) - \hat{\hat{\delta}}_i \right\|^2 \tag{2.33}$$

where $\xi = [k_b, \alpha_p, \alpha_n]$. Note that, in the aforementioned parameter set $k_b = n_c \kappa_b$. Since in Equation (2.19) the (n_c, κ_b) parameters appear only in a multiplicative form, these two parameters are not uniquely identifiable.

2.5.2 Estimation Procedure

The models presented so far can be used either during a slow charge or slow discharge. However, because of the presence of hysteresis in voltage and expansion, different potential and expansion functions are needed for charge and discharge. Since performing controlled charge is a more viable choice in applications, here, we also carry out the estimation during charging. The functional forms for potential and expansion henceforth correspond to the electrode response during cell charging. The estimation procedure for calibrating expansion parameters and estimating eSOH parameters using expansion and voltage is as follows:

1. At the cell fresh state measure the voltage and expansion during a slow charge (C/20).
2. Estimate the eSOH parameter, θ_f, using Equation (2.31) (voltage only) and the full range of data.
3. Estimate the expansion parameters, ξ, using Equation (2.33) with the identified θ_f and the full range of data.
4. At the cell aged state measure the voltage and expansion during a slow charge (C/20).
5. Estimate the eSOH parameter, θ_a, using Equation (2.32) given the identified ξ.

Note that when using simultaneous expansion and voltage measurements, a full range of data is not necessarily needed. In section 2.6, the estimation accuracy and error is compared for a case of full and limited data window.

2.5.3 Identifiability Analysis

The identifiability analysis can be explored by means of Fisher Information Matrix (FIM), and the Cramer-Rao bound (CRB) matrix, which gives the lower bound on the error covariance matrix of an unbiased estimate of a nonrandom parameter vector. The problem (P) has an equality constraint related to the maximum voltage of the cell. Therefore, here a methodology based on [71] is introduced, which incorporates the equality constraints in the calculation of the CRB.

It is assumed that the measurements can be modeled as

$$\hat{Y} = Y(\theta) + \epsilon, \tag{2.34}$$

where ϵ is an additive measurement error, which can include measurement noise and model mismatch. In the context of a least squares estimation problem, assuming a zero mean Gaussian vector with the covariance matrix, E, for ϵ, the FIM can be written as [72]

$$\mathcal{I}_f = S^T E^{-1} S, \tag{2.35}$$

where $S = \partial Y / \partial \theta$ is the local sensitivity matrix calculated at true $\theta = \theta^*$. If FIM is nonsingular, the $\mathcal{I}_f^{-1}$ is the *unconstrained* CRB for the error covariance matrix of θ.

Since the problem statement has constraints, following procedure is used to determine the *constrained* CRB [71]. Let the constraints be defined as follows

$$f(\theta^*) = 0, \tag{2.36}$$

where it is assumed that f is locally differentiable. Define $\mathcal{O}$ is an orthogonal matrix ($\mathcal{O}^T \mathcal{O} = I$), which forms an orthonormal basis for the nullspace of the gradient of the constraints. That is

$$\left.\frac{\partial f(\theta)}{\partial \theta}\right|_{\theta^*} \mathcal{O} = 0. \tag{2.37}$$

If $\mathcal{O}^T \mathcal{I}_f \mathcal{O}$ is nonsingular, then the the *constrained* problem is identifiable, moreover, the error covariance, Σ matrix i.e. *constrained* CRB is

$$\Sigma \geq \mathcal{O}(\mathcal{O}^T \mathcal{I}_f \mathcal{O})^{-1} \mathcal{O}^T. \tag{2.38}$$

Furthermore,

$$\sigma_\theta = \sqrt{diag[\Sigma]}, \tag{2.39}$$

where σ_θ is the standard parameter error. Furthermore, the standard error is normalized with respect to the parameter true value to give a percentage error as following:

$$Error\ (\%) = \frac{\sigma_{\theta_i}}{\theta_i} \times 100. \tag{2.40}$$

2.5.4 Slopes of Electrode Potential and Expansion

Under the assumption that the noise is zero-mean Gaussian and independent, E can be written as

$$E = \begin{bmatrix} E_V & 0 \\ 0 & E_t \end{bmatrix}, \tag{2.41}$$

where $E_V = diag[\sigma_V^2]$ and $E_t = diag[\sigma_t^2]$. Furthermore, the sensitivity matrix, S, can be written as

$$S(\theta^*) = \begin{bmatrix} S_V(\theta^*) \\ S_t(\theta^*) \end{bmatrix}, \tag{2.42}$$

where $S_V = \left.\frac{\partial OCV}{\partial \theta}\right|_{\theta^*}$, $S_t = \left.\frac{\partial \Delta t_c}{\partial \theta}\right|_{\theta^*}$.

For the optimization problem (P) in this study, the sensitivity of OCV (Equation (2.10)) with respect to x_{100} corresponds to the first column of $S_V(\theta^*)$. At measurement, Q_i, corresponding to stoichiometric state, x_i (Equation (2.8)), this entry is as follows

$$\frac{\partial OCV_i}{\partial x_{100}} = \frac{\partial OCV_i}{\partial x_i} \cdot \frac{\partial x_i}{\partial x_{100}} = -\frac{\partial U_n}{\partial x_i}, \tag{2.43}$$

which is the slope of the negative electrode potential. The second column of $S_V(\theta^*)$ is computed as $\frac{\partial OCV_i}{\partial y_{100}} = \frac{\partial U_p}{\partial y_i}$ which is the slope of the positive electrode potential. The third and fourth column are calculated similarly. Then, the sensitivity matrix assuming N measurements with $Q_1, ..., Q_N$ charge levels can be written as

$$S_V(\theta^*) = \begin{bmatrix} -\frac{\partial U_n}{\partial x_1} & \frac{\partial U_p}{\partial y_1} & -\frac{\partial U_n}{\partial x_1}\frac{Q_1}{C_n^2} & -\frac{\partial U_p}{\partial y_1}\frac{Q_1}{C_p^2} \\ \vdots & \vdots & \vdots & \vdots \\ -\frac{\partial U_n}{\partial x_N} & \frac{\partial U_p}{\partial y_N} & -\frac{\partial U_n}{\partial x_N}\frac{Q_N}{C_n^2} & -\frac{\partial U_p}{\partial y_N}\frac{Q_N}{C_p^2} \end{bmatrix}. \tag{2.44}$$

For the case of voltage only measurements, if all the measurements are from a single slope the first and second columns in the sensitivity matrix in Equation (2.44) become linearly dependent due to the same values of entries for all measurements. Thus, the sensitivity matrix is rank deficient and the problem is unidentifiable. Hence, at minimum the measurements have to be taken from regions with different slopes.

The sensitivity of expansion (Equation (2.19)) to x_{100} is as follows

$$\frac{\partial \Delta t_{ci}}{\partial x_{100}} = w_n \left(\frac{\partial \Delta \mathcal{V}_n}{\partial x_i} - \gamma^{100} \right) \tag{2.45}$$

where $\gamma^{100} = \left.\frac{\partial \Delta \mathcal{V}_n}{\partial x_{100}}\right|_{x_{100}^*}$, and $w_n = n_c \kappa_b \frac{\alpha_n C_n}{C_n^f}$ are substituted for brevity. The second column of $S_t(\theta^*)$ is computed as $\frac{\partial \Delta t_{ci}}{\partial y_{100}} = w_p \left(\frac{\partial \Delta \mathcal{V}_p}{\partial y_i} - \zeta^{100} \right)$, where $\zeta^{100} = \left.\frac{\partial \Delta \mathcal{V}_p}{\partial y_{100}}\right|_{y_{100}^*}$, and $w_p = n_c \kappa_b \frac{\alpha_p C_p}{C_p^f}$.

The third and fourth column are calculated similarly. Then, the sensitivity matrix can be written as

$$S_t(\theta^*) = \begin{bmatrix} w_n\left(\frac{\partial \Delta \mathcal{V}_n}{\partial x_1} - \gamma^{100}\right) & w_p\left(\frac{\partial \Delta \mathcal{V}_p}{\partial y_1} - \zeta^{100}\right) & -w_n \frac{\partial \Delta \mathcal{V}_n}{\partial x_1}\frac{Q_1}{C_n^2} & w_p \frac{\partial \Delta \mathcal{V}_p}{\partial y_1}\frac{Q_1}{C_p^2} \\ \vdots & \vdots & \vdots & \vdots \\ w_n\left(\frac{\partial \Delta \mathcal{V}_n}{\partial x_N} - \gamma^{100}\right) & w_p\left(\frac{\partial \Delta \mathcal{V}_p}{\partial y_N} - \zeta^{100}\right) & -w_n \frac{\partial \Delta \mathcal{V}_n}{\partial x_N}\frac{Q_N}{C_n^2} & w_p \frac{\partial \Delta \mathcal{V}_p}{\partial y_N}\frac{Q_N}{C_p^2} \end{bmatrix}. \tag{2.46}$$

Therefore the identifiability of the parameters in the estimation problem depends on the number of rate changes in electrode potential/expansion included in the measurement.

2.5.5 Graphite/LFP Cell Model

The eSOH parameters are fitted to the *full range* of voltage and expansion data. The fitting results are reported in Table 2.3. Furthermore, the data and the fitting result are shown in Figure 2.7, which also shows the relationship between electrode potential/expansion and the cell voltage/expansion. In this figure, the expansion is normalized with respect to maximum expansion to show the characteristic behavior of a representative cell in the battery. Based on the fitting result, a virtual model is constructed to study the identifiability of the parameter under a variety of data availability scenarios, such as a limited number of measurements, and identifiability under voltage and voltage plus expansion measurements. The virtual model uses the piecewise linear functions introduced in Section 2.4.

2.6 Results and Discussion

In this section, the result of identifiability analysis for eSOH parameters is presented and discussed. The analysis is done using the data generated by the virtual model. The limited data scenarios include a case of voltage measurements alone and a case of voltage plus expansion measurements, both with data available only in certain SOC windows. The data window is defined as follows: it is assumed that there is one measurement opportunity at every 1% change in SOC, starting from the

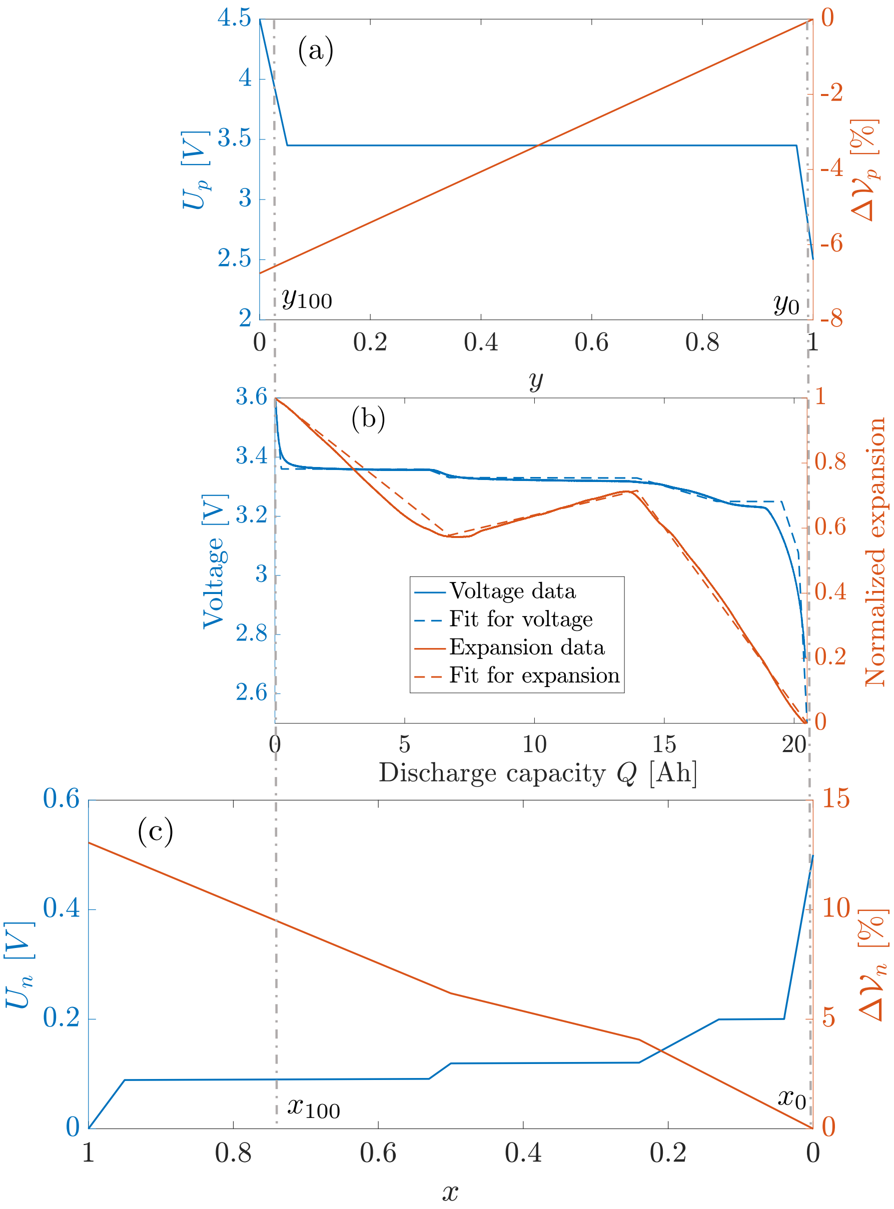

Figure 2.7: (a) The model of potential and expansion of LFP, and (c) graphite. (b) The fitting results of OCV and expansion along with the data.

fully charged state. With each addition of the measurements, the standard error of the parameters is calculated. The size of the data window is denoted by the depth of discharge (DOD). Given that the method so far relies on the open circuit state, for transportation applications, the data can accumulate every time there is an open circuit opportunity, for instance, at every key-on with ample rest time before it. Also, at very low c-rate such as level 1 charging.

Pouch cell			
Nominal capacity		20.5 Ah	
Operating voltage		2.5-3.6 V	
		Graphite	LFP
Electrode thickness t_i^0 (μm)		43 [73]	70 [74]
Active material volume ration ξ_i		0.63 [73]	0.42 [74]
Electrode potential U_i (V)		Equation (2.28)	Equation (2.27)
Particle volume expansion $\Delta\mathcal{V}_i$ $(\%)$		Equation (2.29)	Equation (2.30)
Fitted parameters			
x_{100}	y_{100}	C_n (Ah)	C_p (Ah)
0.741	0.038	27.85	21.65

Table 2.3: The parameters used in the virtual model for identifiability demonstration.

The results of the standard parameter error versus the DOD (data window) are shown in Figure 2.8. This result is obtained using $\sigma_V = 10\ mV$ and $\sigma_t = 5\ \mu m$ measurement error. The goal is to show the relative observability of the two scenarios of voltage alone and voltage plus expansion measurements. For this work, the data window starts from the fully charged state.

2.6.1 Connection to Phase Transitions

The results indicate that as the measurements move to a higher DOD, the estimation error decreases for all the parameters. This reduction happens in stages, which corresponds to the phase transitions in the material. For example, for the parameter x_{100}, the estimation error decreases as the graphite is transitioning from stage 1 to stage 4 (Tables 2.1 and 2.2). Each error reduction corresponds to the ending of a plateau (phase coexistence), which is indicated by bounding stoichiometric states (x_1^-, x_2^-, x_3^-) in the figure. For example, the first error reduction ($x \approx 0.5$) corresponds to slope changes in both voltage and expansion. Furthermore, for the parameter C_p, in case of voltage alone measurement, the estimation error remains at a constant value until almost 98% DOD, which corresponds to the stoichiometric state (y^+) bounding the plateau in LFP.

As shown in Equations (2.44) and (2.46), the identifiability of the parameters depends on rate changes of electrode voltage/expansion, which is related to phase transition in the material. Therefore, it is deduced that having data at phase transitions provides better identifiability of the individual electrode parameters. The error goes down as the electrodes go through the phase transitions. It is noted that the results agree with the long-established method, Differential Voltage Analysis (DVA), which depends on terminal voltage data across phase transitions to compute the shifts of the peak locations in the dV/dQ curve [75].

Furthermore, the results indicate that the parameters are unobservable at low DOD regions. However, in practice, compared to the simple model used in this study, there are more nonlinearities near the low DODs which results in better-conditioned sensitivity matrices. Hence, the observability of the parameters should enhance in practice.

2.6.2 Observability of the Different Parameters

Recall that the problem (P) includes an equality constraint (maximum voltage limit) which intrinsically couples the error estimates of parameters x_{100} and y_{100}. Using the Taylor series expansion of the voltage constraint about the true solution the following equation is obtained

$$\sigma_y \left.\frac{\partial U_p}{\partial y}\right|_{y_{100}} = \sigma_x \left.\frac{\partial U_n}{\partial x}\right|_{x_{100}} . \tag{2.47}$$

Comparing the voltage only measurements results of x_{100} with y_{100}, it is evident that the error for x_{100} is larger than y_{100}. The reason for this disparity in estimating x_{100} and y_{100} can be explained using Equation (2.47). It is apparent that $\frac{\partial U_n}{\partial x}$ at flat region of U_n is smaller than $\frac{\partial U_p}{\partial y}$ which is at the higher derivative region of U_p. Since the estimation error of x_{100} and y_{100} are proportional through Equation (2.47), it stands to reason that x_{100} has larger estimation error than y_{100}.

The parameter error of C_n and C_p can also be explained by the same analysis of the sensitivity matrix. The parameter error of C_n and C_p are related to the third and fourth column of the sensitivity matrix in Equation (2.44). For C_p to have a lower parameter error the window should include at least one of the asymptotes of U_p function i.e. at least two different slopes. Thus, the reason parameter error of C_p is small near the edges of fully discharged states. The same analysis is also

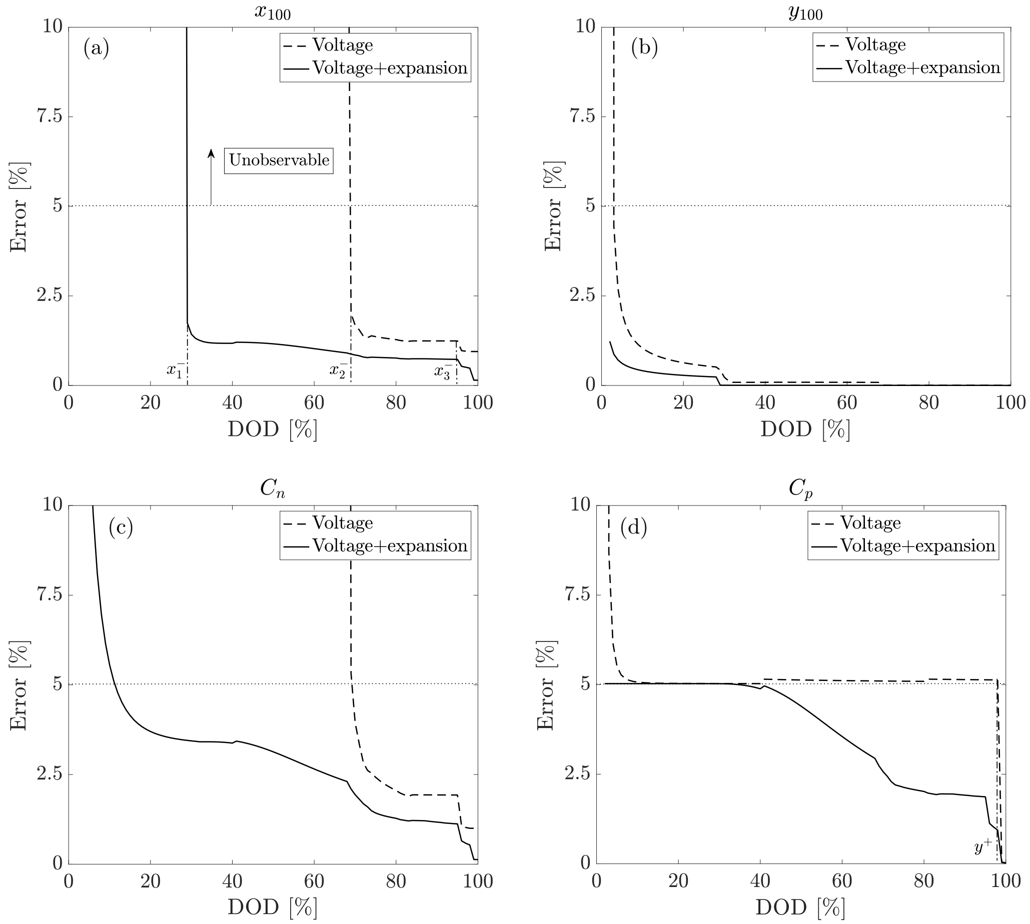

Figure 2.8: Parameter error of (a) x_{100} (b) y_{100} (c) C_n (d) C_p calculated for different data windows starting from fully charge and ending at DOD, plotted for the case of voltage only and the case of voltage plus expansion measurements.

true for C_n. As the U_n function is almost flat until high DODs.

2.6.3 Observability with the Addition of Expansion

From the results in Figure 2.8, it can be seen that with the addition of expansion measurement the estimation error decreases for all the parameters. This reduction is more significant for the negative electrode parameters (x_{100}, C_n) than the positive electrode parameters (y_{100}, C_p). The reasons are that in the case of graphite/LFP cell; first, the slopes of $\Delta\mathcal{V}_{p/n}$ functions are a magnitude larger than the slopes of $U_{p/n}$ functions. Second, graphite has several rate changes while expanding, whereas LFP expands at a constant rate. As a result, the expansion is more sensitive to a change in parameters compare to voltage, especially in the middle SOC region (see Figure 2.2). Hence, in this chemistry, the expansion measurement is more beneficial for the negative electrode than the positive electrode.

Finally, a threshold of 5% is selected as an acceptable amount of estimation error for the parameters. Using this criterion, it is evident that by having the expansion measurements the estimation is feasible at about 30% DOD. Hence, there is no need to have data near fully discharged states, which is important since battery packs are rarely discharged fully in automotive applications. Therefore, it is concluded that in order to have better confidence levels in the presence of noise and limited data, having the expansion measurement is necessary for estimating eSOH parameters.

2.7 Summary

The fundamental benefit of using cell expansion measurement for estimating electrode specific SOH parameters, which correspond to the individual electrode capacity and the utilization window, was presented. First of all, to provide a measure of the identifiability of individual electrode parameters concerning the measurement noise, the standard error of the parameters was calculated by the constrained Cramer-Rao Bound. Furthermore, to make the analysis simpler and intuitive, the electrodes potential/expansion were approximated by the piecewise linear functions under the consideration of the phase transitions of materials. The results show that for material like LFP with flat voltage response at middle SOC regions the estimation of the individual electrode parameters is feasible by having the expansion measurements. It is worth mentioning that the effects of the temperature, hysteresis, and the dynamics of the battery under nonzero current profile were not included in the analysis of this chapter.

CHAPTER 3

Experimental Study on Evolution of Cell Expansion Under a Wide Range of Degradation Factors

3.1 Introduction

The focus of this chapter is to systematically verify the capability of aging diagnostics using cell expansion under variety of aging conditions. The data collection campaign covers various degradation stress factors in order to inform, parameterize, and validate the diagnostic model. This data collection campaign, for the first time documents the evolution of the electrical and mechanical characteristics of multiple cells under variety of stress factors. The testing matrix covers a wide range of conditions from charge/discharge C-rates, temperatures, depth of discharges, and applied pressures. It is important to note that we collect data using specially designed fixtures that enables the simultaneous measurement of mechanical and electrical response under constant pressure. This expands significantly the prior experimental campaigns, which often performed in unconstrained [76, 77] or completely constrained conditions [42, 78], where the cells are clamped to a fixed distance and the irreversible expansion leads to increased compression over life.

Additionally, we directly compare the differential voltage (DV), incremental capacity (IC), and various differential expansion (DE) features and develop capacity estimation methods based on voltage and expansion that are accurate and robust with respect to the aging conditions. Specifically, it is shown that nearly linear regression is observable between capacity and the features. Moreover, for the features to be beneficial for real-world applications, they need to:

1. be detectable at various practical C-rates
2. occur within an operational SOC range (preferably close to 50% SOC)
3. be unaffected by the initial SOC

The Chapter is organized as follows: Section 3.2 describes the experimental methodology and presents the range of aging conditions from charge/discharge C-rates, temperatures, depth of discharges, and pressures. Section 3.3 presents the experimental results, capacity fade, reversible and irreversible expansion evolution. Moreover, the correlation of the voltage and expansion signals with the capacity fade are introduced. Additionally, the results of resistance growth and its correlation with capacity fade are presented. Using the experimental data number of features in expansion and voltage are identified, and linear regression models based on a different combination of features are developed. The accuracy and robustness of the different models are compared, and a model based on the zero crossing of the differential expansion feature shown to be superior for the capacity estimation. Finally, Section 3.4 summarizes the contributions.

3.2 Experimental Procedures

A number of identical pouch cells were manufactured in one batch using the fabrication facility at the University of Michigan Battery Lab (UMBL) to study the degradation under various conditions. The production of the cells in one batch minimizes the cell-to-cell variation in performance caused by the manufacturing process [79]. These cells were graphite/NMC chemistry and designed as energy cells with the detailed specifications shown in Table 3.1. The cells were assembled inside the fixture shown in Figure 3.1 (a). The fixture was designed such that the top and bottom plates are fixed in place while the middle plate is free moving. Compression springs were used to apply a prescribed pressure on the cell. Spring modulus was selected to be much lower than the battery, which ensures almost constant pressure on the cell as it cycles and expands. Initial target pressures of 34.5 kPa (5 psi) were achieved by adjusting the spring compression to a fixed displacement

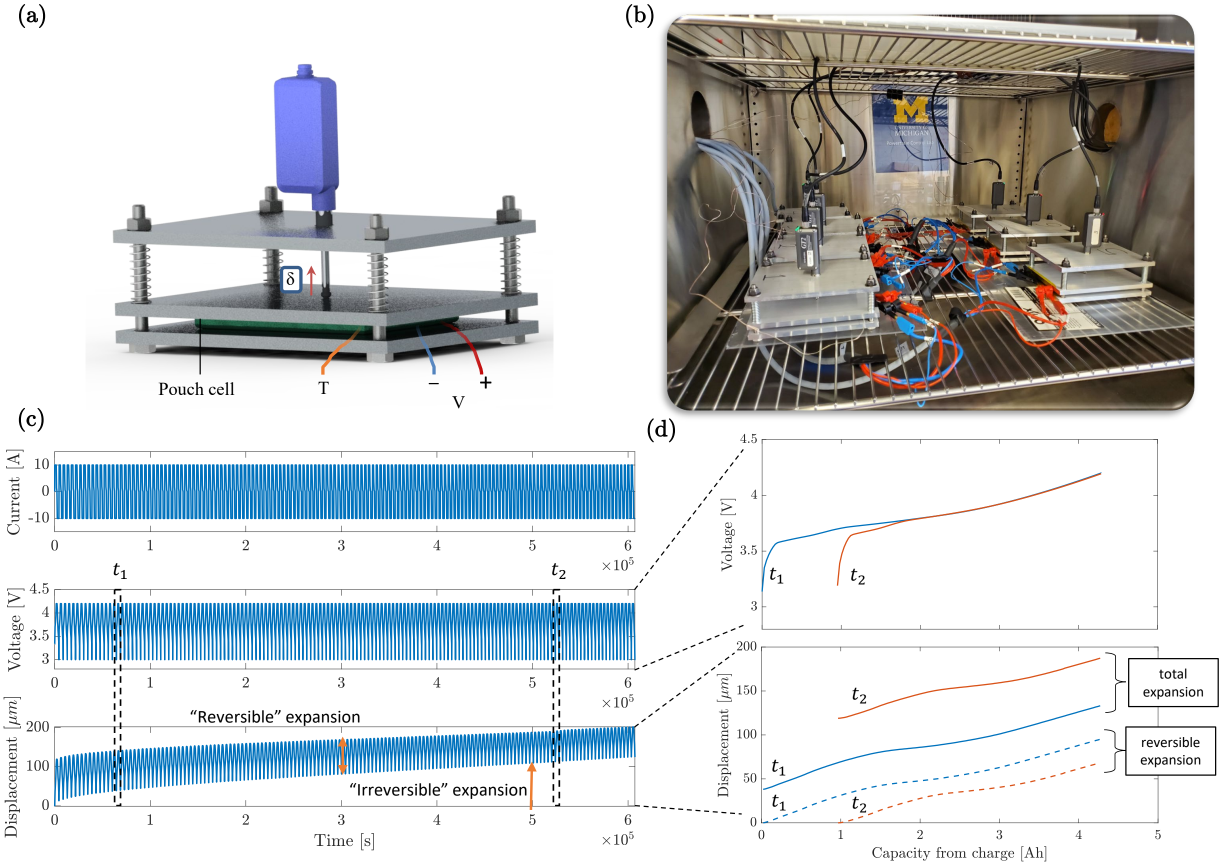

Figure 3.1: a) The fixture schematics, b) the testing configuration in the climate chamber, c) the current, voltage, and expansion response for condition 2C $@45°C$ during cycling with the reversible and irreversible expansion. d) The voltage and expansion response from two snapshots in time (t_1,t_2) plotted versus charge capacity. Note that the thickness change during one charge cycle is shown as the total expansion and the relative change as the reversible expansion.

using the threaded rods. Furthermore, polymer poron sheets (Rogers, USA) were used on both sides of the pouch cell to achieve a more uniform pressure on the cell and avoid high-pressure spots. The expansion was measured using a displacement sensor (Keyence, Japan) mounted on the center of the top plate. The dynamic testing was carried using a battery cycler (Biologic, France). The fixtures were installed inside a climate chamber (Cincinnati Ind., USA) in order to control the temperature during cycling and the characterization tests as shown in Figure 3.1 (b). The temperature was measured using a K-type thermocouple (Omega, USA) place on the battery's surface.

The aging experiments were designed to cover an array of stress factors such as C-rates during

Pouch cell	
Nominal capacity	5.0 Ah
Operating voltage	3.0-4.2 V
Thickness	4.0 mm
Length	132 mm
Width	90 mm
Positive electrode	
Material	NMC111:CB:PVDF (94:3:3)
Number of double sided electrode sheets	14
Electrode active material loading	18.5 (single side) mg/cm^2
Electrode thickness	67 μm
Negative electrode	
Material	Graphite:PVDF (95:5)
Number of double sided electrode sheets	15
Electrode active material loading	8.55 (single side) mg/cm^2
Electrode thickness	62 μm
Separator	
Material	Polyethylene (PE)
Electrolyte	
Material	1 M $LiPF_6$
Organic solvent in electrolyte	2$\%$ EC:EMC (3:7)

Table 3.1: Pouch cell specifications.

charge and discharge, depth of discharges (DOD), temperatures, and applied pressures. Based on these stress factors, a number of testing conditions were selected. The summary of all the testing conditions is shown in Table 3.2. Each of the test conditions is done at three different temperatures of hot ($45°C$), cold ($-5°C$), and room ($25°C$), which are indicated by condition group A to G. The condition group G utilizes a realistic daily drive cycle with fast charging for an electric vehicle. The details of the drive cycle are presented in Figure 3.2. The drive cycle is composed of several standard drive cycles based on a home-to-work/work-to-home (back and forth) commute scenario, assuming a home at city of Ann Arbor, MI and the work is at Dearborn, MI for a total of 71 miles of range. The current profile was obtained by assuming driving a 33 kWh battery pack. The EPA standard drive cycles used for the synthetic drive cycle are UDDS (Urban Dynamometer Driving Schedule), HWFET (Highway Fuel Economy Test), and US06 (one of the Supplemental Federal Test Procedures). The UDDS represents city driving conditions, HWFET is used to determined the highway fuel economy rating, and US06 combines the current city and highway cycles to reflect real-world fuel economy more accurately that has a high speed, quick acceleration, and four stops. For instance, US06 has more frequent large spikes in current profile than the other two, and HWFET has a higher average current than UDDS, reflecting the highway driving condition. The hot temperature/high C-rate condition was selected as an accelerated aging test to study the effects of pressure on the cycle-life (shown as condition group H). In the following, the C-rate noted for all the test procedures is defined with respect to the *nominal* cell capacity (i.e., 5 Ah).

Cycling procedure Before the start of the cycling tests, the chamber temperature was set to the target temperature of the cycling test and the cells were held at rest for 3 hours to ensure thermal equilibrium. The cycling consists of a constant current (CC) charge until reaching 4.2 V, followed by a constant voltage (CV) phase at 4.2 V until ($I < C/50$). Then a CC discharge until reaching 3.0 V for the full range conditions. For partial DOD the discharge time is with respect to the nominal capacity (i.e. to obtain 50% DOD, 2.5 Ah are discharged from a completely charged state). During all the tests, in addition to the traditional signals of voltage, current, and temperature, the thickness changes of the cell is also recorded. As an example, Figure 3.1(c) shows the voltage and expansion response of the condition 2C $@45°C$ during cycling. Figure 3.1(d) shows two separate voltage and expansion responses versus capacity at two different snapshots during cycling. The reversible and total part of the expansion response are denoted in the figure. All the cells were cycled to at least 80% capacity retention and characterization tests performed periodically.

Reference Performance Test (RPT) Before the start of the aging tests initial RPTs were done for all the cells. The subsequent RPTs were performed after a certain number of cycles corresponding to an expected 5% capacity loss for cycling aging tests. For RPT the cells were brought

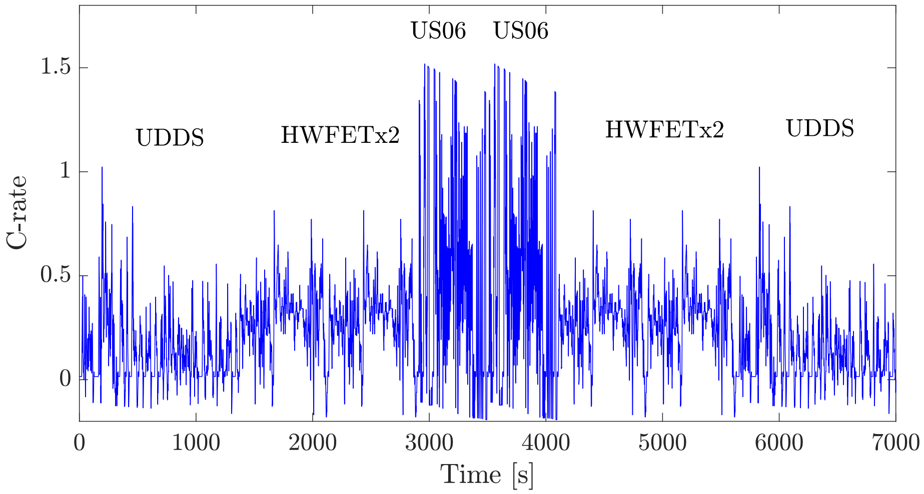

Figure 3.2: The synthetic drive cycle used in the cyclic aging experiment. The positive C-rate values corresponds to discharging.

Cyclic aging conditions				
Condition group	Cell number - Temperature (R/C/H)[a]	DOD	Charge[b]	Discharge
A - (baseline)	01 (R) | 02 (C) | 03 (H)	0-100%	C/5	C/5
B	04 (R) | 05 (C) | 06 (H)	0-100%	1.5C	1.5C
C - (fast charge)	07 (R) | 08 (C) | 09 (H)	0-100%	2C	2C
D	10 (R) | 11 (C) | 12 (H)	0-100%	C/5	1.5C
E	13 (R) | 14 (C) | 15 (H)	0-50%	C/5	C/5
F	16 (R) | 17 (C) | 18 (H)	0-50%	C/5	1.5C
G - (drive cycle)	19 (R) | 20 (C) | 21 (H)	0-50%	1.5C	Drive cycle[c]
H - (pressure effects)				
1 PSI	22 (H)	0-100%	2C	2C
5 PSI	23 (H) | 24 (H)	0-100%	2C	2C
10 PSI	25 (H) | 26 (H)	0-100%	2C	2C
15 PSI	27 (H) | 28 (H)	0-100%	2C	2C
20 PSI	29 (H) | 30 (H)	0-100%	2C	2C
25 PSI	31 (H)	0-100%	2C	2C

Table 3.2: The aging test conditions matrix. [a] The R, C, and H corresponds to room ($25°C$), cold ($-5°C$), and hot ($45°C$) temperature. [b] Constant current until 4.2 V and then constant voltage until ($I < C/50$). [c] For the details on the drive cycle refer to the Figure 3.2.

back to the room temperature ($25°C$) and held at rest for 3 hours to ensure thermal equilibrium. The RPTs are as the following:

1. A C/20 charge-discharge cycle which consists of an initial C/5 discharge until reaching 3.0 V, followed by a constant voltage (CV) phase at 3.0 V until ($|I| < C/50$) and 1 hour rest to ensure the cell is fully discharged. Then a C/20 charge until reaching 4.2 V, followed by a constant voltage (CV) phase at 4.2 V until ($I < C/50$) and 1 hour rest. Then a C/20 discharge until reaching 3.0 V. The C/20 data is used to approximate the open circuit response of the battery.

2. Hybrid pulse power characterization (HPPC) and electrochemical impedance spectroscopy (EIS) measurements at 10% SOC intervals. First the cells are charged using C/2 CC until 4.2 V, followed by a CV at 4.2 V until ($I < C/50$) and 1/2 hour rest. Then a C/2 CC discharge for an equivalent of 10% SOC discharge, where the discharge time was adjusted based on the prior capacity measurement (C/20) test. Followed by a 1/2 hour rest. Then the HPPC profile was done which consists of a 1C CC discharge for 10 s, a 10 min rest, a 1C CC discharge for 10 s. Followed by a 10 min rest. Then the EIS measurement was done over frequency range of 10 mHz - 10 kHz. The above steps were repeated until the end of discharge 3.0 V was reached.

3. The C-rate dependency test consists of charging the cell at different rates for characterizing the rate capabilities of the cell. Before each charge, the cell was fully discharged to 3.0 V by a C/3 discharge current until reaching 3.0 V, followed by a CV phase at 3.0 V until ($|I| < C/50$). Then the cell was charged using CC (C/10, C/5, C/2, and 1C) until 4.2 V.

Half-cell measurements The data for the positive and negative half cells were identified by assembling coin cells from fresh cells electrode materials and the details can be found in Section 4.3.

Initial SOC sensitivity test A C/3 discharge to 5% SOC, followed by a 1 hour rest. Then a charge with C/10 CC until 4.2 V, followed by a CV phase at 4.2 V until ($I < C/50$) and 1 hour rest. The previous steps are repeated for a discharge to 20% and 40% SOC. The test is done again for the C/5, C/2, and 1C for the charge current.

3.2.1 Data availability

The dataset presented in this chapter is made publicly available at [80].

3.3 Results and Discussion

3.3.1 Capacity retention

The capacity evolution of all the aging conditions are shown in Figure 3.3. The aging conditions are also denoted in Figure 3.3. The conditions consists of symmetrical and unsymmetrical cycling with C-rates from C/5 to 2C, room $@25°C$, cold $@-5°C$, hot $@45°C$ temperatures, and a full and 50% depth of discharge. The capacity fade as in *thermodynamic* capacity (low C-rate) and *apparent* capacity are shown in Figure 3.3 (a) and (b), respectively. In this chapter, the thermodynamic capacity is the defined using the C/20 capacity, which is shown in Figure 3.3 (a). The thermodynamic capacity fade is primarily caused by loss of lithium inventory (LLI), and loss of active material in the positive ($\mathrm{LAM_{pe}}$) and negative ($\mathrm{LAM_{ne}}$) electrodes [81] aging modes. The increase of the internal resistance also plays a role in reducing the capacity, however, the diagnostic test utilizes a very low charging rate of C/20, which minimizes the impact of resistance on the measured capacity. As a result, the C/20 capacity only captures the thermodynamic capacity fade due to the aging modes and does not capture losses due to the resistance growth.

On the other hand, Figure 3.3 (b) shows the apparent discharge capacity, which is measured at the C-rate and temperature that the cells were cycling. Therefore, depending on the C-rate, the resistance growth can also reduce the measured apparent capacity when the minimum voltage is reached sooner due to a larger ohmic voltage drop. The apparent capacity can be a more relevant measure of capacity in the field applications, nevertheless, it can be easily inferred after estimating the thermodynamic capacity by measuring the resistance. The measurement of resistance is relatively easy and fast since, for example, it can be done with simple pulse charge techniques. In terms of capacity estimation, in this chapter, the objective is the estimation of the thermody-

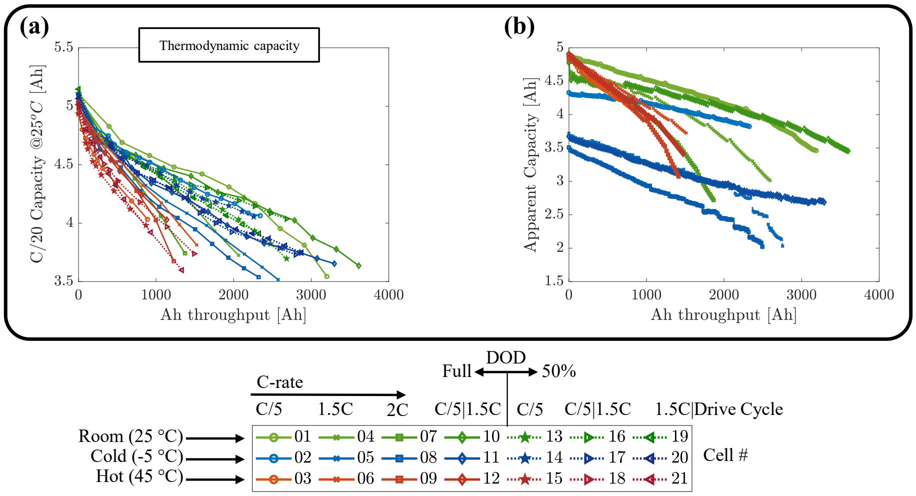

Figure 3.3: a) The thermodynamic capacity measured during the periodic C/20 tests at $25°C$, which is computed by averaging the charge and discharge capacities. The C/20 capacity is plotted for all the aging conditions versus Ah throughput. b) The apparent discharge capacity measured during cycling. The apparent capacity is only available for the cell with a full DOD.

namic capacity. Measurement of the thermodynamic capacity requires prolonged experiments that often can take days to finish. Moreover, the periodic thermodynamic capacity RPT disrupts the cycling aging and can have unintended consequences on the aging process, such as capacity recovery [82, 83], that complicates the translation of lab data to the real-world aging scenarios. Therefore, methods that can estimate the thermodynamic capacity during cycling and accelerated conditions such as high C-rates are greatly advantageous.

3.3.2 Reversible and irreversible expansion

In Figure 3.4 (a) and (b) the capacity retention is plotted as a function of the irreversible and reversible expansion, respectively. The capacity retention in this figure is measured during the C/20 RPT and represents the thermodynamic capacity fade. The reversible expansion is calculated during the C/20 test by subtracting the expansion at the fully charged state from the expansion at the fully discharged state. It should be pointed out that the fixture is designed to maintain a constant pressure on the cell to decouple and reduce the potential feedback between the pressure increase due the irreversible expansion and additional aging. The constant pressure is achieved using the springs with much lower spring modulus compared to the cell.

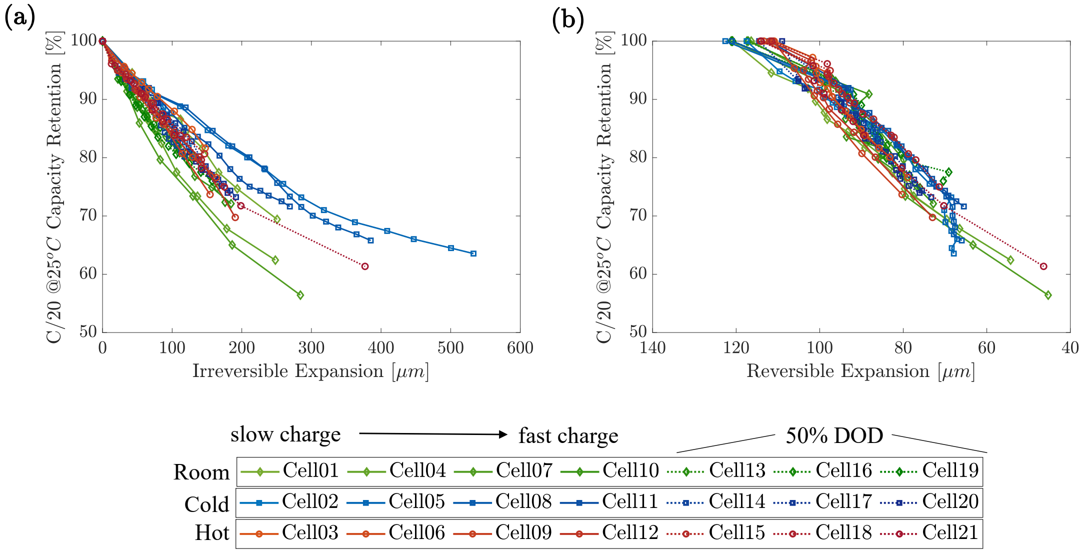

Figure 3.4: a) The capacity retention plotted as a function of the irreversible expansion, and b) the reversible expansion for all the cyclic aging conditions measured during the C/20 charge test at $25°C$. The curves in the plots are color coded such that the red, blue, and green colors indicate the aging condition at hot, cold, and room temperatures, respectively.

In the past works both irreversible [78, 84] and reversible [41, 85] expansion have been discussed as good indicators of SOH. At this point, however, a clear mathematical model for the irreversible expansion growth is not yet available for use in parametric identification. Moreover, Figure 3.4 (a) shows that the irreversible expansion does not have a simple correlation with capacity fade and requires separate training for each aging condition. On the contrary, the reversible expansion, has a well defined relationship to battery degradation modes [8]. The reversible expansion has features that, similar to the voltage signal, are connected to the phase transitions in the graphite. Additionally, the reversible expansion can be modeled with a relatively simple approach that is introduced in Section 2.3.

More importantly, Figure 3.4 (b) shows the strong and nearly linear correlation of the maximum reversible expansion with capacity for all the aging conditions. Since the intercalation expansion of graphite is much larger than the NMC [48], the reversible expansion response is largely a function of the graphite expansion. Therefore, the strong correlation of the maximum reversible expansion with capacity is contributed to the fact that LAM_{ne} at the negative electrode is the dominate aging mode. This statement is verified in the following sections by estimating the electrode specific state of health (eSOH).

3.3.3 Mechanistic electrode model validation

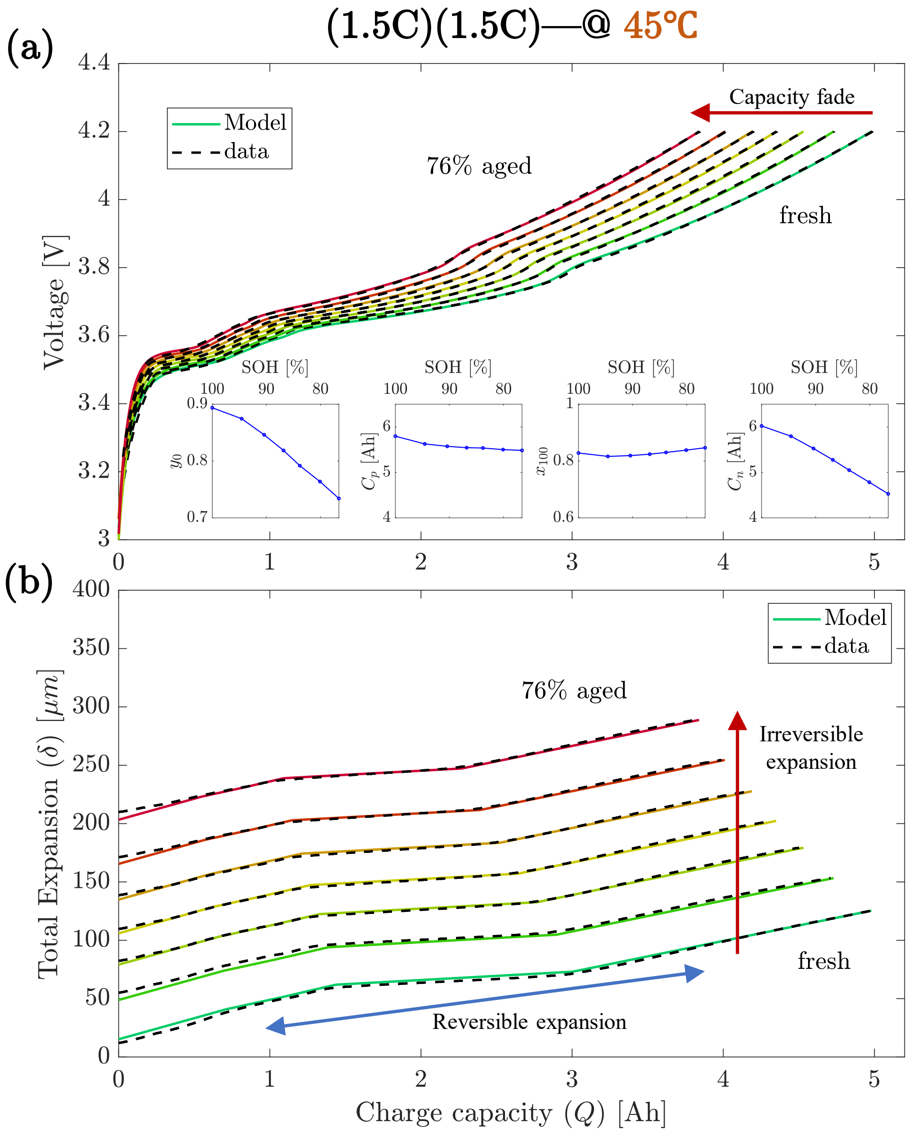

Figure 3.5: The results for the 1.5C @45°C condition, a) the voltage response during the C/20 charge test @25°C and the results of model fitting, b) The expansion response during the C/20 charge test @25°C and the results of model fitting. The lines are color coded from green (fresh) to red (most aged).

In this section, we show the details of the parametric estimation for one case with a full charge and discharge and also for reduced depth of discharge that is more expected in the field operation. It has been shown that a higher confidence level in estimating the eSOH parameters is achievable with the inclusion of expansion data [8]. Therefore, the advantages of the expansion is explored here by assuming a limited availability of data. Here, for the analysis of the benefits of the expansion, cell 06 (1.5C/1.5C $@45°C$) is selected. It should be pointed out that the analysis was applied to all the other conditions, and there was a similar results and conclusion. However, to avoid repetition and to keep the discussion more streamlined, the aforementioned condition was selected to showcase the results of the analysis.

The voltage and expansion evolution of cell 06 measured during C/20 RPTs are shown in Figure 3.5 (a) and (b). The fitting results for voltage and expansion are also shown in Figure 3.5 (a) and (b). It should be pointed out that the model only requires the thickness change of the cell with respect to a thickness at the start of a C/20 charge cycle, i.e. a partial or reduced data window of the reversible expansion. Furthermore, the cell capacity and the initial SOC are also assumed to be unknown. For clarity of the presentation, the fitting results are shown with the irreversible expansion added in Figure 3.5 (b). As can be seen, the identified models and the data are in good agreement at all the stages of aging. The fitted electrode parameters at every SOH is also shown inside the Figure 3.5 (a). The fitted model in Figure 3.5 (a) and (b) is achieved by utilizing the full data window (100-0% SOC) of both voltage and expansion. In Table 3.3, the estimated eSOH parameters using the full data window for the fresh and the most aged state are shown. These identified parameters are inferred to be the best estimated values since the full range of data is used for their estimation. For the reduced data window (90-40% SOC), the estimation is repeated once using only voltage and second time using voltage and expansion. The error percentage is calculated with respect to the full range values. It should be noted that in all of the cases the estimation is done using a global search option, where the optimization algorithm is done using a 100 randomly generated initial guesses within a predefined bound, and the estimated parameters with the least value of the root mean squared error are selected as the answer of the optimization. The upper bound for the C, C_n, and C_p parameters are set to the fresh cell values.

From Table 3.3, comparing the estimation error of the voltage only and voltage plus expansion, it is evident that estimation of negative electrode parameters, (x_{100}, C_n), and the capacity, C, suffers greatly using only the voltage. The estimation error is under 3% across the board for the expansion whereas for the voltage the estimation error is as high 13%. This large error is particularly important for the capacity, which is overestimated by 7.4%. As an example, for an electric vehicle with a 250 miles of range, the range would be overestimated by about 20 miles. On the other hand, the expansion produces accurate estimates even with a limited state of charge window, which enables fast and high-confidence diagnostics under limited data window scenarios. Furthermore, the expansion can facilitate more frequent capacity estimation and diagnostics for electric vehicles, where the state of charge window is often restricted and a deep depth of discharge rarely happens.

Aging state	Data range	Measurement type	Estimated parameters (error with respect to the full range values)				
			y_0	C_p [Ah]	x_{100}	C_n [Ah]	C [Ah]
Fresh	Full	Voltage+Expansion	0.88	5.80	0.82	6.02	4.97
76% aged	Full	Voltage+Expansion	0.73	5.48	0.84	4.52	3.84
76% aged	Reduced^a	Voltage	0.79 (+8.0%)	5.36 (-2.2%)	0.80 (-5.3%)	5.13 (+13.3%)	4.12 (+7.4%)
		Voltage+Expansion	0.74 (+1.0%)	5.32 (-2.8%)	0.85 (+1.5%)	4.44 (-2.0%)	3.82 (-0.5%)

Table 3.3: The results of estimation error analysis with a reduced data window, comparing the voltage only and voltage+expansion. The analysis is done for the Cell 06 (1.5C/1.5C $@45°C$). The error is calculated with respect to the aged values estimated using the full range of voltage and expansion data. ^{a} The Reduced data window corresponds to 90-40% SOC.

The large error estimation result of the voltage in Table 3.3 points to an underlying limitation of the voltage only estimations. Moreover, the large error is only for the negative electrode parameters, whereas, the positive electrode parameters are estimated with good accuracy. Also, the cell overall capacity has a large estimation error resulted from the poor estimation of the negative electrode parameters. It has shown in [8] that the observability of the eSOH parameters is related to the rate changes of the half-cell potential and expansion responses. The graphite has a very flat half-cell potential response in the high SOC region, which makes the voltage measurement less sensitive to the lithiation changes in the graphite. Meanwhile, the NMC half-cell potential rate changes with respect to lithiation state is non-zero over the whole SOC range. The poor observability of the graphite parameters compared to the NMC parameters is the direct result of the aforementioned difference in the potential responses. Contrary to the potential response, the rate changes of half-cell expansion of graphite with respect to the lithiation is non-zero, which makes the expansion measurement sensitive to the lithiation state of the graphite. Therefore, by including the expansion data we are able to increase the observability of graphite and the estimation accuracy of the eSOH parameters greatly.

3.3.4 eSOH estimation using reversible expansion

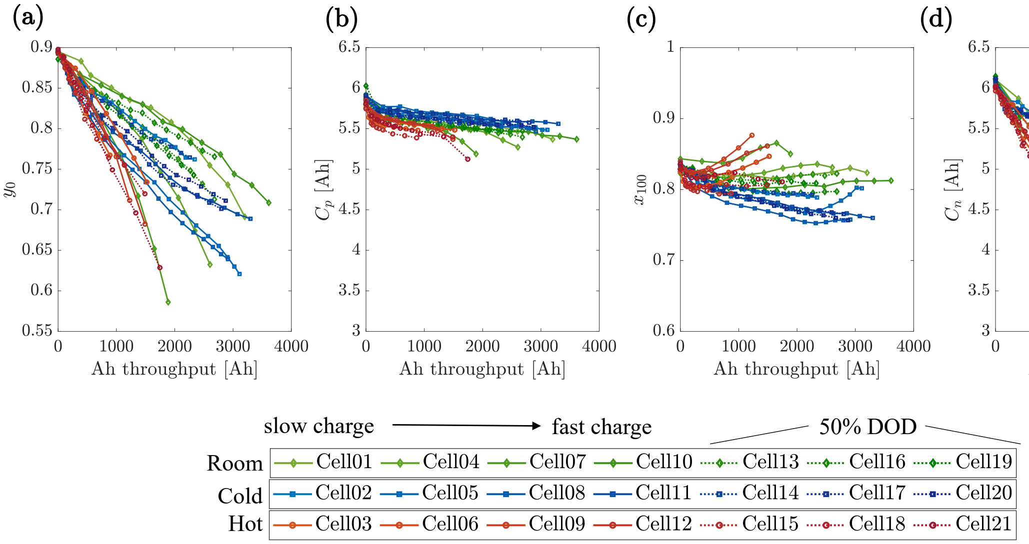

Figure 3.6: The evolution of eSOH parameters versus Ah throughput for all the cyclic aging conditions estimated using the C/20 charge test at $@25°C$, a) for y_0, b) for C_p, c) for x_{100}, and d) for C_n. The curves in the plots are color coded such that the red, blue, and green colors indicate the aging condition at hot, cold, and room temperatures, respectively.

In this section, the electrode level parameters are estimated for all the aging conditions. For this estimation the full range of voltage and expansion data is used. The estimated eSOH parameters for y_0, Cp, C_n, and x_{100} are presented in Figure 3.6 (a), (b), (c), and (d). The parameter y_{100} corresponding to the lithiation state of the positive electrode at full charge and the parameter

x_0 corresponding to the lithiation state of the negative electrode at full discharge do not change significantly during aging. As a result, they are not shown in Figure 3.6.

The maximum lithiation state of the positive electrode, y_0, decreases considerably for all the aging conditions in Figure 3.6 (a). These changes point to the fact that the Li inventory loss happens primarily during charging with (SEI growth and lithium plating). Since the negative electrode quickly becomes the limiting electrode during aging ($C_n/C_p < 1$), the lithium loss during charging leads to a shift (reduction) of y_0 in the subsequent discharges. The shifts in the maximum lithiation state of the negative electrode, x_{100}, demonstrate an interesting response in Figure 3.6 (c). The balance between loss of lithium inventory and loss of active material in the negative electrode governs the trajectory of x_{100}. When LLI is the dominate aging mode the x_{100} decreases and when the LAM is the dominate aging mode the x_{100} increases. In Figure 3.6 (c), for the hot temperature cells the x_{100} reduces initially and then quickly increases. For the room temperature cells the x_{100} is fairly unchanging overall, which points to a balance between LLI and LAM. For the cold temperature cells the x_{100} decreases indicating that LLI is the main aging mode.

The loss of active material in the negative electrode (graphite) in Figure 3.6 (d) is significantly more than the loss of active material in the positive electrode (NMC) in Figure 3.6 (b) for all the aging conditions. The active material loss can occur with particle cracking, separation, and isolation [81]. Particle cracking exposes fresh surface area to the electrolyte, which creates newly formed SEI layers. Therefore, a main reason for the increase in SEI growth is due to the increase in particle cracking at the later stages of aging [78]. The graphite is considered as a brittle material, which means that the increase and decrease of the internal stresses during cycling can lead to growth of cracks, fatigue failure and ultimately material separation. High charge-discharge rates also lead to a large stress gradient in the particles, which propagates the micro-crack formations. The temperature rise is also greater at high C-rates compared to low C-rates conditions inducing more SEI growth.

3.3.5 Effects of pressure on expansion and capacity retention

The impacts of applied pressure on the expansion and capacity fade is presented in this section. As explained in the experimental section, the fixtures were designed to retain the initial set-pressure during aging. This is achieved by utilizing springs with a low spring constants. As a result, the increase in pressure due to the irreversible expansion ($\approx 150\mu m$) is negligible compared to the applied pressure.

The results of the aging at various applied pressures (condition group H) are presented in Figure 3.7. In Figure 3.7 (a), the capacity retention is the cycle-to-cycle discharge capacity at 2C, similarly Figure 3.7 (b) shows the cycle-to-cycle growth of the irreversible expansion. As can be seen, overall the capacity retention is improved with increased pressure. Furthermore, the irreversible expansion decreases with the increase pressure. The most severe capacity fade and irreversible expansion happens for the cell at the lowest pressure (1 PSI). Since the cycling temperature is at $45°C$, the SEI growth is expected to be the primary aging mechanism [86]. The irreversible expansion is mainly due to the growth of the SEI layer, therefore, the results points to the fact that an ample applied pressure can suppress the growth of the SEI layer [78]. Additionally, this results reiterates the importance of applied pressure for the performance of lithium-ion cells and coupling between the mechanical and electrochemical processes.

As mentioned before, for the NMC-graphite cells tested in this study, the LAM at the negative electrode was the dominate aging mode (see Figure 3.6 (d)) under a variety of different aging conditions. Therefore, the capacity of the cell is determined by the limiting electrode, which is the graphite. Moreover, the cell reversible expansion response is also dominated by the graphite electrode, and the reduction of active material leads to a lower reversible electrode expansion as well. Similar to the results in Figure 3.4 (b) the reversible expansion has a linear relationship with the capacity retention for the different applied pressures shown in Figure 3.7 (c). In summary, the rate of change in the reversible expansion with respect to capacity fade is similar for all the applied pressures with higher pressures exhibiting a reduction of the maximum reversible expansion magnitude due to the larger compression. Overall, this result shows that the relationship between the

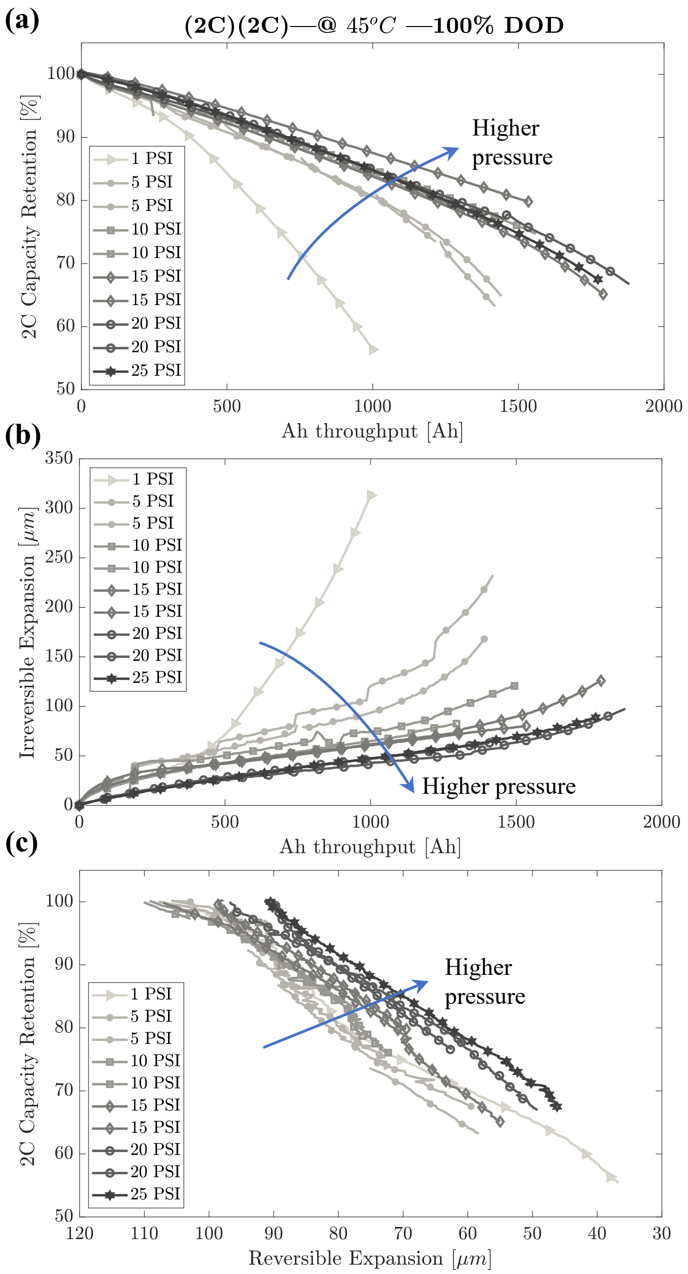

Figure 3.7: a) The 2C capacity retention and b) the irreversible expansion for the condition group H; aging at different applied pressures ranging from 1 to 25 PSI. c) The 2C capacity retention as a function of the reversible expansion. The measurements are made during the continues cycling.

reversible expansion and capacity fade holds for the cells cycled at different applied pressures as well.

3.3.6 The resistance growth and EIS

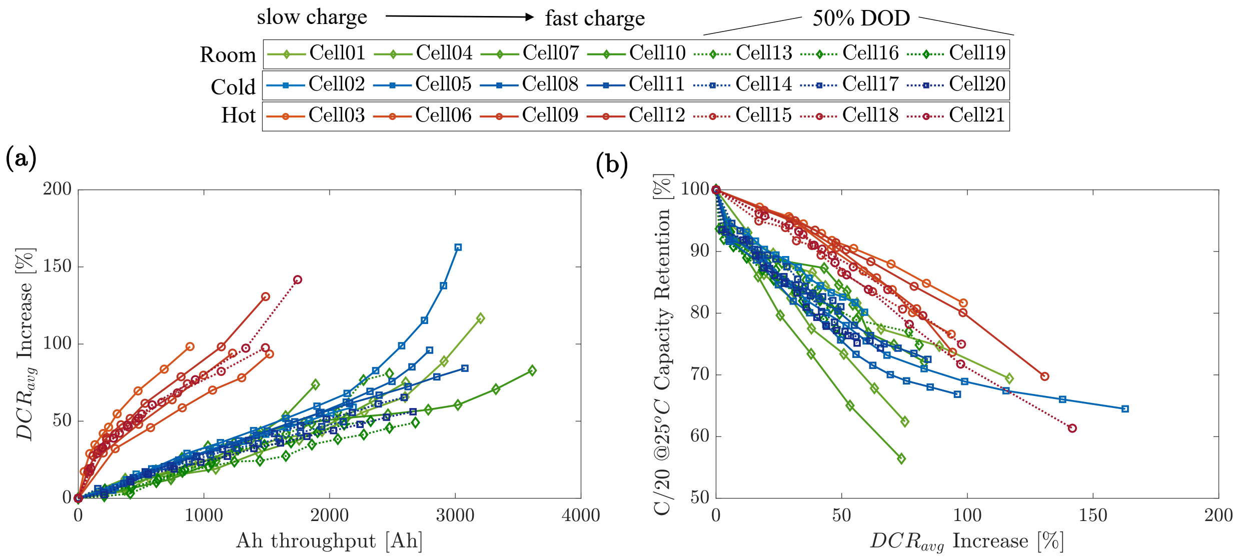

Figure 3.8: a) Direct current resistance (DCR) increase in percentage, averaged over the SOC range, versus Ah throughput for all the cyclic aging conditions. b) The capacity fade plotted as a function of the DCR for all the cyclic aging conditions. The DCR is calculated using the HPPC test. The curves in the plots are color coded such that the red, blue, and green colors indicate the aging condition at hot, cold, and room temperatures, respectively.

In this section, the resistance data is processed and is presented along with the EIS measurements to shed light on the primary aging mechanisms. The direct current resistance (DCR) is calculated using the HPPC data. Dividing the voltage drop after 1 s after each discharge and charge pulses by the current magnitude of 1C (5 A) gives the resistance values for the discharge and charge. The discharge and charge resistances are calculated at 10% SOC intervals and averaged to estimate the DCR. For reporting the resistance increase during aging the average value of the DCRs over the SOC range is used. Figure 3.8 (a) compares the DCR_{avg} increase for all the cyclic aging conditions.

Figure 3.8 (a) shows that the resistance increase is greater for the cells cycled at the hot temperature cells. This behavior is expected since the resistance is largely dependent on the SEI layer thickness and the SEI growth increases significantly at the high temperatures [86]. In Figure 3.8 (b), the capacity retention is plotted as a function of DCR increase. As can be seen, the resistance increase varies greatly with the aging conditions and the operating temperature. Therefore, despite popular belief, the resistance increase does not have a simple correlation with the capacity fade in a a similar way and it varies depending on the aging condition.

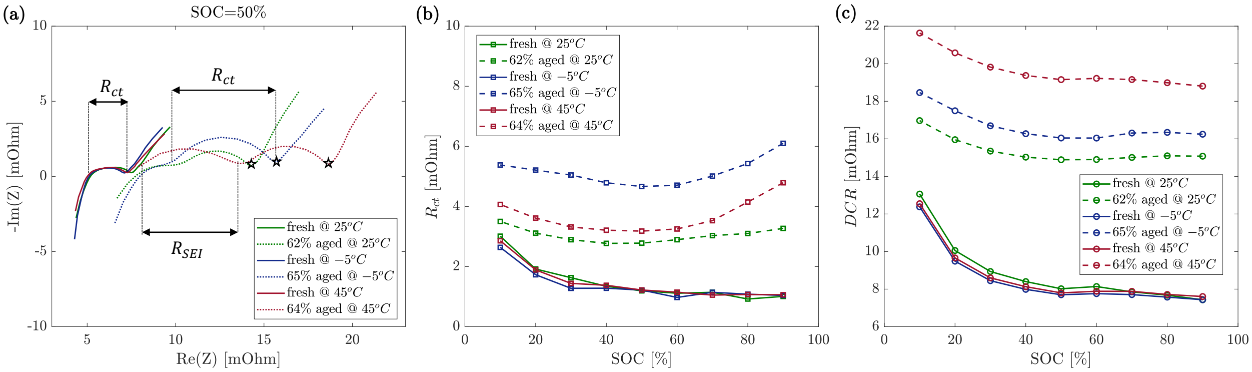

Figure 3.9: a) The Nyquist plot of the EIS data at the 50% SOC. The measurements are made at the room temperature. b) The charge-transfer resistance, R_{ct}, as a function of SOC. c) The direct-current resistance, DCR, as a function of SOC. The data is plotted at the fresh and aged states for the cells with (2C)(2C) condition cycled at $@25°C$, $@-5°C$, and $@45°C$.

The changes to the EIS data and DCR SOC dependency from the fresh to aged states are shown in Figure 3.9. The fast charging conditions (condition group C) are selected to show the effects of temperature on the evolution of resistance in Figure 3.9. The Nyquist plot of the EIS data of a lithium-ion battery has a characteristic shape with each part representing different dynamics inside cell. The relevant parts of the EIS response to the discussion in this paper are denoted in Figure 3.9 (a). The width of the semi-circle represents the charge-transfer resistance. For the hot temperature condition a second semi-circle is observable at the aged state. The existence of the second semi-circle is the evidence that a large degree of SEI is formed for the hot temperature condition [87]. The charge-transfer resistance, R_{ct}, is estimated using the EIS data at 10% SOC intervals and the results are shown in Figure 3.9 (b). The results suggest that the cold temperature cell has the largest increase in the charge-transfer resistance compared to the hot and room temperate cells. A higher increase of the R_{ct} for the cold temperature cell can be contributed to the presence of plated lithium. Since plated lithium reduces the accessible surface area of the graphite resulting in an increase of the charge-transfer resistance [88, 89].

The DRC SOC dependency in Figure 3.9 (c) shows that the resistance is larger at the lower SOCs. The largest changes to DCR are for the hot temperature cell, which is due to increased SEI layer growth and film resistance at hot temperatures. The DCR includes both the ohmic resistance and a portion of the charge-transfer resistance, and since DCR is calculated based on 1-second pulses, the contribution of the diffusion is negligible [90]. The estimated DCR is also approximately equal to the impedance at the transition point denoted with the star-shaped marker in Figure 3.9 (a). The charge-transfer resistance also depends on the concentration or lithiation state of the individual electrodes. At low SOCs, the lithiation state of the positive electrode (y_o) is close to fully lithiated. As a result, the large resistance near the discharge state is contributed to the positive electrode [91]. In Figure 3.9 (b), the difference between the resistance at the low SOCs and mid to high SOCs is lower at the aged state. This is partly contributed to the changes of the lithiation state of the positive electrode during aging (see Figure 3.6 (a)), which is also confirmed by the results in Figure 3.9 (b).

3.3.7 Differential expansion, voltage, and incremental capacity

In this section, the various signals based on differential analysis of the voltage and expansion measurements are introduced, and the features used in the study are described. Figure 3.10 (a) shows the testing procedure consist of cycling and periodic reference performance tests (RPTs). During the RPTs the voltage and expansion response are measured at various C-rates, as shown in Figure 3.10 (b). Then, the various differential signals are processed using filtering and a number of features are extracted.

The differential analysis is utilized in order to identify the prominent features in the expansion. The second differential of expansion (DE) with respect to charge displays distinct features such as local maximums and minimums. These features are the product of the various stages of phase transitions in the graphite anode [8]. The differential of voltage (DV) with respect to charge also exhibit similar features, and the connections of the DV and DE features to the graphite phase transitions has been reported previously [47, 48]. The distinct features in the DV signal such as

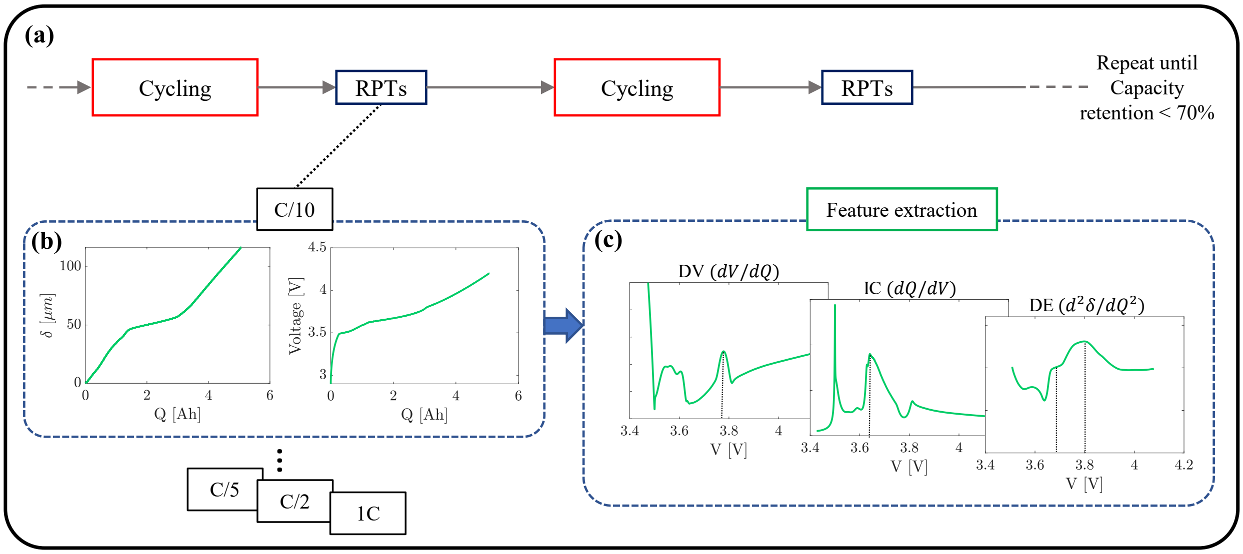

Figure 3.10: a) The testing procedure. b) The reference performance tests (RPTs) are done at approximately every 5% loss in capacity. The RPTs consist of a C/20 charge and discharge capacity measurement, charging at various C-rates from fully discharge state, and an hybrid pulse power characterization (HPPC) test for measuring the resistance. c) The incremental capacity (IC), differential expansion (DE), and voltage (DV) signals are extracted and filtered using the charging data at various C-rates.

voltage level at the peaks and also features in the incremental capacity (IC), which is the inverse of DV, have been utilized in capacity estimation methods [21, 22]. These feature are often quantified using a fixed constant current during charge or discharge. This paper systematically compares the expansion and voltage features measured at various constant charge currents. Also, the impact of partial charging is quantified by varying the initial SOC during charging tests. In the following, the various signals based on differential analysis of the voltage and expansion measurements are introduced, and the features of interest are described.

Figure 3.11 (b) shows a measurement of the voltage and expansion during charging at C/10. In this case, the measurements are from cell 01 at the fresh state. The differential voltage (DV) is defined as the derivative of the voltage, V, with respect to the amount of input-charge, Q. The DV signal is plotted in Figure 3.11 (a). The DV signal displays distinct features such as local maximums that are often referred to as peaks in the literature. These peaks are the product of the various stages of phase transitions in the graphite anode [8].

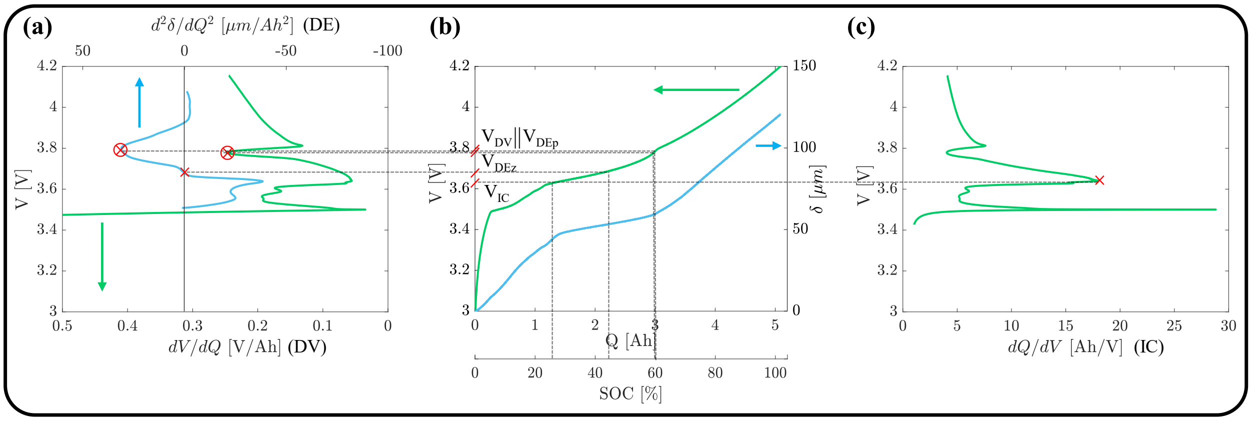

Figure 3.11: a) The differential voltage and expansion. b) The voltage and expansion during charging at C/10. c) The incremental capacity. The selected feature in differential voltage (DV) is the voltage at the peak observed about the 60% SOC. The selected feature in differential expansion (DE) is the voltage at the zero cross over point observed about the 45% SOC. The selected features in incremental capacity (IC) are the voltage and the height of the peak observed about the 25% SOC.

Next, the differential expansion (DE) is defined as the second derivative of the expansion, δ, with respect to the amount of input-charge, Q. The DE signal is also plotted in Figure 3.11 (a). Similar to the DV, the DE signal has features that correspond to the phase transitions in the graphite anode [47, 48]. In fact, the peaks observed in the DE signal and DV signal occur at the same location in voltage, indicating that these features are fundamentally pointing towards the same graphite phase transitions.

Lastly, the incremental capacity (IC) is defined as the derivative of the amount of input-charge, Q, with respect to voltage, V (i.e., the inverse of the DV). The IC signal is plotted in Figure 3.11 (c). The peaks in the IC signal correspond to the local minimums in the DV signal. Here, the signals are plotted on the x-axis, and the voltage is plotted on the y-axis. This is to aid in illustrating the location of the features in the voltage curve and their corresponding SOC values.

As can be seen from Figure 3.11 (a) and (c), several distinct features can be used for each of the signals. For example, the measured voltage at any of the peaks or their height. Nevertheless, the most important criteria for selecting a feature is its correlation factor with the capacity. In other words, the feature should maintain a strong correlation with capacity retention that is invariant to the cycling conditions. Furthermore, the feature needs to be insensitive to the initial SOC, and the correlation should remain strong at various C-rates. It is also desirable that the feature appears at SOC ranges that most electric or hybrid vehicles usually operate in, meaning the feature should not require or occur at a high depth of discharge (SOC $< 20\%$). These conditions are essential for the relevance of the capacity estimation method for real-world applications.

Based on these criteria and the experimental results, several prominent features are selected, which are marked in Figure 3.11 (a) and (c). For the IC signal, the measured voltage, V_{IC}, at the peak occurring about 25% SOC and its height, H_{IC}. For the DE signal, the measured voltage, V_{DEp}, at the peak, occurring about 60% SOC and the zero crossover point ($d^2\delta/dQ^2 = 0$), V_{DEz}, occurring about 45% SOC. For the DV signal, the measured voltage, V_{DV}, at the peak, occurring about 60% SOC. In the following sections, the correlation of these features with capacity and their sensitivity to the charge conditions are presented.

3.3.8 Evolution of the differential signals at different C-rates

As mentioned in the experimental section, charge data were collected during the C-rate dependency tests at various aging intervals. After collecting this data, the DV, IC, and DE signal are processed using the Savitsky-Golay (SG) filtering technique [92]. In this filtering method, a polynomial is fitted to a moving frame of the data. Selecting a suitable polynomial order and data frame length depends on the noise levels and the number of available data points. Generally, lower-order polynomials and larger data frames lead to more filtering. In this work, polynomial order of three is selected. The data acquisition frequency is fixed at 0.1 Hz. This means that charging at higher C-rates results in a fewer number of data points. It was discovered that a fixed SOC window for data frame size leads to more consistent filtering compared to a fixed number of data points. Therefore, for different C-rates, the frame length is always set to the number of data points equivalent to a 5% SOC window.

As an example, the evolution of the DE, DV, and IC signals of cell 04 (1.5C/1.5C $@25°C$) during aging is shown in Figure 3.12 (a), (b), and (c), respectively. For each signal, the evolution

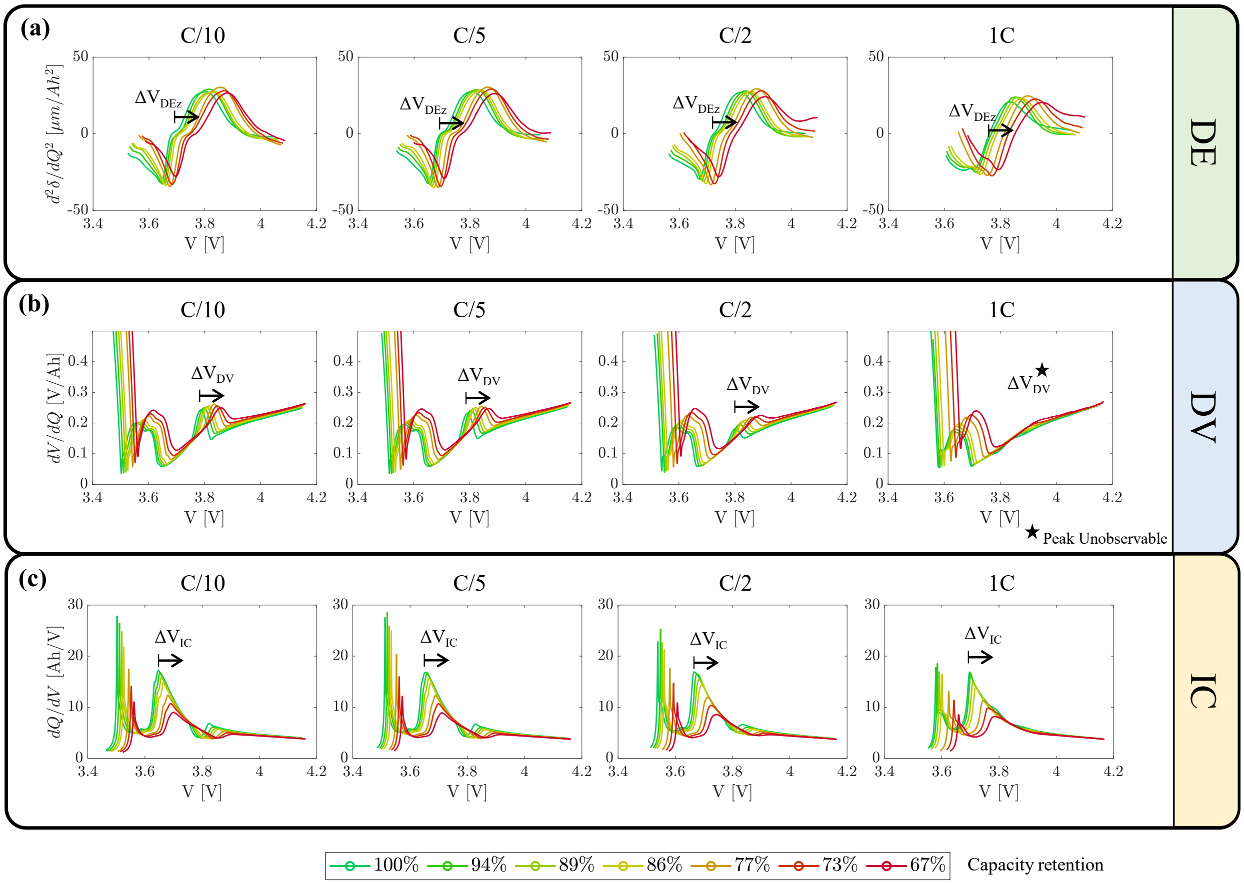

Figure 3.12: a) The evolution of the differential expansion (DE), b) the differential voltage (DV), and c) the incremental capacity (IC) signals for the cell 04 (1.5C/1.5C @25°C) at various C-rates during aging. Note that at 1C the peak in DV is unobservable. The lines are color coded from green (fresh) to red (most aged).

is shown for the C/10, C/5, C/2, and 1C. The lines in Figure 3.12 are colored from green to red for fresh to aged. Note that in Figure 3.12 (b), the height of the DV peak diminishes considerably at 1C, which makes detection of this peak infeasible. It is also observable that all signals are shifting to higher voltages with aging. This change is about 60 mV for the C/10 rate and about 100 mV for 1C rate at the maximum. The resistance increase is partially responsible for this change. The resistance increase at the end of life was about 8 mΩ (see Figure 3.8 (a)), which translates to a 4 mV and 40 mV shift of the signals due to resistance increase at C/10 and 1C, respectively. Therefore, at low C-rates, the impact of the resistance increase is much lower on the voltage shift, and in fact, the majority of this voltage shift is from the changes of the operating stoichiometric window of the electrodes.

The same behavior observed in Figure 3.14 (b) is also happening in the experimental data shown in Figure 3.12. Therefore, in essence, tracking the shifts in the DV, IC, and DE signals to higher voltages are capturing the underlying degradation of individual electrodes during aging. Additionally, both in the experimental IC signals of Figure 3.12 (c) and the modeling results of Figure 3.14 (b), the height of the peak in the IC signal decreases with aging. This is expected as the area under the IC curve is equal to charge-capacity. Therefore, overall the IC curve magnitude should decrease with aging.

3.3.9 Sensitivity of the differential signals during charging to different initial SOCs

The goal here is to assess the sensitivity of the signals (and their features) to the initial SOC of the charge. The test was done after the termination of the cycling experiment with the cell at approximately 70% capacity retention (see Section 3.2 for detailed steps). The experiment was done with respect to three different initial SOC of 5%, 20%, and 40%, and was repeated with various C-rates. The results of this experiment for cell 04 are presented in Figure 3.13. The DE, DV, and IC signals at various C-rates are shown in Figure 3.13 (a), (b), and (c), respectively. For the DE signal, the zero crossover point is detectable with 5% and 20% initial SOC. The voltage values of this feature, V_{DEz}, are presented in Table 3.4 with the maximum error of 5 mV observed at 1C. However, large deviations are observable for the location, V_{DEp}, and height of the DE peak.

In Figure 3.13 (b), for the DV signal the peak is detectable with 5%, 20%, and 40% initial SOC. Similar to the results of Figure 3.12 (b), which has a charge starting from a full depth of the discharge, the peak is still not observable at 1C. The voltage values of the peak, V_{DV}, at lower C-rates are available in Table 3.5 with a maximum error of 5 mV observed at C/2. Nevertheless, similar to the DE peak, a large variation of the peak height is observed depending on the initial SOC. The peak in IC signal in Figure 3.12 (c) is detectable with 5% and 20% initial SOC. The voltage values, V_{IC}, of the peak, are presented in Table 3.6 with the maximum error of 2 mV

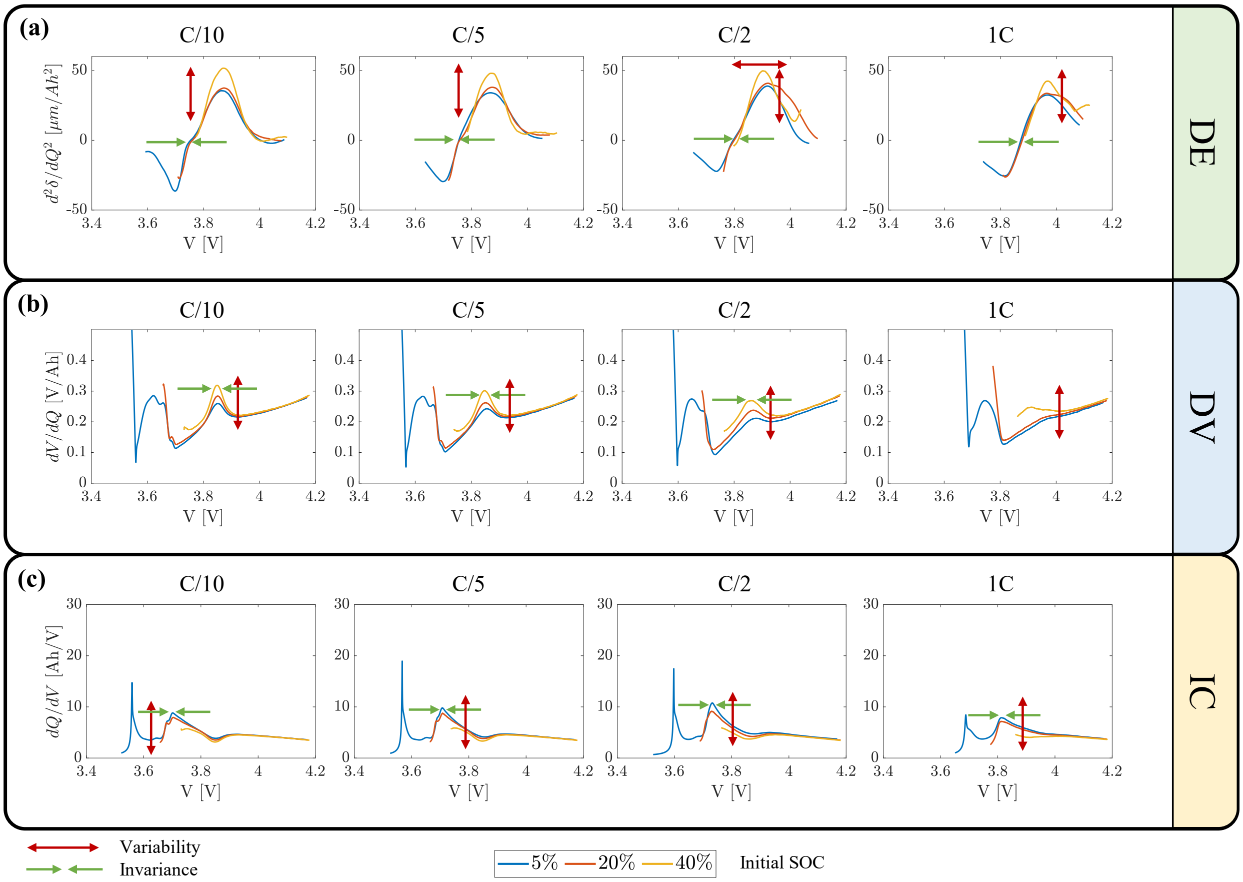

Figure 3.13: a) The charge response of the DE, b) DV, and c) IC signals with respect to the initial SOC at various C-rates. The signals are plotted for the 5%, 20%, and 40% initial SOC. Note that the height of the peaks in DE, DV, and IC curve varies greatly depending on the initial SOC. The location of the peak in the DV and IC signals is consistence regardless of the initial SOC. Moreover, the zero crossover point of the DE signal also remains unchanged by the initial SOC.

observed at 1C. Here as well, the height of the peak, H_{IC}, changes with respect to the initial SOC.

	V_{DEz} [V]			
Initial SOC	C/10	C/5	C/2	1C
5%	3.7537	3.7549	3.7729	3.8732
20%	3.7572	3.7578	3.7759	3.8783
40%	-	-	-	-
max. abs. error	0.0035	0.0029	0.0030	0.0051

Table 3.4: The measured voltage of the zero-crossing feature of the DE signal at different C-rates and initial SOCs. The absolute maximum difference between the measurement voltages is also included. Note that with a 40% initial SOC the feature was not detectable.

	V_{DV} [V]			
Initial SOC	C/10	C/5	C/2	1C
5%	3.8483	3.8489	3.8596	-
20%	3.8495	3.8454	3.8618	-
40%	3.8483	3.8460	3.8569	-
max. abs. error	0.0015	0.0035	0.0049	-

Table 3.5: The measured voltage of the peak feature of the DV signal at different C-rates and initial SOCs. The absolute maximum difference between the measurement voltages is also included. Note that at 1C rate the feature was not detectable.

	V_{IC} [V]			
Initial SOC	C/10	C/5	C/2	1C
5%	3.7014	3.7073	3.7319	3.8131
20%	3.7034	3.7084	3.7298	3.8119
40%	-	-	-	-
max. abs. error	0.0020	0.0011	0.0021	0.0022

Table 3.6: The measured voltage of the peak feature of the IC signal at different C-rates and initial SOCs. The absolute maximum difference between the measurement voltages is also included. Note that with a 40% initial SOC the feature was not detectable.

3.3.10 Evolution of differential signal from the mechanistic model perspective

As mentioned earlier, the capacity fade is due to the LLI and LAM. Often the capacity fade is significantly more at the negative electrode compared to the positive electrode. This is because the LLI is mainly due to side reactions of SEI growth and lithium plating at the negative electrode (graphite). Furthermore, the LAM can occur with particle cracking, separation, and isolation [81]. Particle cracking exposes fresh surface area to the electrolyte, which creates newly formed SEI layers. Therefore, the main reason for the increase in SEI growth is due to the increase in particle cracking [78]. Graphite is considered a brittle material, which means that the increase and decrease of the internal stresses during cycling can lead to the growth of cracks, fatigue failure, and ultimately material separation. High charge-discharge rates lead to large stress gradients in the particles, which propagates the micro-crack formations. The temperature rise is also more significant

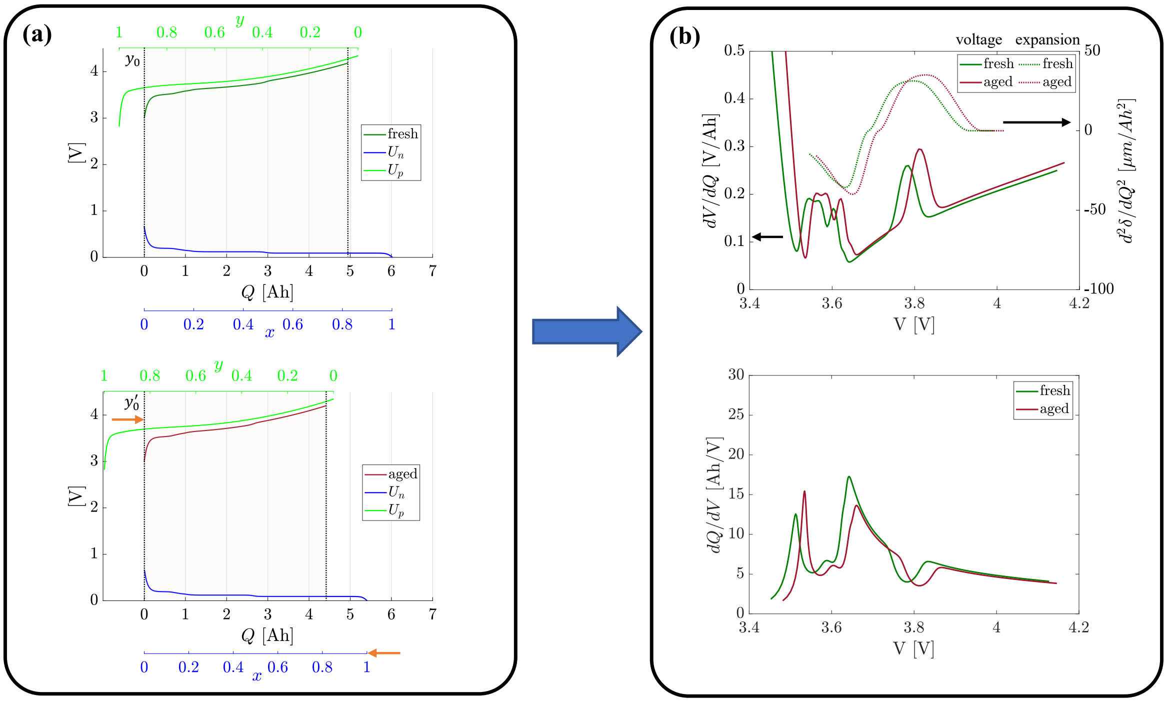

Figure 3.14: a) Mechanistic model of the changes to the OCV during aging. Notice the shift of the operating window of the positive electrode to higher potentials. b) The DV, DE, and IC signals of the fresh and aged states. The aged signals are moved to a higher voltages. The decrease in the magnitude of the IC signal is also related to the 10% capacity fade of from fresh to aged state.

at high C-rate than low C-rate conditions, which induces more SEI growth.

The LLI and LAM over the lifetime of the battery alter the open circuit voltage (OCV). The measured OCV is equal to the potential difference of the positive (U_p) and negative (U_n) electrode. The specific shape of the OCV curve is a function of the operating stoichiometric window and the relative capacity of the electrodes, which also depend on the LLI and LAM. Detailed modeling of the OCV and expansion can be found in Ref. [8]. Figure 3.14 (a) shows a simulation that is done to study the OCV changes during aging due to LLI and LAM. The potential functions of the negative and positive electrodes are taken from Ref. [48]. The capacity fade, in this case, was about 10%. The LAM at the negative electrode and LLI caused a shift of the stoichiometric window of the positive electrode (y_0) to higher potentials. As a result, as shown in Figure 3.14 (b), the DV, DE, and IC signals are moved to a higher voltage at the aged state.

3.3.11 Correlations between the differential signal features and capacity

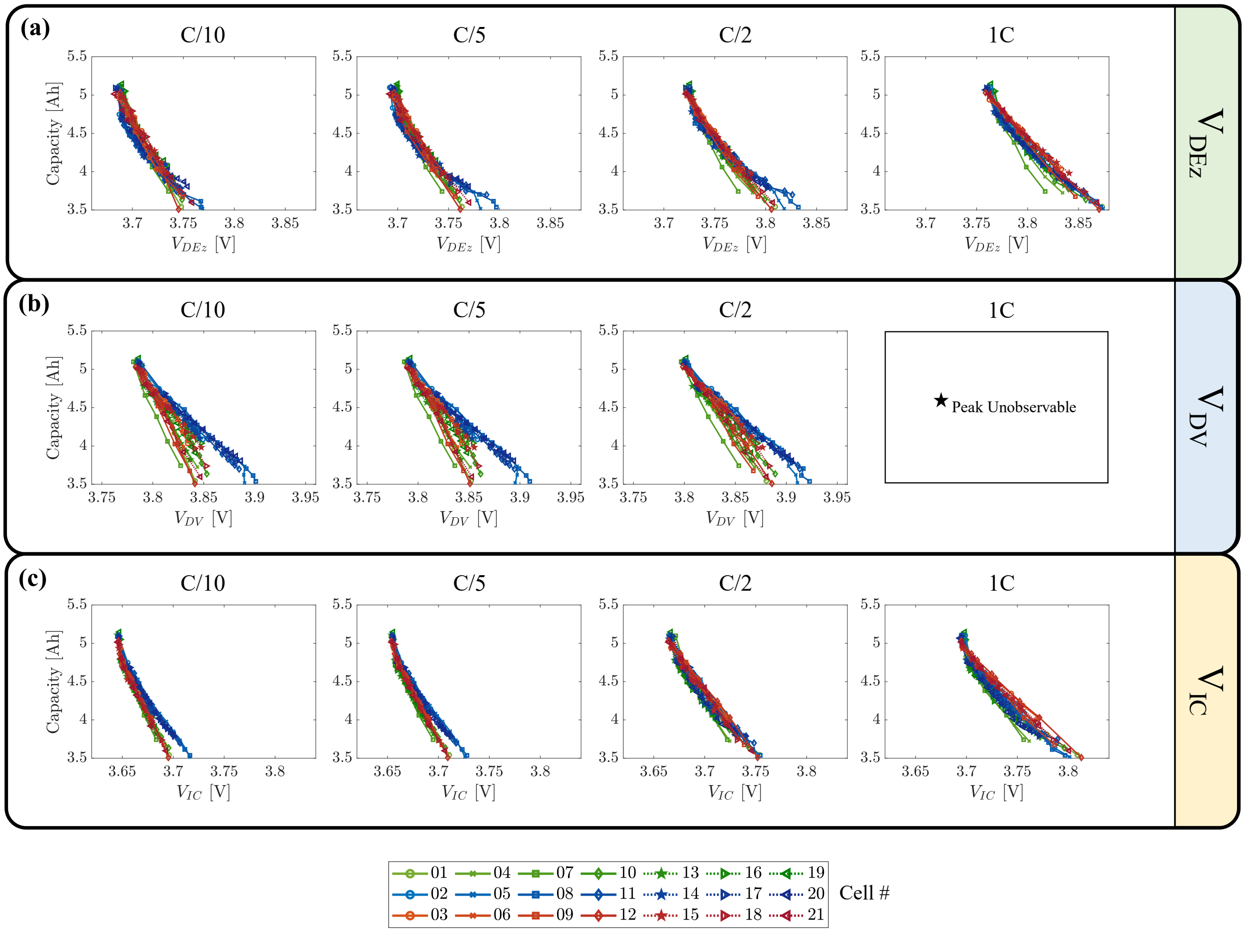

Figure 3.15: a) The evolution of the DE feature, V_{DEz}, b) the DV feature, V_{DV}, and c) the IC feature, V_{IC}, for all the aging conditions. The evolution of the features are plotted for different C-rates. At 1C the DV feature was not detectable, therefore, this C-rate is not included in the plot. The data is color coded such that the red, blue, and green colors correspond to the aging condition at hot, cold, and room temperatures, respectively.

As noted in Figure 3.11 the primary features selected in this study are the voltage at the peak of the DV and IC signals and zero crossover voltage of the DE signal. Other potential features are the height of the peaks in the DV and IC signals. However, as discussed earlier, the heights of these peaks are sensitive to the initial SOC, and therefore not suitable for robust capacity estimation. The features below 20% were also not considered since to observe these features, a high depth of discharge is required. Additionally, the peak in the DE signal was also not robust with respect to the initial SOC. It should be mentioned that since the charge C-rate dependency data was collected with the same full depth of discharge as the initial SOC, the evolution of the IC peak height and the voltage of the DE peak also shows a good degree of correlation with the capacity (see Figure 3.16). However, due to the sensitivity of these features to the initial SOC, these features are not considered for the development of capacity estimation methods.

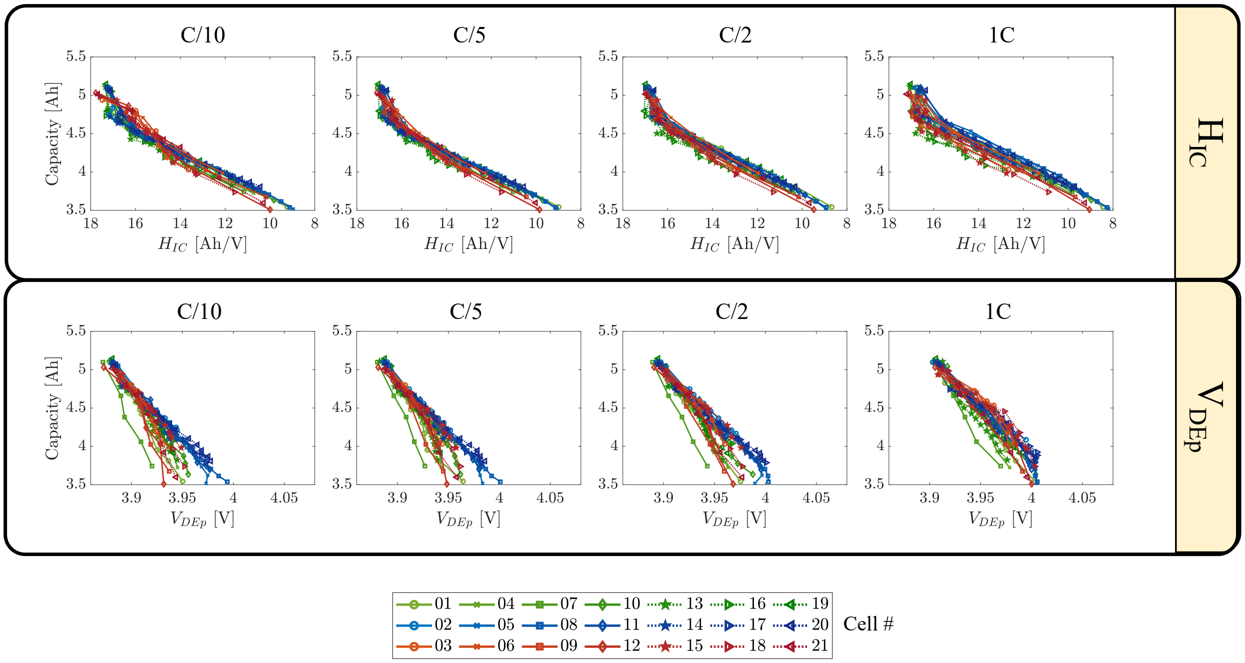

Figure 3.16: a) The evolution of the height of the IC feature, H_{IC} and b) the peak voltage of the DE signal, V_{DEp}, for all the aging conditions. The evolution of the features are plotted for different C-rates. The data is color coded such that the red, blue, and green colors correspond to the aging condition at hot, cold, and room temperatures, respectively.

Figure 3.15 shows the evolution of the selected features during aging for all the aging conditions. All three features have a good correlation with capacity. Similar to Figure 3.3 (a), the capacity in Figure 3.15 is measured during the C/20 diagnostic test. Based on these results, each of the features can be used and are a good candidate for a capacity estimation method. Comparing the DV feature in Figure 3.15 (b) with the other two features, it is evident that there is larger distribution in the evolution of this feature among the aging conditions. It is also observed in Figure 3.15 (b) that the DV feature deviated from the linear evolution close to the end of the cyclic experiment

($\approx$ 70%) for the cells 05 and 08. This is noteworthy as these cells also exhibit the accelerated aging at the same time in Figure 3.3 (b). Therefore, it may be possible to utilize the V_{DV} to detect the occurrence of the acceleration of capacity fade, which is also referred to as a *kneepoint* in the literature. However, verifying this observation and development of kneepoint detection methods requires further investigation, and it is beyond the scope of this work.

From the results in Figure 3.15, it is clear that the selected features have a strong correlation with the capacity that is highly independent of the vast array of aging conditions tested in this study. Thus, these features are great candidates for developing capacity estimation methods based on simple linear regression models. Furthermore, it is possible to combine these features to develop more robust capacity estimation methods. Therefore, various combinations of the features are also considered. In order to assess the goodness of the linear regression models the root mean square error (RMSE) of the fits are compared. The RMSE is normalized by the nominal capacity of 5 Ah and is akin to an absolute error in estimating SOH. The linear regression models are fitted using all the data at each C-rate independently. The detailed results of the fitting for the C/5 and 1C are shown in Table 3.7. The DCR data is also used as a feature to develop a linear regression model and the results are reported in Table 3.7.

	RMSE/Q_{nom} [%]		
Features	C/5	1C	Required SOC range
V_{DV}	3.57	-	55%—65%
V_{DEz}	2.68	1.94	40%—50%
V_{IC}	2.36	2.21	20%—30%
V_{DV}, V_{IC}	2.28	-	20%—65%
V_{IC} , V_{DEz}	2.26	1.95	20%—50%
V_{DV}, V_{DEz}	2.54	-	40%—65%
V_{DV}, V_{IC}, V_{DEz}	2.22	-	20%—65%
DCR	4.17		-

Table 3.7: RMSE values of the linear regression fit using different feature sets for all the conditions

In terms of single features, the expansion feature, V_{DEz}, at 1C has the lowest absolute error of 1.9% for capacity estimation. Additionally, this feature remains observable up to 1C and occurs at about 50% SOC. At C/5, combination of the V_{DEz} with V_{IC}, improves the accuracy of the capacity estimation method considerably. As can be seen from the results in Table 3.7 the combination of all the features has the best correlation with the capacity. However, as noted previously, the DV feature is not observable at 1C. Therefore, capacity estimation models with the DV features are only possible if the charging C-rates are below C/2. The required SOC range is also essential for the applicability of the estimation method for fast characterization. Methods that require shorter SOC ranges, rely on features from the middle of the entire SOC range, and are applicable at 1C are more desirable. In this sense, the expansion feature, V_{DEz}, fulfills all the aforementioned requirements.

As evident from the results of Table 3.7, capacity estimation using DCR has a large error since the evolution of average DCR is strongly dependent on the cycling conditions. The correlation of average DCR and capacity is shown in Figure 3.8 (b). On the other hand, measurement of the resistance can effectively be done at any SOC by applying a prescribed short-duration charge or discharge pulse. Nevertheless, particular attention to the effects of aging conditions is needed if one wants to utilize DCR reliably for capacity estimation.

Finally, it should be noted that in order to develop capacity estimation methods for cells with different chemistry or construction, it is necessary to collect the aging data. However, as demonstrated in this study, the correlation of the voltage and expansion features in Table 3.7 with capacity is largely independent of the aging conditions. Therefore, the data collection can be done using an accelerated aging condition like the (2C/2C) at hot temperature to significantly reduce testing time.

3.4 Summary

In this work, we demonstrated that incorporating the cell expansion is a powerful tool for electrode specific health estimation and diagnostics. We showed that the changes in the reversible expansion as the cell ages are more pronounced compared to the voltage measurements, which leads to a higher-confidence estimation of cell health parameters with a reduced data range. Moreover, the mechanistic model developed for electrode state of health estimation was able to capture the voltage and expansion evolution under variety of conditions such as temperature, charging rate, depth of discharge, and pressure. To develop a capacity estimation method based on voltage and expansion, the charge response of the cell was recorded periodically with different C-rates. The features and characteristics of the DV, IC, and DE signals and their evolution with capacity fade were presented. Based on the results of sensitivity of the feature with respect to the initial SOC, a number of features were selected for developing capacity estimation methods. Different linear regression models were fitted to the data by considering all the combinations of the features. It was discovered that utilizing the IC and DE features results in the best method for capacity estimation in terms of accuracy.

CHAPTER 4

A Reduced Order Electrochemical and Mechanical Model Applicable to Differential Analysis

4.1 Introduction

As can be seen in Figure 4.1, as the C-rate increases there is an appreciable shift in the location and reduction of height for these peaks. Furthermore, at 1C the peaks are effectively flattened and are unobservable. The same analysis in Figure 4.1 is done for the cell expansion. The peaks in the second differential of the expansion correspond to the same peaks in the differential voltage [93], since they also result from the same phase transitions in the graphite. Therefore, in principle, we can apply that same method of peak alignment using the peaks in the second derivative of expansion. Moreover, there are some advantages in using expansion, namely, as it can be seen from Figure 4.1, the second peak remains observable up to 1C, which is important for application of this method at fast charging rates.

In this chapter, the overarching goal is to capture the observation in Figure 4.1, which is the smoothing of the peaks in dV/dQ and retention of the peaks in $d^2\delta/dQ^2$ at higher C-rates. The retention of the peaks at higher charging rates enables better estimation of the cell capacity. To achieve this goal a reduced order electrochemical and mechanical model is developed. Compared to other reduced order electrochemical models such as single particle model with electrolyte (SPMe), which has a single particle representation of the solid electrode, in our model, we consider multiple particles with a size distribution. The main contribution of this chapter is the addition of the mechanical/expansion model, which has the same particle size distribution of the electrochemical model. This allows us to capture the smoothing and preservation of the phase transitions in the voltage and expansion measurements at high C-rates, respectively.

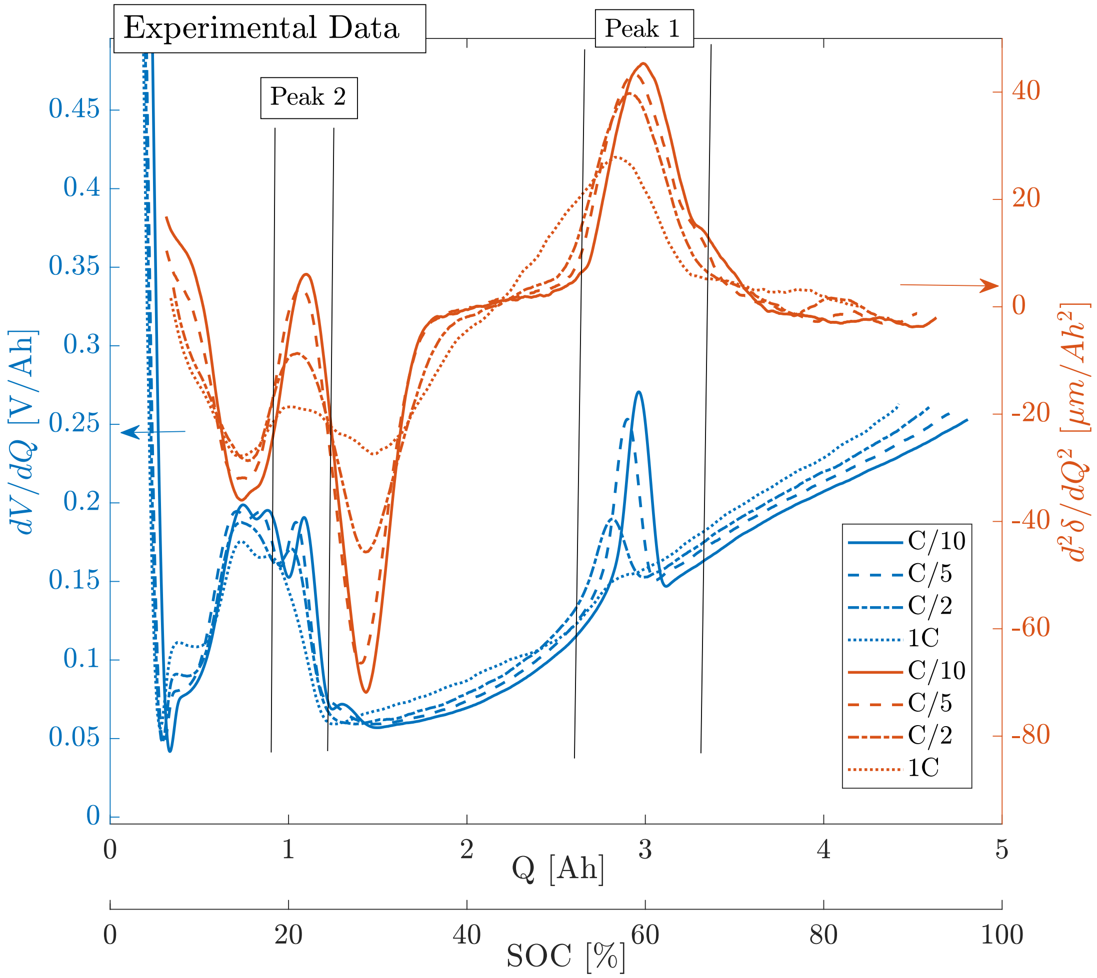

Figure 4.1: Differential voltage and expansion at different charging rates, showing that the peaks in the voltage derivative curve and the second derivative of the expansion curve occur at the to the same phase transitions in the material. Note that the peak 1 is unobservable at 1C for voltage, whereas it remains observable at this rate for expansion.

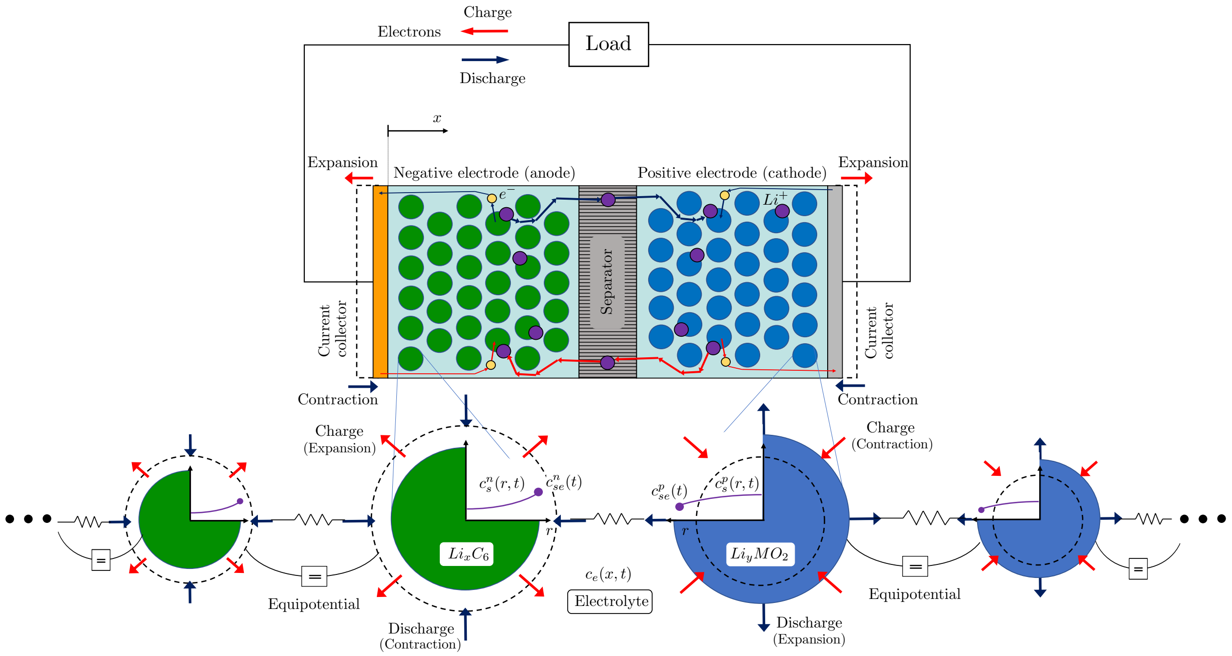

Figure 4.2: The schematics of the Multiparticle electrochemical and mechanical model.

4.2 Model Development

4.2.1 Electrochemical Model

The electrochemical model in this section is primary based on the well known Doyle Fuller Newman (DFN) model. As mentioned in the introduction, the distribution of particle size for the graphite electrode is considered here. A model for electrodes with multiple materials has been proposed in [94]. The treatment of multiple particle sizes is similar to models with multiple materials, with only difference being the fact that instead of multiple materials there are multiple particle sizes of the same material. The model schematics is shown in Figure 4.2. For generality the particle size distribution is considered for both positive and negative electrodes in the model description below, although in practice we only considered a particle distribution in the negative electrode.

4.2.1.1 Full order model

The multiparticle DFN (MP-DFN) model is presented here. The main difference in MP-DFN model is that at each point in the x direction instead of the single particle configuration, there are multiple particles with a size distribution. The particle size distribution is the same along the length of the electrode. In the following equations the symbol $(*)$ is a place holder for either positive (p) or negative (n) electrodes. The number of particle sizes is denoted by N_*^R. The particle (i) represents the particles with size $R_{p,i}^*$. The lithium concentration, $(c_{s,i})$, for each particle (i) is given by the following solid diffusion equations

$$\frac{\partial c_{s,i}^*}{\partial t}(x,r,t) = \frac{1}{r^2}\frac{1}{\partial r}\left[D_{s,i}^* r^2 \frac{\partial c_{s,i}^*}{\partial r}(x,r,t)\right], \tag{4.1}$$

$$\frac{\partial c_{s,i}^*}{\partial r}(x,0,t) = 0, \tag{4.2}$$

$$D_{s,i}^* \frac{\partial c_{s,i}^*}{\partial r}(x,R_{p,i}^*,t) = -j_i^*(x,t), \tag{4.3}$$

where j_i is the pore wall flux between electrolyte and the solid, and D_s is the solid state diffusion coefficient. The Butler-Volmer equation is given by

$$j_i^*(x,t) = \frac{i_{0,i}^*(x,t)}{F}\left(e^{\frac{\alpha_a F}{RT}\eta_i^*(x,t)} - e^{\frac{-\alpha_c F}{RT}\eta_i^*(x,t)}\right), \tag{4.4}$$

$$i_{0,i}^*(x,t) = k_0^*(c_e(x,t))^{\alpha_a}(c_{s,max,i}^* - c_{se,i}^*(x,t))^{\alpha_a}(c_{se,i}^*(x,t))^{\alpha_c}, \tag{4.5}$$

where $c_{se,i}^*(x,t) = c_{s,i}^*(x,R_{p,i}^*,t)$ is the concentration at the surface of the particle, the k_0 is the reaction rate constant, the (α_a, α_c) are the charge transfer coefficients, and $\eta_i^*(x,t)$ is the surface overpotential given by

$$\eta_i^*(x,t) = \Phi_1(x,t) - \Phi_2(x,t) - U_*(c_{se,i}^*(x,t)) - V_{f,i}^*(x,t), \tag{4.6}$$

where Φ_1 is the potential of the solid, Φ_2 is the potential of electrolyte, U is the half-cell open circuit potential. The $V_{f,i}^*(x,t) = ASR_{f,i}^* F j_i^*(x,t)$ is the voltage drop due to the film resistance, where ASR_f is the area specific resistance. The modified current balance is as follows

$$\begin{cases} \nabla \, . \, i_2(x,t) = \sum_{i=1}^{N_n^R} a_i^n F j_i^n(x,t) & 0 \leq x < l_n, \\ \nabla \, . \, i_2(x,t) = 0 & l_n \leq x \leq l_n + l_s, \\ \nabla \, . \, i_2(x,t) = \sum_{i=1}^{N_p^R} a_i^p F j_i^p(x,t) & l_n + l_s < x \leq l_c, \end{cases} \tag{4.7}$$

where i_2 is the current density in the electrolyte, the a_i is the active interfacial surface area of particle (i) per electrode unit volume, and the $l_c = l_n + l_s + l_p$ is denoting the total length of the cell. The boundary conditions are the continuity of i_2, and $i_2(0,t) = i_2(l_c,t) = 0$. The following equations remain unchanged from the DFN model. The electrolyte material balance is

$$\epsilon_2^{**} \frac{\partial c_e}{\partial t}(x,t) = \nabla \, . \, (D_e^{eff} \nabla c_e(x,t)) + \frac{1 - t_+^0}{F} \nabla \, . \, i_2(x,t) - \frac{i_2 \, . \, \nabla t_+^0}{F}(x,t), \tag{4.8}$$

where the symbol $(**)$ can be (p), (n), and (s) for positive electrode, negative electrode, and separator regions, ϵ_2 is the porosity, t_+^0 is the transference number of Li ions, and the $D_e^{eff} = D_e(\epsilon_2^{**})^{brug}$ is the effective electrolyte diffusion coefficient. The boundary conditions are continuity of c_e, and $\nabla c_e(0,t) = \nabla c_e(l_c,t) = 0$. The liquid-phase Ohm's law is

$$i_2(x,t) = -\kappa^{eff} \nabla \Phi_2(x,t) + \frac{2\kappa^{eff} RT}{F}(1 - t_+^0) \left(1 + \frac{d \, ln \, f_\pm}{d \, ln \, c_e}(x,t)\right) \nabla (ln \, c_e)(x,t), \tag{4.9}$$

where $f_\pm$ is the mean molar activity coefficient in the electrolyte, and the $\kappa^{eff} = \kappa(\epsilon_2^{**})^{brug}$ is the effective bulk ionic conductivity of the electrolyte. The boundary conditions are continuity of Φ_2, and $\Phi_2(0,t) = 0$. The solid-phase Ohm's law is

$$i_1(x,t) = -\sigma^{eff} \nabla \Phi_1(x,t), \tag{4.10}$$

where i_1 is the current density in the solid, and the $\sigma^{eff} = \sigma(1 - \epsilon_2^*)^{brug}$ is the effective electronic conductivity. Also, $i_1(x,t) + i_2(x,t) = I(t)$, where $I(t)$ is the current density input to the model.

Finally, the output of the model, voltage, is written as follows:

$$V(t) = \Phi_1(l_c, t) - \Phi_1(0, t). \tag{4.11}$$

Finally, the energy balance for the lithium ion battery assuming local thermal equilibrium is given by the following equations

$$\frac{\partial(\rho c T)}{\partial t} = \nabla \,.\, (\lambda \nabla T) + q, \tag{4.12}$$

where ρ is the volume average density, c is the volume averaged specific heat, T is the temperature, and λ is the volume averaged thermal conductivity. The heat generation term, q, is given by

$$q = \sum_{i=1}^{N_*} a_i^* F j_i^*(x,t) \left(\eta_i^*(x,t) + T(t) \frac{\partial U_*}{\partial T}(c_{se,i}(x,t)) \right) - i_1 \nabla \Phi_1(x,t) - i_2 \nabla \Phi_2(x,t). \tag{4.13}$$

It is worth mentioning that this form neglects the enthalpy of mixing, since it is generally small and ignored in practice. Furthermore, the boundary conditions are defined based on the types of heat flux considered at the cell boundary such as, convection, conduction, and radiation.

4.2.1.2 Reduced order model

For deriving the reduced order model, the asymptotic analysis method has been shown to result in a more accurate approximation of the full-order model compared to similar models in the literature [55]. Furthermore, this method requires no assumptions about the spatial distributions of variables. Using the same methodology, the resulting equations of the multi-particle model with electrolyte (MPMe) are presented in the following.

The behavior of all particles in each electrode can be represented by a single representative particle, with concentration $(c_{s,i})$ given by

$$\frac{\partial c^*_{s,i}}{\partial t}(r,t) = \frac{1}{r^2}\frac{1}{\partial r}\left[D^*_i r^2 \frac{\partial c^*_{s,i}}{\partial r}(r,t)\right], \tag{4.14}$$

$$\frac{\partial c^*_{s,i}}{\partial r}(0,t) = 0, \tag{4.15}$$

$$D^*_i \frac{\partial c^*_{s,i}}{\partial r}(R^*_{p,i},t) = -j^*_i(t). \tag{4.16}$$

Furthermore, for simplification it is assumed that the solid diffusion is independent of the concentration. The current exchange density, i_0, is approximated by integration over the electrode thickness, which results in the following for the Butler-Volmer equations

$$j^*_i(t) = \frac{i^*_{0,i}(t)}{F}\left(e^{\frac{\alpha_a F}{RT}\eta^*_i} - e^{\frac{-\alpha_c F}{RT}\eta^*_i}\right), \tag{4.17}$$

$$i^n_{0,i}(t) = \frac{1}{l_n}\int_0^{l_n} k^n_0 (c_e(x,t))^{\alpha_a}(c^n_{s,max,i} - c^n_{se,i}(t))^{\alpha_a}(c^n_{se,i}(t))^{\alpha_c} dx, \tag{4.18}$$

$$i^p_{0,i}(t) = \frac{1}{l_p}\int_{l_c-l_p}^{l_c} k^p_0 (c_e(x,t))^{\alpha_a}(c^p_{s,max,i} - c^p_{se,i}(t))^{\alpha_a}(c^p_{se,i}(t))^{\alpha_c} dx. \tag{4.19}$$

Observing that the total number of lithium moles are conserved in the solid and the electrolyte. This results in a simplified form for the current density in the electrolyte [55], given by the following

$$\begin{cases} i_2(x,t) = \frac{I(t)}{l_n}x & 0 \le x < l_n, \\ i_2(x,t) = I(t) & l_n \le x \le l_n + l_s, \\ i_2(x,t) = -\frac{I(t)}{l_p}(x - l_c) & l_n + l_s < x \le l_c, \end{cases} \tag{4.20}$$

Therefor, using Equation (4.7) results in

$$I = \sum_{i=1}^{N^R_n} l_n a^n_{s,i} F j^n_i, \quad I = -\sum_{i=1}^{N^R_p} l_p a^p_{s,i} F j^p_i. \tag{4.21}$$

Because of the conservation of lithium in the electrolyte the average lithium concentration over the cell length is equal to the initial concentration. Therefore, for the electrolyte concentration, an average transference number and diffusion coefficient based on electrolyte initial concentration is considered. The resulting equation when combining with Equation (4.21) is

$$\epsilon_2^{**}\frac{\partial c_e}{\partial t}(x,t) = \nabla.(\bar{D}_e(\epsilon_2^{**})^{brugg}\nabla c_e(x,t)) + \frac{1-\bar{t}_+^0}{F} \times \begin{cases} \frac{I(t)}{l_n} & 0 \le x < l_n, \\ 0 & l_n \le x \le l_n + l_s, \\ \frac{-I(t)}{l_p} & l_n + l_s < x \le l_c, \end{cases} \tag{4.22}$$

where $\bar{t}_+^0 = t_+^0(c_e^0)$ and $\bar{D}_e = D_e(c_e^0)$ with the same boundary conditions as the ones for Equation (4.8). Similarly for solving the liquid-phase Ohm's law, Equation (4.9), the conductivity, κ, and the thermodynamic factor, $tf = (1 - t_+^0)\left(1 + \frac{d\ ln\ f_\pm}{d\ ln\ c_e}(x,t)\right)$ are calculated based on the average(initial) electrolyte concentration. Integrating and applying the boundary condition results in

$$\Delta\Phi_2(t) = -\left(\frac{l_n}{3(\epsilon^n)^{brugg}} + \frac{l_s}{(\epsilon^s)^{brugg}} + \frac{l_p}{3(\epsilon^p)^{brugg}}\right)\frac{I(t)}{\bar{\kappa}} + \frac{2RT}{Fc_{e,init}}\bar{tf}(\bar{c}_{e,p} - \bar{c}_{e,n}), \tag{4.23}$$

where $\bar{c}_{e,*}$ denotes the average electrolyte concentration over the electrode, the $\bar{\kappa} = \kappa(c_e^0)$, and $\bar{tf} = tf(c_e^0)$. The solid electrical conductivity is large in the electrodes, which means the ohmic potential drop in the solid is relatively small, and the solid electric potential is independent of x. Hence, the solid-phase potential drop is negligible, and all the particles in an electrode have the same solid-phase potential and are essentially in a parallel configuration. This results in the following $(N_n^R - 1)$ and $(N_p^R - 1)$ equality equations for negative and positive electrodes, respectively,

$$\Phi_{1,1}^* = \Phi_{1,2}^* = ... = \Phi_{1,N_*}^*. \tag{4.24}$$

Because of the above equations, the output voltage can be written for any index $i = 1, ..., N_p^R$

and $j = 1, ..., N_n^R$, therefore

$$V(t) = \eta_i^p(t) + U_p(c_{se,i}^p(t)) + V_{f,i}^p(t) - \eta_j^n(t) - U_n(c_{se,j}^n(t)) - V_{f,j}^n(t) + \Delta\Phi_2(t). \tag{4.25}$$

As for the energy balance equation, a lumped temperature model is considered, which reduces the complexity of the model. Furthermore, since the thickness of the cell is much smaller than the length scale for the heat conduction, the cell dissipates heat only through convection. With these assumptions the energy balance in reduced form is given by

$$\bar{\rho}\bar{c}\frac{dT}{dt}(t) = -\frac{hA_c(T(t) - T_a)}{V_c} + \frac{1}{V_c}\int_{V_c} q d\nu, \tag{4.26}$$

where $\bar{\rho}$ is the cell lumped density, $\bar{c}$ is the cell lumped specific heat capacity, h is the heat transfer coefficient for convection, A_c is the battery surface area, V_c is the cell volume, and T_a is the ambient temperature. Equation (4.6) is used to substitute the over potential term, η, in Equation (4.13), and further simplification of the above equation is done using the procedure in [95]. Finally, the energy balance equation reduces to

$$\begin{aligned} \rho\bar{c}l_c\frac{dT}{dt}(t) = -h(T(t) - T_a) - \sum_{*=p\&n}\sum_{i=1}^{N_*^R} a_i^* F j_i^*(t) l_* \Big(& U_*(c_{se,i}^*(t)) + V_{f,i}^*(t) \\ & -T(t)\frac{\partial U_*}{\partial T}(c_{se,i}(t))\Big) - I(t)V(t). \end{aligned} \tag{4.27}$$

4.2.2 Mechanical Model

In this section a model for the expansion of the lithium ion battery during cycling is presented. The model is developed by incorporating several simplifying assumptions. In our model, the expansion model does not affect the electrochemical model. It has been shown that for cells with a relatively small expansion such as graphite/NMC cell with 8 and 2% expansion of the anode and cathode respectively, the effect of stress induced diffusion in the solid for the voltage are negligible [50]. Additionally, an analysis of fundamental dimensionless parameters of a porous electrode model with the volume changes has shown that the dimensionless pressure parameter is orders of magnitude smaller than the other parameters [96]. Furthermore, adding the stress diffusion increases the complexity of the model substantially. Therefore, the effects of stress induced diffusion and volume changes on the terminal voltage are not considered. To further elucidate the model structure the coupling between the sub-models is shown in Figure 4.3.

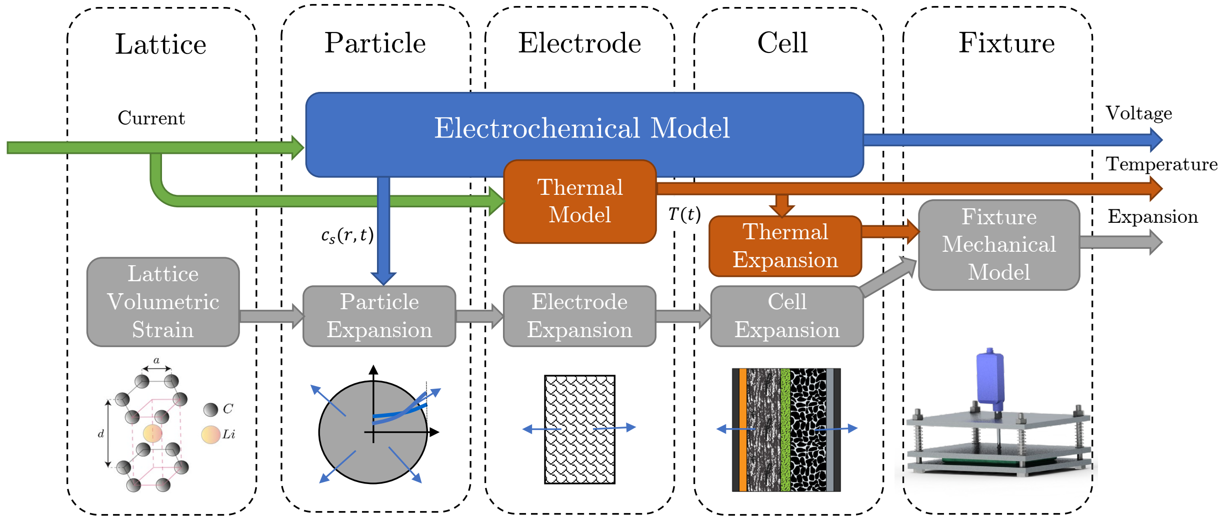

Figure 4.3: Block diagram of the MPMe with expansion. Note that the coupling between the expansion subsystems and the electrochemical subsystem is one way.

4.2.2.1 Intercalation induced expansion

With the relatively small expansion of the cell, it is appropriate to utilize the infinitesimal strain theory for modeling the deformation. Thus the Cauchy strain tensor, $\boldsymbol{\epsilon}$, is given by

$$\boldsymbol{\epsilon} = \frac{1}{2}\left(\nabla \boldsymbol{u} + (\nabla \boldsymbol{u})^T\right), \tag{4.28}$$

where $\boldsymbol{u}$ is displacement vector. The quasi-static condition is also assumed for the evolution of strain in the particle. With body forces neglected, the equilibrium condition reads as

$$\nabla \,.\, \boldsymbol{\sigma} = 0, \tag{4.29}$$

where $\boldsymbol{\sigma}$ is the Cauchy stress tensor. Furthermore, it is assumed that the bulk electrode particle is a linear elastic solid. The graphite material used in lithium-ion batteries is the mesophase carbon microbeads (MCMB), which is generally disordered, and thus it is assumed to be isotropic. The constitutive equations written using Young's modulus, E, and Poisson's ratio, ν, are given by

$$\epsilon_{ij} = \frac{1}{E}[(1+\nu)\sigma_{ij} - \nu\sigma_{kk}\delta_{ij}], \tag{4.30}$$

where the equations are expressed with respect to a Cartesian coordinate system (e.g. $i, j, k = r, \theta, \phi$), and the Einstein summation convention of summing on repeated indices is used.

During cycling the intercalation of lithium leads to changes in the lattice parameters. These changes can be represented as a volume change of some unit lattice volume, which in a macroscopic scale, is a function of the local lithium concentration. This change is represented by a volumetric strain, which is denoted by $\Delta\mathcal{V}$. Because of the assumptions of linear elasticity and small strain, this volumetric strain can be added to Equation (4.30) linearly. This is equivalent to the treatment of the stress and strain induced by thermal expansion, first presented in [97], and in agreement with other studies [50, 51, 52, 98]. Furthermore, the volumetric strain is equal in all direction, and hence it is trivial to show that the strain in the normal stresses direction is one third of the volumetric strain. Thus, the stress-strain relationship with intercalation expansion is given by

$$\epsilon_{ij} = \frac{1}{E}[(1+\nu)\sigma_{ij} - \nu\sigma_{kk}\delta_{ij}] + \frac{\Delta\mathcal{V}\left(c_s(r,t)\right)}{3}\delta_{ij}, \tag{4.31}$$

where δ_{ij} is the Kronecker delta. It is assumed that the every active material particle is sphere, so a spherical coordinate system is utilized. Furthermore, due to the symmetry $\sigma_{\theta\theta} = \sigma_{\phi\phi}$, the normal strains in Equation (4.31) can be written as

$$\epsilon_{rr} = \frac{1}{E}[\sigma_{rr} - 2\nu\sigma_{\theta\theta}] + \frac{\Delta\mathcal{V}\left(c_s(r,t)\right)}{3} \tag{4.32}$$

$$\epsilon_{\theta\theta} = \frac{1}{E}[(1-\nu)\sigma_{\theta\theta} - \nu\sigma_{rr}] + \frac{\Delta\mathcal{V}\left(c_s(r,t)\right)}{3}. \tag{4.33}$$

The spherical symmetry of the particle also results in the radial and tangential stresses which are only a function of radial position. Therefore, the stress equilibrium equation (see Equation (4.29)) in the radial direction simplifies to

$$\frac{\partial\sigma_{rr}}{\partial r} + \frac{2(\sigma_{rr} - \sigma_{\theta\theta})}{r} = 0, \tag{4.34}$$

and the strain tensor equations (see Equation (4.28)) in spherical coordinates are

$$\epsilon_{rr} = \frac{\partial u_r}{\partial r}, \tag{4.35}$$

$$\epsilon_{\theta\theta} = \frac{u_r}{r}, \tag{4.36}$$

where u_r denotes radial displacement. Based on Equations (4.32) to (4.36), a second order differential equation for the radial displacement is obtained:

$$\frac{\partial^2 u_r}{\partial r^2} + \frac{2}{r}\frac{\partial u_r}{\partial r} - \frac{2u_r}{r^2} = \frac{1+\nu}{1-\nu}\frac{\partial}{\partial r}\left(\frac{\Delta\mathcal{V}\left(c_s(r,t)\right)}{3}\right). \tag{4.37}$$

The boundary conditions are the displacement at the center being zero, and the stresses at the surface of particle being zero,

$$u_r(0,t) = 0, \tag{4.38}$$

$$\sigma_{rr}(R_p,t) = 0. \tag{4.39}$$

Integrating Equation (4.37) along the radius of the particle subject to the two boundary conditions gives the solution for u_r,

$$u(r) = \frac{1+\nu}{1-\nu}\frac{1}{3r^2}\left(\int_0^r \rho^2 \Delta\mathcal{V}(c_s(\rho,t))d\rho\right) + \frac{1-2\nu}{1-\nu}\frac{2r}{3R_p^3}\left(\int_0^{R_p} \rho^2 \Delta\mathcal{V}(c_s(\rho,t))d\rho\right). \tag{4.40}$$

Then, the radial and tangential stress are given by:

$$\sigma_{rr}(r,t) = \frac{2E}{3(1-\nu)}\left(\frac{1}{R_p^3}\int_0^{R_p} \rho^2 \Delta\mathcal{V}(c_s(\rho,t))d\rho - \frac{1}{r^3}\int_0^r \rho^2 \Delta\mathcal{V}(c_s(\rho,t))d\rho\right), \tag{4.41}$$

$$\sigma_{tt}(r,t) = \frac{E}{3(1-\nu)}\left(\frac{2}{R_p^3}\int_0^{R_p} \rho^2 \Delta\mathcal{V}(c_s(\rho,t))d\rho + \frac{1}{r^3}\int_0^r \rho^2 \Delta\mathcal{V}(c_s(\rho,t))d\rho - \Delta\mathcal{V}(c_s(r,t))\right). \tag{4.42}$$

The hydrostatic stress is equal to

$$\sigma_h(r,t) = \frac{\sigma_{rr}(r,t) + 2\sigma_{tt}(r,t)}{3}. \tag{4.43}$$

Finally, the displacement at the surface of the particle is calculated using Equation (4.40) at $r = R_p$, which is given by the following,

$$u_R(t) = \frac{1}{R_p^2}\int_0^{R_p} \rho^2 \Delta\mathcal{V}\left(c_s(\rho,t)\right) d\rho. \tag{4.44}$$

4.2.2.2 Electrode level expansion

The electrode consists of active material, binder, and conductive material. The particle expansion results in deformation of the other components. In addition, the mechanical boundary conditions also impact the expansion. The electrode is fixed at the one side to the current collector and free on the separator side. In order to simplify the modeling of electrode expansion, the volume changes in other components is assumed to be negligible. Hence, the volume change of the electrode is given by

$$\Delta V_e^* = \sum_{i=1}^{N_*^R} p_i^* \left(4\pi {R_{p,i}^*}^2\right) u_{R,i}^*, \tag{4.45}$$

where p_i is the total number of particles with a radius $R_{p,i}$ in the electrode. Furthermore, because of the large electrode length to thickness ratio and high stiffness, it is assumed that the electrode only expands in the through-plane direction [64]. Therefore, the volume change can also be written as

$$\Delta V_e^* = A\Delta t_*. \tag{4.46}$$

Following the definition of a_i^*, which is the active interfacial surface area of particles with size $R_{p,i}^*$ per unit volume of the electrode, we have:

$$a_i^* = \frac{p_i^* \left(4\pi {R_{p,i}^*}^2\right)}{Al_*}. \tag{4.47}$$

Using Equations (4.45) to (4.47) together results in the following equation for the change in electrode thickness,

$$\Delta t_* = \sum_{i=1}^{N_*^R} a_i^* u_{R,i}^* l_*. \tag{4.48}$$

4.2.2.3 Thermal and battery level expansion

Since it was assumed that the temperature is uniform in the cell, a lumped expansion model is also considered for the battery. Therefore, the thermal expansion, Δt_{th}, is given by

$$\Delta t_{th} = \alpha_{th}(T - T_a), \tag{4.49}$$

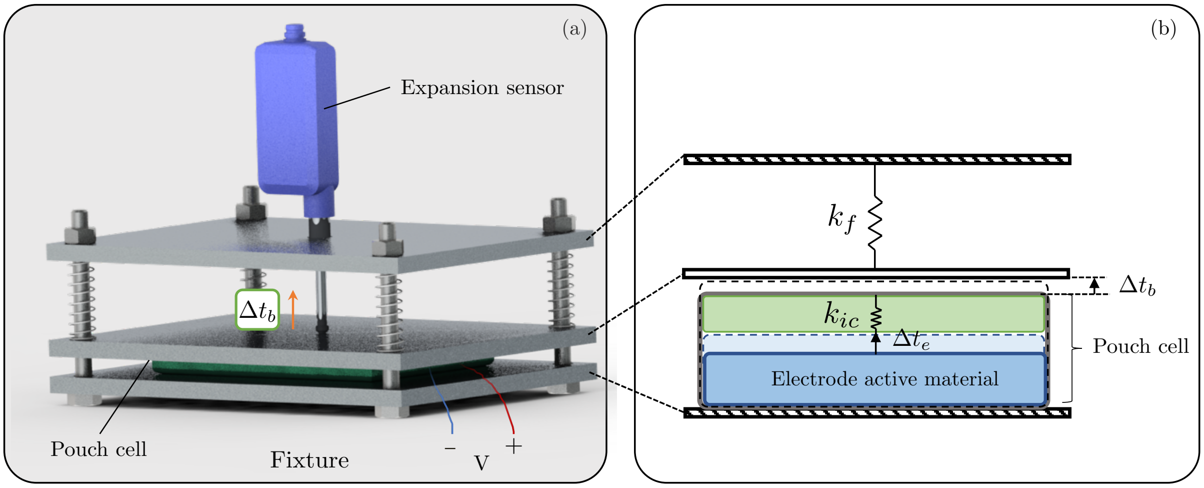

Figure 4.4: a) The fixture schematics, and b) the simplified linear spring model for the battery.

where α_{th} is the thermal expansion coefficient of the battery. The total expansion of the electrodes in the cell is simply the sum of the expansion of individual electrodes. Furthermore, in the case of this chapter, the battery consists of multiple layers of cells stacked on top of each other in a pouch cell. Hence, the total expansion of electrodes is given by

$$\Delta t_e = n_c \left(\Delta t_p + \Delta t_n \right), \tag{4.50}$$

where n_c is the number of parallel cells stacked on top of each other in the battery. However, for the expansion at the battery level it is also necessary to consider the influence of the inactive components such as the separator, current collectors, and casing. The expansion and the strain rate during battery cycling is small enough to consider a linearized regime for the deformation of these components. Furthermore, the assumption of quasi-equilibrium is considered. Therefore, the modeling of the inactive components is achieved with a linear spring in series with the electrodes. Additionally, a linear spring is also considered to account for the effects of the fixture on the expansion. The configuration of the spring model is shown in Figure 4.4(b). As the amount of force is the same in the springs, following equation can be written for the expansion at the battery level

$$\Delta t_b = \kappa_b \Delta t_e, \tag{4.51}$$

where $\kappa_b = \frac{k_{ic}}{k_{ic}+k_f}$ with k_{ic} and k_f denoting the inactive components and fixture spring constants, respectively. Finally,

$$\delta = \Delta t_b + \Delta t_{th}, \tag{4.52}$$

where δ denotes the total expansion of the battery.

4.3 Experimental Method

The pouch cell was built using the manufacturing equipment at the University of Michigan Battery Lab (UMBL). The cell was of graphite/NMC chemistry, and the specifications of the battery is shown in Table 3.1. Initial formation cycles were performed after the manufacturing to ensure the safety and performance stability of the cell. Then the cell was assembled inside the fixture shown in Figure 4.4(a). The fixture was designed such that the top and bottom plates are fixed in place while the middle plate is free moving. For pouch cells, added pressure is needed to ensure the optimal performance of the battery. Hence, the fixture was designed to apply an uniform pressure on the pouch cell. This was achieved by using compression springs and polymer poron sheets (Rogers, USA). The target applied pressure of 5 psi was achieved by adjusting the spring compression to a fixed displacement using the threaded rods. The expansion was measured using a displacement sensor (Keyence, Japan) mounted on the top plate. The dynamic testing were carried using a battery cycler (Biologic, France). The temperature was measured using a K-type thermocouple (Omega, USA) placed on the surface of the battery.

The fixture was installed inside a climate chamber with the temperature set to 25^oC, then the cell was cycled 10 times at C/3 between 3.0 V and 4.2 V to ensure the repeatability of the expansion data. The cell was charged with a constant current (CC) from the fully discharged state at different rates (C/20, C/10, C/5, C/2.5, 1C, and 2C) to 4.2 V, followed by a constant voltage (CV) period until the current dropped below C/40, followed by a rest of 3 h. Then, the cell was discharged to 3 V at the same constant current. Each cycle was repeated three times and the measurements from the final cycle were reported.

The thermal tests were done to characterize the thermal expansion and cooling behavior of the fixture. The cell was charged at C/3 to 50% SOC, followed by a rest for 3 h. Then a pulse excitation profile was applied. The profile was a charge pulse at 1C for 5 s, followed by a discharge pulse at the same rate for 5 s. The profile was repeated until the temperature reached the steady state (about 3 h), then the current profile was stopped and temperature was recorded during the cooling stage. The test was repeated with the current rate of 2C. The expansion was also monitored during these tests to be used in thermal expansion coefficient estimation.

In order to measure the potential of graphite and NMC electrodes, coin cells for individual electrodes were built. The electrode sheets were collected from the production line after going through the calendering process, and the coating on one side of the electrode was carefully removed. Then circular electrodes were extracted by using a punch. Lithium metal foil was used as the counter electrode with a glass fiber sheet as the separator. Finally, the electrolyte consisted of a 1 mol/l LiPF6 was added and coin cells (CR2032-type) were assembled.

Initial formation cycles were performed for the coin cells. The Li/NMC coin cell was cycled at constant current (C/50) between 2.8 and 4.35 V for three times. Similarly, the Li/graphite coin cell was cycled at constant current (C/50) between 0.005 and 1.0 V for three times. The measurements from the last cycle were utilized.

4.3.1 Data and code availability

The dataset and code presented in this chapter are made publicly available at [99].

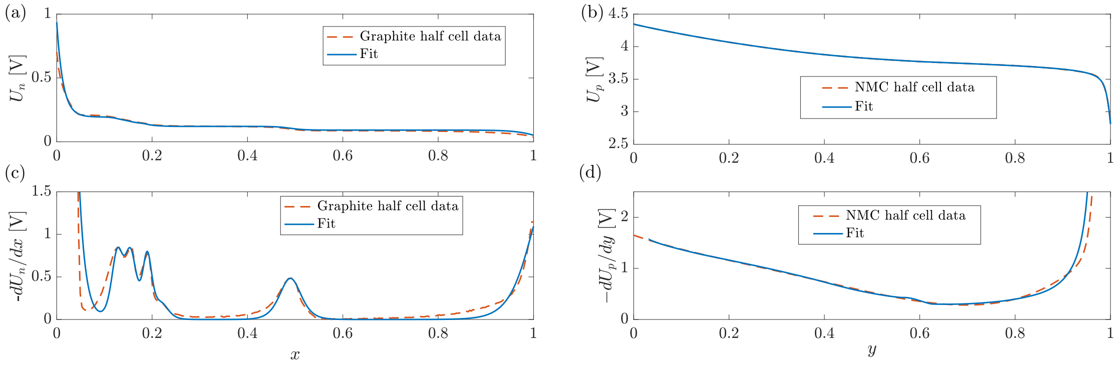

Figure 4.5: a) The graphite half-cell potential and fit. b) The NMC half-cell potential and fit. (c) The differential voltage data and fit for graphite and (d) for NMC.

4.4 Parameter Identification

4.4.1 Half-cell voltage functions

In order to develop a model for the half cell potentials, several basis function are used to capture the behavior of each electrode the best. The main goal for the graphite function is to have the phase transitions observed in the derivative of voltage. The basis functions are fitted to lithiation data for the Li/graphite coin cell and delithiation data for the Li/NMC coin cell (cell charging). The half cell functions are presented in Table 4.1. In Figure 4.5(a) and (b) the data and the fit for graphite and NMC potential are shown, respectively. The derivative of potential with respect to capacity for the data and the model are also shown in Figure 4.5(c) and (d). The data and model are in excellent agreement, especially at the phase transitions of the graphite.

4.4.2 Full cell stoichiometric window

The identification of the operating window parameters is needed for correct initialization of the concentration. The data at the lowest rate (C/20) is utilized to approximate the open circuit state of the cell. The half-cell voltage functions identified previously are used to estimate the stoichiometric operating window of each electrode, which is defined as (x_0, x_{100}) for graphite, and (y_0, y_{100}) for NMC. The estimation is done by means of a non-linear least squares with the steps detailed in [8]. The identified parameters are reported in Table 4.1 and the voltage fit is depicted in Figure 4.6(a,b) for voltage and voltage derivative. Using the identified operating windows, the relationship between initial state of charge (SoC) and concentration [100] is given by

$$c_{s,init} = c_{s,max}(\mathrm{SoC} \times (\theta_{100} - \theta_0) + \theta_0), \tag{4.53}$$

where $\theta = x, y$ depending on the electrode.

4.4.3 Half-cell expansion functions

As the lithiation increases the lattice parameters of the graphite change and the overall crystal volume increases. These changes are measured as a function of lithiation state using X-ray diffraction (XRD) method [5]. Using this data the volumetric strain of a unit lattice cell is calculated and a functional fit was found [8]. For the NMC, it has been shown that the volumetric strain is approximately linear with a maximum value of 1 - 1.5%, which agrees with crystallography measurements [101]. In order to fit the expansion of the full cell, the volumetric strain of NMC is treated as a tuning parameter using this measurement as a guideline. Here the expansion is fitted to pseud-

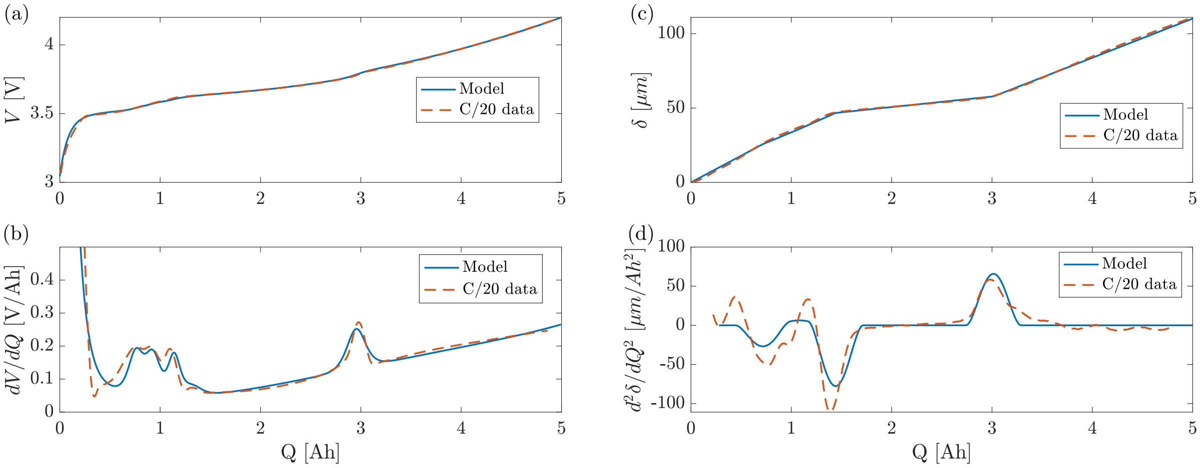

Figure 4.6: The resulting a) voltage and c) expansion fit using C/20 data to approximate the open circuit condition and identifying the operating windows of the cell. Furthermore, b) the differential voltage is showing a good fit with respect to the peak locations.

OCV (C/20) data, as a result, the temperature rise is negligible, and the contributions of thermal expansion are not considered. Following the above methodology, the fitted maximum expansion function for NMC is found to be 1.1 $\%$. The resultant expansion of the full cell using this value and graphite model is shown in Figure 4.6(c). The volumetric strain functions of graphite and NMC are also presented in Table 4.1. It should be noted that the stoichiometric window is already identified using the voltage and only the NMC volumetric strain is fitted to the data. Furthermore, from Equation (4.51), the measured expansion at the fixture level also depends on the κ_b ratio. For the fixture utilized in this work, the modulus of the springs in the fixture is much lower than the modulus of the battery, so the κ_b ratio is assumed to be equal to one.

4.4.4 Thermal properties

The thermal expansion coefficient and the heat transfer coefficient were estimated using the pulse excitation data. The density of the cell is estimated by measuring weight and the dimensions of the cell. In the Equation (4.27), the energy balance includes the entropy of reaction ($\partial U/\partial T$). In lithium insertion materials, such as graphite and NMC, the entropy of reaction is a strong function of lithiation state. For the graphite material, the entropy of reaction has been measured and presented in [102] as a function of lithiation state. In this work, a polynomial function is fitted to this data, which is presented in Table 4.1. Furthermore, the entropy of reaction data of NMC material is measured and provided in [103] as a function of open circuit potential. Similarly, a polynomial function is fitted to this data. Note that the entropy of reaction for NMC is given as a function of open circuit potential in Table 4.1. Therefore, at a lithiation state, first, the open-circuit potential is calculated using $U_p(y)$ function and then this potential is used to find the entropy of reaction, i.e. $\partial U_p/\partial T(U_p(y))$. The estimated parameters and functions are presented in Table 4.1.

4.4.5 Dynamic charge response fitting procedure

The parameters considered here for fitting the experimental data during different charge rates are the solid diffusion rate, reaction rate constant, and particle size. The fitting process consist of two iterative steps. The other model parameters are either identified using the steps described previously, or measured directly, and are reported in Table 4.1. In the first step, it is assumed that all the particle are the same size, which essentially reduces the model to the standard SPMe. Then, the solid diffusion rates and the reaction rates are fitted to the voltage and expansion charging data (C/5, C/2, 1C, 2C) at the same time. Meanwhile, the heat transfer coefficient is further tuned to fit the temperature rise data.

In the second step, a particle size distribution is considered for the graphite electrode. For the NMC electrode a single particle size configuration is considered. There are several factors that need to be considered here, which are the particle size distribution and the number of discrete particle sizes. The average particle size was found in the first step by fitting the only voltage and expansion at different rates. In this step, the goal is to fit both the voltage/expansion and their derivatives. It is assumed that the particle size follows an approximately normal distribution about the average particle size. The standard deviation of this distribution was found by finding the best-fit case in terms of the smoothing effect of the voltage derivative at high rates. Regarding the selected number of discrete particle sizes, it was observed that having five particles was a good balance between model accuracy and simplicity. Increasing the number of particle sizes produces a smoother response for the derivatives, but the model complexity and computation time greatly increased with only negligible improvements for the voltage fit. The identified particle size distribution for the graphite electrode is shown in Figure 4.7 as a fraction of the total number of particles ζ, defined as the following

$$\zeta_i^* = \frac{p_i^*}{\sum_{k=1}^{N_*^R} p_k^*}. \tag{4.54}$$

Using this fraction the active intefacial surface area, a_i^*, is given by

$$a_i^* = \frac{3\zeta_i^* \epsilon_1^*}{R_{p,i}^*}. \tag{4.55}$$

The particle sizes and their corresponding number fraction is also presented in Table 4.1.

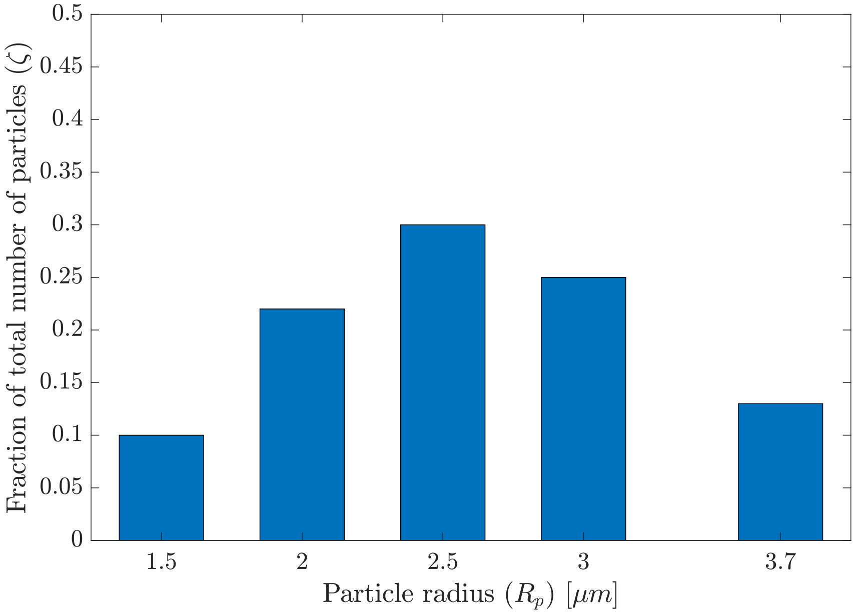

Figure 4.7: The particle size distribution for the graphite electrode.

4.5 Results and Discussion

4.5.1 Model output at different rates

In order to compare the output of the model at different rates four different charge rates, namely C/5, C/2, 1C, and 2C are selected. The starting point for all the cases are the fully discharged ($SoC = 0$) state. Using these inputs the model is simulated forward in time until the terminal voltage reaches the maximum voltage (4.2 V). The potential, expansion, and temperature rise curves are shown in Figures 4.8 to 4.10, respectively. The simulated and measured voltage curves (Figure 4.8) are in good agreement for the entire charge. The computed expansion profiles from Figure 4.9 show a good correlation to the experimental data in the maximum expansion and the region with a lower expansion rate in the middle is captured in the low charging rates.

4.5.2 Differential curves at different rates

In Figure 4.11 the first differential of the voltage and second differential of expansion is depicted for the C/5 and 1C. The model is able to capture the smoothing effect of the voltage peak at the

Electrochemical					
Parameter	Symbol	Unit	Negative electrode	Separator	Positive electrode
Thickness	t_0	μm	62^m	12^m	67^m
Particle radius, total number fraction	$[R_{p,1},\ \zeta_1]$	$[\mu m,\ -]$	$[1.5,\ 0.10]^f$		$[3.5,\ 1]^f$
Particle radius, total number fraction	$[R_{p,2},\ \zeta_2]$	$[\mu m,\ -]$	$[2.0,\ 0.22]^f$		-
Particle radius, total number fraction	$[R_{p,3},\ \zeta_3]$	$[\mu m,\ -]$	$[2.5,\ 0.30]^f$		-
Particle radius, total number fraction	$[R_{p,4},\ \zeta_4]$	$[\mu m,\ -]$	$[3.0,\ 0.25]^f$		-
Particle radius, total number fraction	$[R_{p,5},\ \zeta_5]$	$[\mu m,\ -]$	$[3.7,\ 0.13]^f$		-
Active material ratio	ϵ_1	-	0.610^f		0.445^f
Reaction rate constant	k_0	$\frac{mol}{m^2 s\left(\frac{mol}{m^3}\right)^{1.5}}$	$1.1\text{e}{-11}^f$		$5.0\text{e}{-11}^f$
Charge transfer coefficient	$\alpha_c = \alpha_a$	-	0.5^a		0.5^a
Solid diffusion rate	D_s	$\frac{m}{s^2}$	$5.0\text{e}{-15}^f$		$8.0\text{e}{-15}^f$
Film resistance	ASR_f	$\Omega.m^2$	1.0e−3[104]		0^a
Volume fraction in electrolyte	ϵ_2	-	0.3^a	0.4^m	0.3^a
Maximum lithium concentration	$c_{s,max}$	$\frac{mol}{m^3}$	28746^a		35380^a
				Electrolyte	
Initial electrolyte concentration	c_e^0	$\frac{mol}{m^3}$		1000^a	
Thermodynamic factor	$\bar{tf}$	-		1.34[105]	
Transference number	$\bar{t}_+^0$	-		0.38[105]	
Electrolyte conductivity	$\bar{\kappa}$	$\frac{S}{m}$		1.3[106]	
Electrolyte Diffusion Coefficient	$\bar{D}_e$	$\frac{m}{s^2}$		5.2e−10[106]	
Bruggman exponent	$brugg$	-		1.5^a	
Thermal and cell properties				Value	
Total electrode area	A	m^2		0.2050^m	
Cell lumped density	$\bar{\rho}$	$\frac{kg}{m^3}$		3100^m	
Cell lumped specific heat capacity	$\bar{c}$	$\frac{J}{kg.K}$		1100^f	
Air convective coefficient	h	$\frac{W}{m^2.K}$		5^f	
Cell thermal expansion coefficient	α_{th}	$\frac{\mu m}{K}$		1.48^f	
Stoich. window for the neg. electrode	$[x_0, x_{100}]$	-		$[0.002, 0.8332]^f$	
Stoich. window for the pos. electrode	$[y_0, y_{100}]$	-		$[0.890, 0.033]^f$	
Fitted functions					Data source
$U_n(x)[V] = 0.063 + 0.8exp(-75(x+0.001)) - 0.0120tanh\left(\frac{x-0.127}{0.016}\right) - 0.0118tanh\left(\frac{x-0.155}{0.016}\right) - 0.0035tanh\left(\frac{x-0.220}{0.020}\right) - 0.0095tanh\left(\frac{x-0.190}{0.013}\right) - 0.0145tanh\left(\frac{x-0.490}{0.020}\right) - 0.0800tanh\left(\frac{x-1.030}{0.055}\right)$					This work
$U_p(y)[V] = 4.3452 - 1.6518y + 1.6225y^2 - 2.0843y^3 + 3.5146y^4 - 2.2166y^5 - 0.5623\text{e}{-4}exp(109.451y - 100.006)$					This work
$\Delta\mathcal{V}_n(x)[-] = (x < 0.12)(0.2x) + (0.12 \leq x < 0.18)(0.16x + 5\text{e}{-3}) + (0.18 \leq x < 0.24)(0.17x + 3\text{e}{-3}) + (0.24 \leq x < 0.50)(0.05x + 0.03) + (0.50 \leq x)(0.15x - 0.02)$					This work, [5]
$\Delta\mathcal{V}_p(y)[-] = -1.1\text{e}{-2}(1-y);$					This work, [101]
$\frac{\partial U_n}{\partial T}(x)[\frac{mV}{K}] = 0.28 - 1.56x - 8.92x^2 + 57.21x^3 - 110.7x^4 + 90.71x^5 - 27.14x^6$					[102]
$\frac{\partial U_p}{\partial T}(V)^1[\frac{mV}{K}] = -800 + 779V - 284V^2 + 46V^3 - 2.8V^4$					[103]

Table 4.1: List of model parameters and functions (25^oC), m: measured, f: fitted to the experimental data, a: assumed. ^{1}written as a function of the open-circuit potential U_p.

1C qualitatively well while maintaining the peaks for the expansion differential. It should be noted that as the C-rate increases the model prediction accuracy suffers slightly. This is evident from the increased RMSE at the higher C-rates shown in Figures 4.8 and 4.9, which stems from the

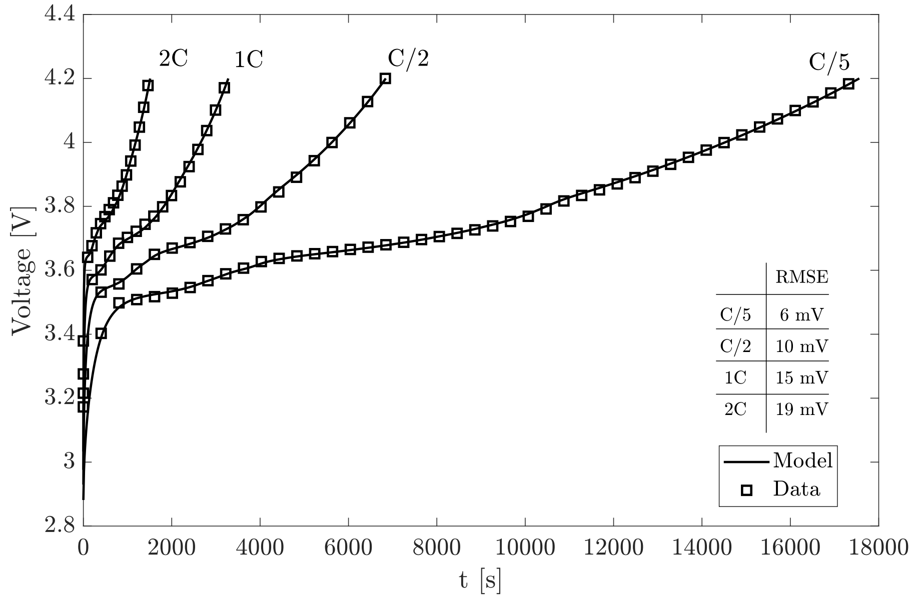

Figure 4.8: The results of the MPMe model and data for the voltage at different charging rates. Furthermore, the root mean square of the error (RMSE) is embedded in the table for the different C-rates.

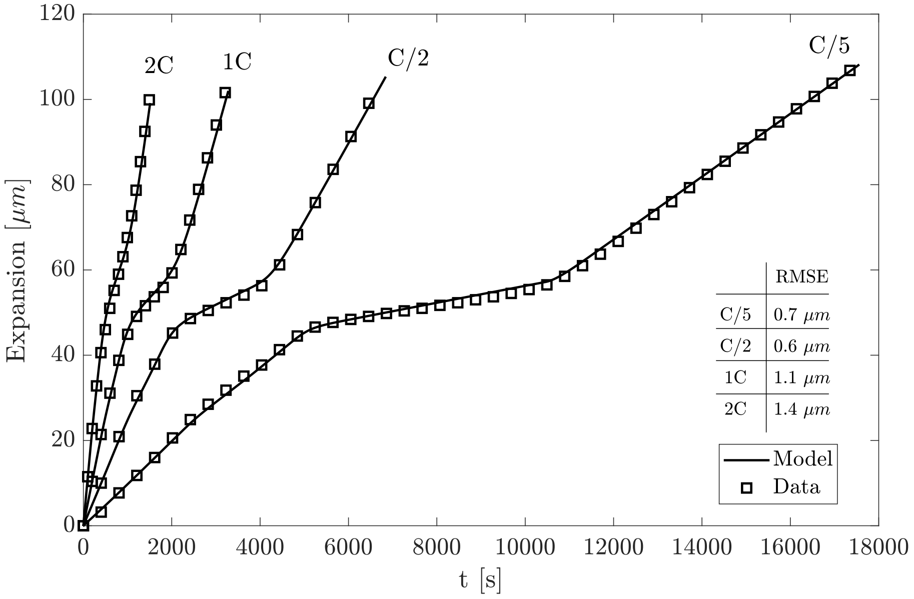

Figure 4.9: The results of the MPMe model and data for the expansion at different charging rates. Furthermore, the root mean square of the error (RMSE) is embedded in the table for the different C-rates. Note that the model is able to capture the maximum expansion and the middle section with the lower expansion rate.

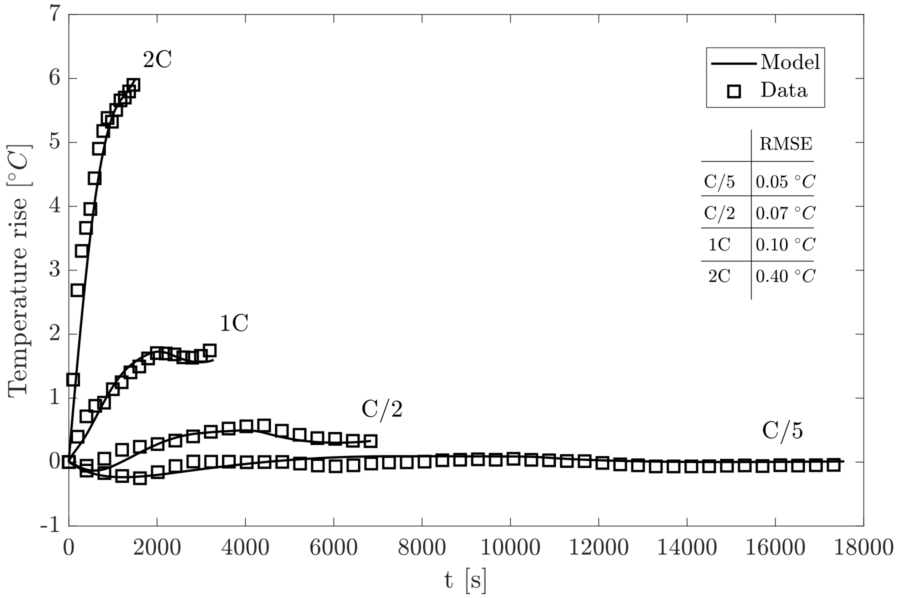

	RMSE
C/5	0.05 $°C$
C/2	0.07 $°C$
1C	0.10 $°C$
2C	0.40 $°C$

Figure 4.10: The results of the MPMe model and data for the temperature rise at different charging rates. Furthermore, the root mean square of the error (RMSE) is embedded in the table for the different C-rates. Note that the model is able to capture the non-monotonic temperature rises of C/2 and 1C, which is made possible by inclusion of the entropy of reaction terms.

omission of the higher order dynamics in our reduced order model. This essentially limits the model applicability to the rates below 2C. Nevertheless, electric vehicles rarely able to charge at rates above 2C due to the limitations of the current charging infrastructure. Furthermore, with a higher order model comes the cost of an increased computation and parameterization complexity. Therefore, in practice a reduced model that can achieve an acceptable prediction accuracy and can facilitate the development of algorithms for estimating degradation mechanisms is preferable.

4.5.3 Particle size distribution and peak smoothing

In order to elucidate the connection between the particle size distribution and peak smoothing, in Figure 4.12, the surface lithiation state of the particles during charge at low (C/5) and high (1C) rates are depicted. As can be seen, there are three regions in that lithiation states diverge, which correspond to the three plateaus in the graphite voltage. At the low C-rate, because the charge time is long enough for the slow diffusion process in the solid, the particles converge as they transition between the plateaus. However, at the high C-rate, because of limits in the diffusion process, the particles surface concentration remain separated, where the smaller particles charge faster at the second plateau. The increase divergence between the particle surface concentrations results in a smooth transition between the voltage plateaus, which is observed as peak smoothing in the voltage derivative data.

As mentioned in the previous sections, the peak in the differential expansion stay observable at the high C-rate, which is also captured using the model. The prevailing reason for this behavior is that the expansion is approximately a function of the average concentration of lithium in the particle (see Equation (4.44)), whereas, the voltage is driven by the surface concentration (see Equation (4.6)). Slow solid diffusion rate increases the concentration at the surface, whereas the average concentration is unchanged at the same SoC at higher C-rates as shown in Figure 4.12(c). Moreover, the reduced order MPMe indicates that the total expansion is the summation of the individual particle expansions, in other words, the particle are in series in terms of expansion. As a result, the expansion is less sensitive to the non-uniformity of the lithiation and the peak of the differential expansion stays observable at the high C-rate. This means that the differential expansion provides useful information about the average lithiation state of the graphite at high C-rates that can be utilized in diagnostic methods.

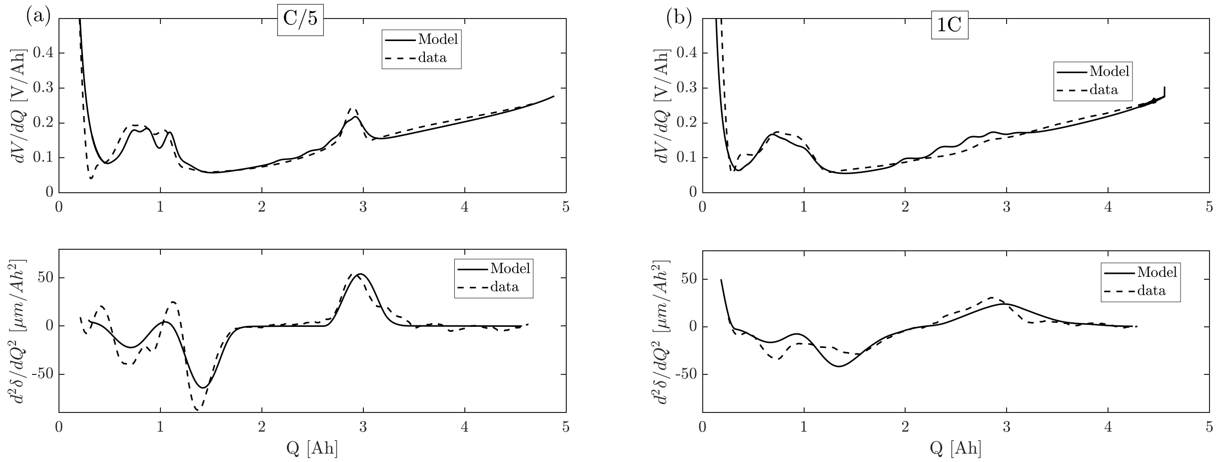

Figure 4.11: The results of the differential voltage and expansion of the model with the data at (a) C/5 rate, and (b) 1C rate.

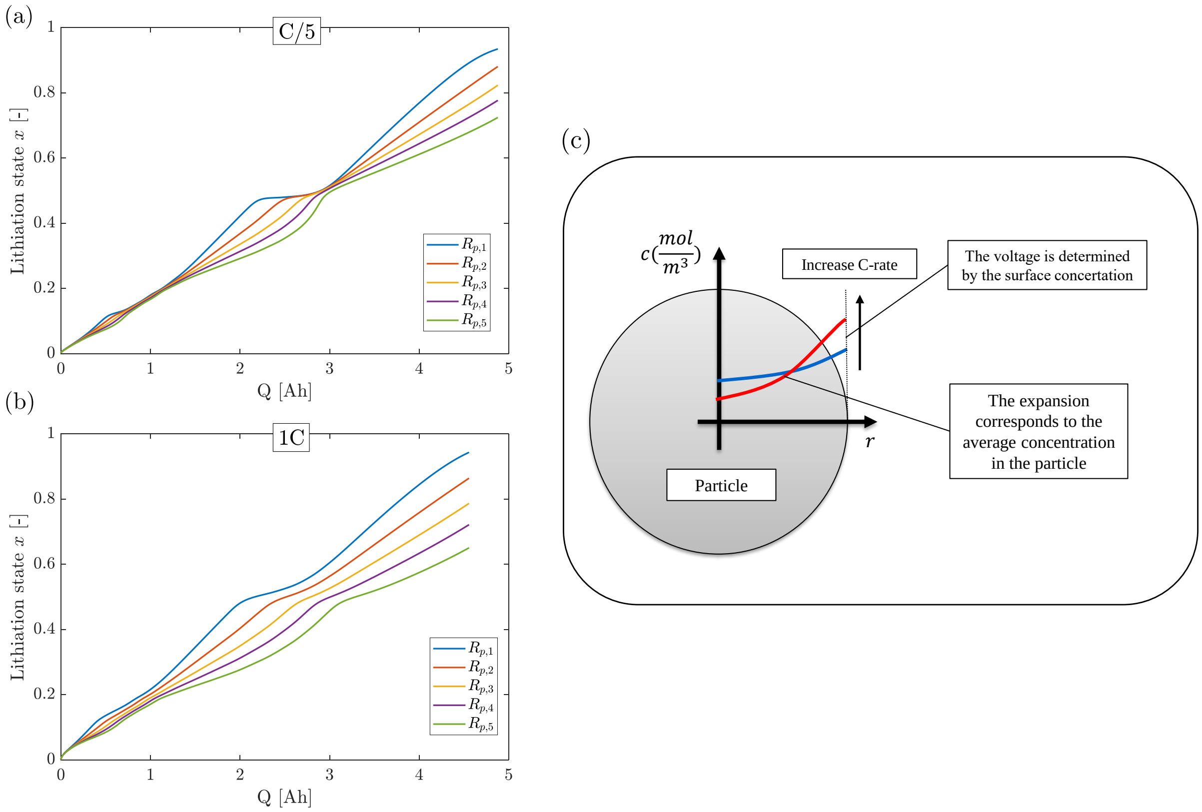

Figure 4.12: (a) The surface lithiation state of the graphite particles at C/5, and (b) 1C. Note that the states diverge more at the higher C-rate compared to the low C-rate. Also, notice that the three regions where states are diverging correspond to the plateaus in the graphite potential. (c) Schematics of the concentration profile inside of a particle with respect to the C-rate.

4.5.4 Comparison of the reduced order models

In this section, the output of the MPMe and SPMe models are compared. In this case, all the parameters are the same between the two models, except the MPMe uses the particles with the size distribution shown in the previous section. The differential voltage and expansion outputs for the MPMe developed and the standard SPMe are shown in Figure 4.13 for two different C-rates of C/5 and 1C. It is noted that, as expected, the SPMe model is not able to capture the smoothing effect observed in the data. However, the reduced order multi-particle model is able to capture this behavior.

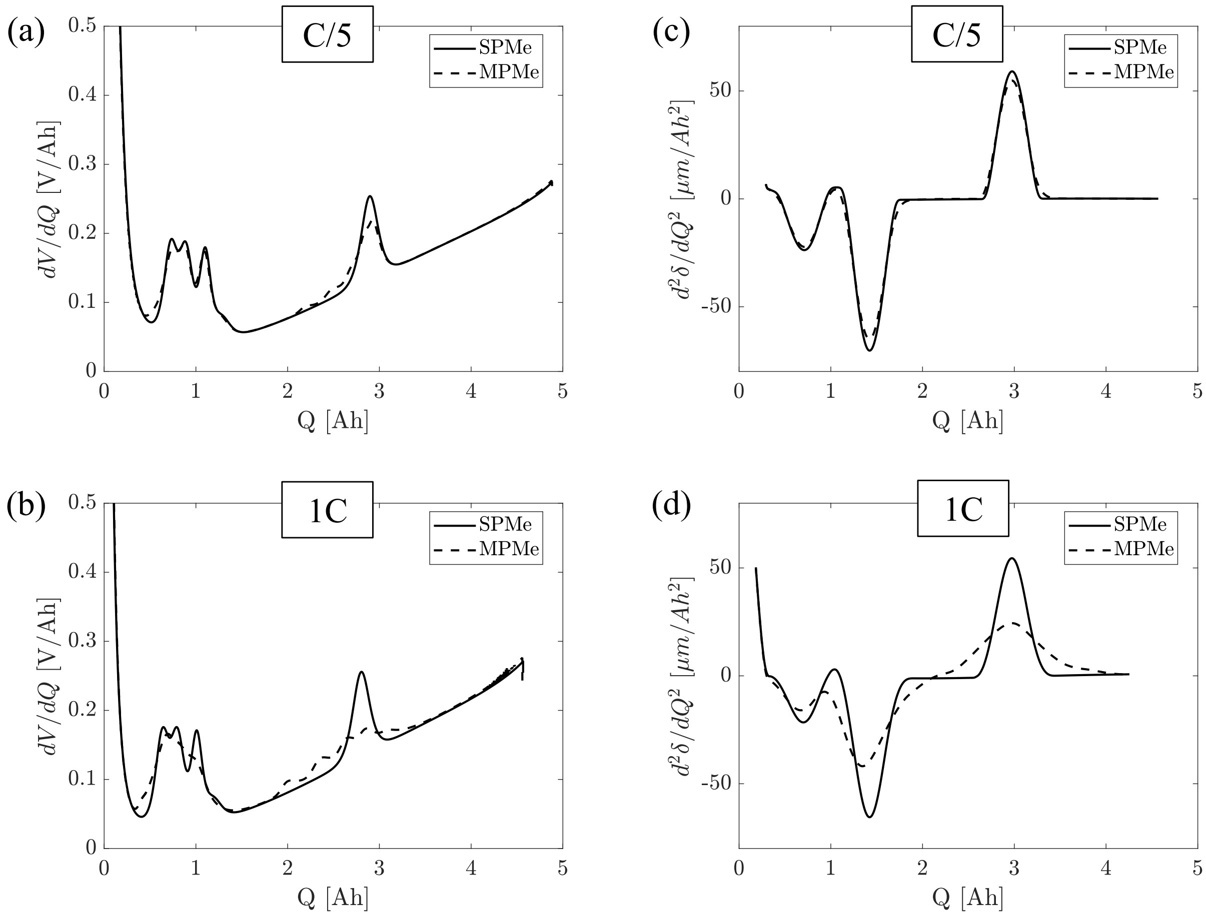

Figure 4.13: The comparison of the response of the SPMe (reduced order with a single particle size), and MPMe (reduced order with a particle size distribution) at (a) differential voltage at C/5 rate, and (b) 1C rate. (c) differential expansion at C/5 rate, and (d) 1C rate. Note that the SPMe is not able to model the peak smoothing.

4.5.5 Model calibration during aging using updated eSOH parameters

To examine the model response at different stages of aging, the model parameters corresponding to the eSOH parameters are updated using the eSOH estimation method presented in the Chapter 2. The measurements of voltage and expansion at C/20 are used for the eSOH estimation. The eSOH parameters of the electrode utilization window, ($x_{100},\ y_{100}$), are directly present in the physics-based model as well and are updated accordingly. The eSOH parameters parameters of the electrode capacity, ($C_n,\ C_p$), are connected to the active material volume ratio, ϵ_1, therefore, the active material ratio is updated using the following equation:

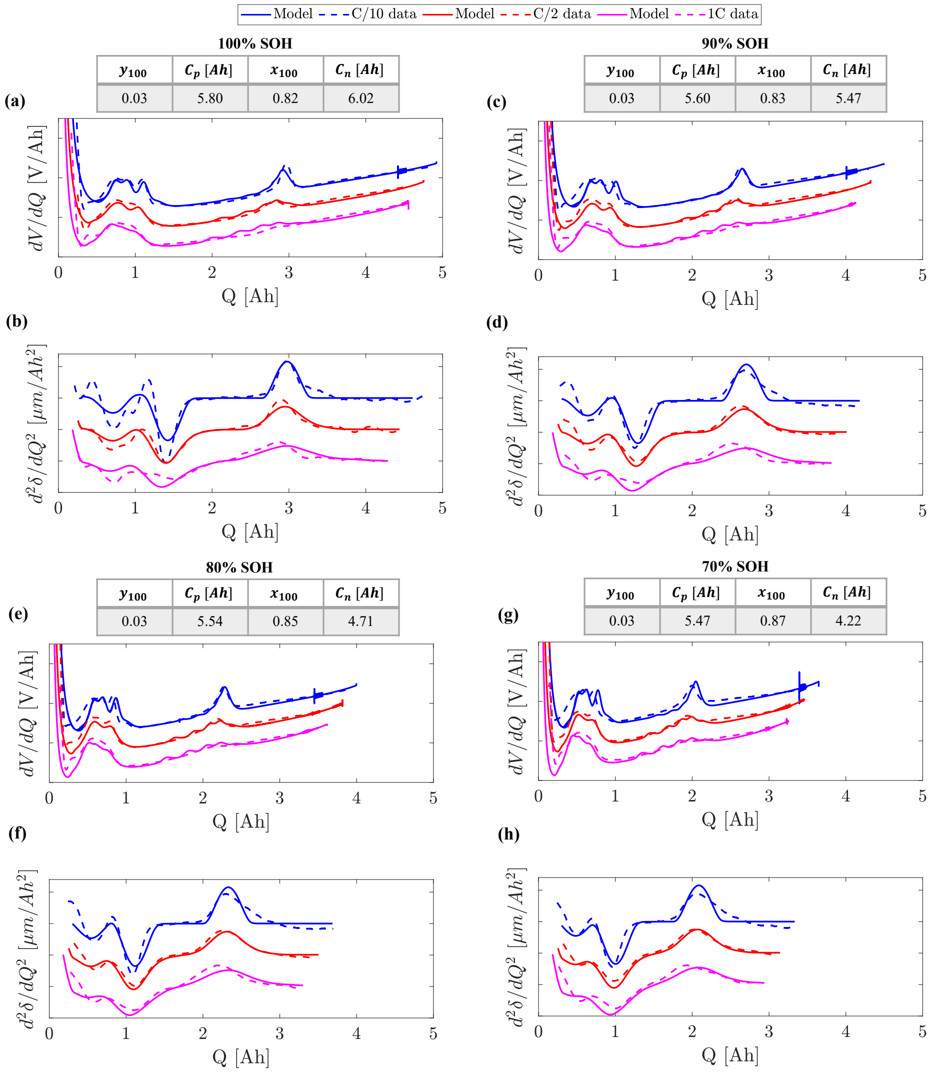

100% SOH

y_{100}	C_p [Ah]	x_{100}	C_n [Ah]
0.03	5.80	0.82	6.02

90% SOH

y_{100}	C_p [Ah]	x_{100}	C_n [Ah]
0.03	5.60	0.83	5.47

80% SOH

y_{100}	C_p [Ah]	x_{100}	C_n [Ah]
0.03	5.54	0.85	4.71

70% SOH

y_{100}	C_p [Ah]	x_{100}	C_n [Ah]
0.03	5.47	0.87	4.22

Figure 4.14: (For clarity of the presentation the model/data responses are vertically shifted in all the subplots at the different C-rates) The comparison of the output of the physics-based model and data. The electrode parameters in the physics-based model are recalibrate using the identified eSOH parameters. The differential voltage and second differential of the expansion measured at @$25°C$ for C/10, C/2, and 1C. The modeling is done for the fresh cell, and three aged states of 90%, 80%, and 70% capacity retention.

$$\epsilon^a_{1,*} = \epsilon^f_{1,*}\frac{C^a_*}{C^f_*}. \tag{4.56}$$

The simulation is done at the fresh state and three different stages of capacity retention of 90%, 80%, and 70%. The aging data used here is from the cell aged at 2C @$45°C$ condition (see Section 3.2). Furthermore, at each stage, the simulation is done with three different C-rates of C/10, C/2, and 1C. The results of the simulation and data are presented in Figure 4.14 for the differential signals and in Figure 4.15 for the voltage and expansion outputs. Furthermore, the eSOH parameters at each stage of aging are also presented. As can be seen, with the eSOH calibration, the model is able to match the data to an acceptable degree, while capturing the smoothing effect of the differential signals at the aged states as well.

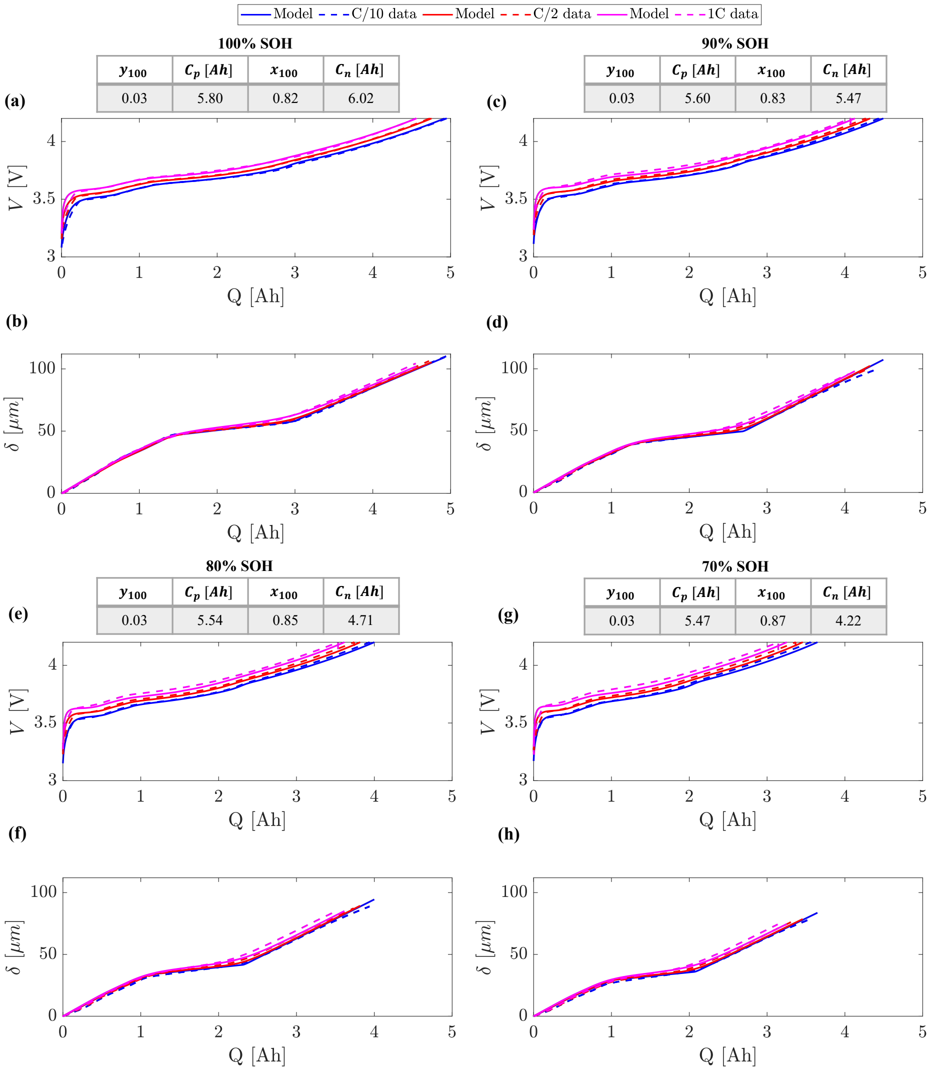

100% SOH

y_{100}	C_p $[Ah]$	x_{100}	C_n $[Ah]$
0.03	5.80	0.82	6.02

90% SOH

y_{100}	C_p $[Ah]$	x_{100}	C_n $[Ah]$
0.03	5.60	0.83	5.47

80% SOH

y_{100}	C_p $[Ah]$	x_{100}	C_n $[Ah]$
0.03	5.54	0.85	4.71

70% SOH

y_{100}	C_p $[Ah]$	x_{100}	C_n $[Ah]$
0.03	5.47	0.87	4.22

Figure 4.15: The comparison of the output of the physics-based model and data. The electrode parameters in the physics-based model are recalibrate using the identified eSOH parameters during diagnostics test. The voltage and second the expansion at @$25°C$ for C/10, C/2, and 1C.

The only parameters calibrated for capturing the aged cell responses were the eSOH parameters. There are a number of parameters that can also change as the cell ages. For example, the calibration of parameters related to the resistance increase was not considered in this work. The growth of the SEI layer is responsible for the resistance increase, and it can be modeled by increasing the film resistance and reducing the electrode porosity. As can be seen in Figure 4.15 the voltage data is slightly higher than the model prediction at the aged states. This mismatch between the model and the data is contributed to the lack of resistance calibration in this work. However, it should be noted that the resistance increase has a minimal impact on the differential signals and, as can be seen in Figure 4.14 the data and model, are in excellent agreement even at the most aged state. The reason for this behavior is that any resistance increase under constant current charging, in effect, results in an almost constant over-potential increase that is canceled out by differentiation.

4.6 Summary

In this chapter, we have demonstrated that unlike differential voltage, the peaks in the differential expansion curve are observable up to 1C rate and this makes the differential expansion an excellent method for capacity estimation during fast charging scenarios (above C/2). To understand why that is the case, a reduce order model with particle size distribution and mechanical expansion was developed. The model consists of a physico-chemical model for the porous electrode and separator domain that is thermally coupled to a lumped energy balance model. The experimental and simulated expansion curves for constant current charge rates at C/5, C/2, 1C and 2C were in good agreement. Furthermore, both experimental and simulated data showed peak smoothing of the cell's differential expansion as the charge rates increases.

CHAPTER 5

A Fast Charging Algorithm Cognizant of Mechanical Stress and Lithium Plating

5.1 Introduction

This chapter aims to leverage the existing CC-CV protocol and augment it with additional constraints that are cognizant of the degradation mechanisms. The new charging algorithm, derived in Section 5.2, can be used with any model to impose constraints on aging variables. The new constraints are added linearly to the integral current controller, which also includes a saturation limit and anti-windup scheme. In Section 5.3, the electro-chemical-mechanical model developed in Chapter 4 is utilized to demonstrate the new charging algorithm by imposing constraints on plating potential, η_{pl}, the mechanical stress, σ, and the temperature, T. Thus, the new algorithm is named CC-CV$\eta\sigma$T (VEST), accordingly. Since the new algorithm relies on latent variables in a model, a state observer is also required. Figure 5.1 shows an example of such configuration, and the results are presented in Section 5.4. Furthermore, due to the aging number of parameters may need re-calibration from time to time. Previously, we have developed an observer in [7], and an electrode state of health (eSOH) estimation method in [8] utilizing the cell voltage and expansion that can be used in conjunction with the CC-CV$\eta\sigma$T charging as shown in Figure 5.1. Nevertheless, the focus of this work is to showcase the CC-CV$\eta\sigma$T charging algorithm.

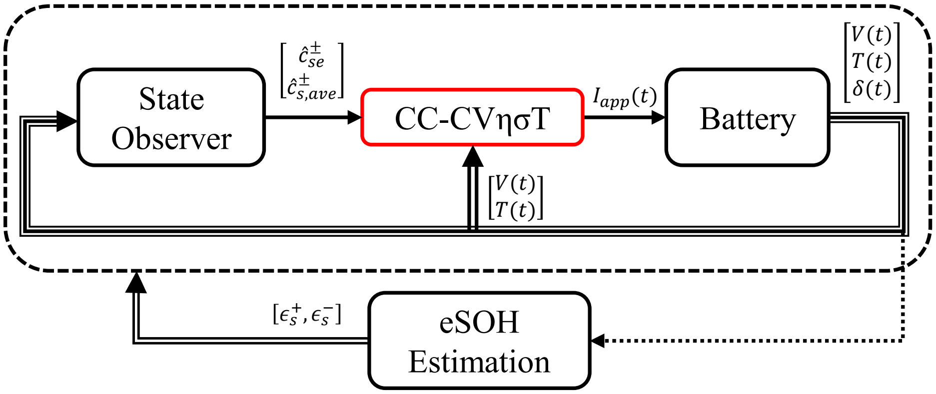

Figure 5.1: The proposed configuration for the CC-CV$\eta\sigma$T charging algorithm. The state observer and eSOH estimation methods are presented in earlier works ([7, 8]).

5.2 Fast Charging Algorithm

The proposed fast charging algorithm is presented in this section. The new algorithm is based on the constant current constant voltage (CC-CV) charging scheme. The CC-CV charging can be implemented in a number of ways. For example, a switch may be used to change from the CC phase to the CV phase once the voltage limit is reached. In this case, a reset might be needed for the integrator current controller once the switch happens. Another method for implementing the CC-CV charging is to use an integrator controller with output saturation and anti-windup:

$$\frac{dI}{dt} = -\left[K_{I,V}(V_d - V_t) + K_{aw}(I - \max(I_{max}, I))\right], \tag{5.1}$$

where $I < 0$ is charging, V_d is the desired or maximum allowable voltage, I_{max} is the maximum allowable current, and $K_{I,V}$ and K_{aw} are the gains for the voltage error and anti-windup, respectively. The setpoint or the initial condition is $I(0) = I_{max}$. The applied or output current is given by

$$I_{app} = \max(I, I_{max}). \tag{5.2}$$

The above implementation of the CC-CV charging will be used to construct the new charging algorithm with aging-aware constraints. Additional variables considered for the new charging algorithm are the plating potential, η_{pl}, the mechanical stress, σ, and the temperature T. The definitions of the plating potential and mechanical stress are given in Section 5.3. The temperature is assumed to be directly measurable from the surface of the lithium-ion battery. However, it is also possible to incorporate a thermal model of the battery and utilize the estimated temperature inside or at the battery center. The additional constraints are as follows:

$$\eta_{pl} > \eta_{pl,d}, \tag{5.3a}$$

$$\sigma < \sigma_d, \tag{5.3b}$$

$$T < T_d, \tag{5.3c}$$

where $\eta_{pl,d}$ is the desired minimum potential to reduce the lithium plating, σ_d is the desired maximum stress to reduce the material fracture and failure, and T_d is the desired maximum temperature to reduce aging due to the SEI growth. The charging protocol in Equation (5.1) is modified by adding the error between the variable and the desired value in Equation (5.3). The new charging algorithm, CC-CV$\eta\sigma$T, is as follows:

$$\begin{aligned}\frac{dI}{dt} = -\,[&K_{I,V}(V_d - V_t) + \\ &(V_d > V_t)(\eta_{pl} < \eta_{pl,d})K_{I,\eta}(\eta_{pl} - \eta_{pl,d}) + \\ &(V_d > V_t)(\sigma_d < \sigma)[K_{I,\sigma}(\sigma_d - \sigma) + K_{P,\sigma}\dot{\sigma}] + \\ &(V_d > V_t)(T_d < T)[K_{I,T}(T_d - T) + K_{P,T}\dot{T}] + \\ &K_{aw}(I - \max(I_{max}, I))],\end{aligned} \tag{5.4}$$

where $K_{I,\eta}$, $K_{I,\sigma}$, and $K_{I,T}$ are the respective integral gains for the plating potential, mechanical stress, and temperature. The $K_{P,\sigma}$ and $K_{P,T}$ are the proportional gains that are added to mitigate the output oscillations. Note that conditional terms are also considered for the additional variables so that they are only active if the voltage is below the maximum voltage. This ensures that overvoltage condition is avoided. Finally, the output current is given by Equation (5.2), similarly to the CC-CV charging.

5.3 The Aging Related Variables

To demonstrate the new charging algorithm an electro-chemical-mechanical model developed in Chapter 4 is utilized. In this section, the lithium plating potential and the mechanical stress are defined, and their connection to aging is discussed.

5.3.1 Li Plating Model

The Li plating potential is defined as the following:

$$\eta_{pl} = \phi_s - \phi_e - V_f, \tag{5.5}$$

where ϕ_s denotes the solid potential and ϕ_e denotes the electrolyte potential. Here V_f is the voltage drop across the SEI film.

A simple model of the plating reaction current ([107]) is given by

$$j_{pl} = -\frac{i_{0,pl}}{F} \exp\left(\frac{-\alpha_{c,pl} F}{RT} \eta_{pl} \right), \tag{5.6}$$

where $i_{0,pl}$ is the exchange current density of Li deposition, and $\alpha_{c,pl}$ has a value of 0.5. An important outcome of Equation (5.6) is that to limit the amount of lithium plating the lithium plating potential, η_{pl}, needs to stay above zero. Therefore, the constraint for lithium plating can be written as

$$\eta_{pl} > 0 \text{ V}. \tag{5.7}$$

5.3.2 Stress Model

During cycling, the intercalation of lithium leads to changes in the lattice parameters. These changes lead to a volume change of a unit lattice volume, which is a function of the local lithium concentration on a macroscopic scale. The volume change is represented by a volumetric strain, which is denoted by $\Delta\mathcal{V}$. The detailed derivation of the expansion and stress is also presented in the Appendix. The hydrostatic stress σ_h (see Equation (4.43)) is given by:

$$\sigma_h(r,t) = \frac{2E}{3(1-\nu)}\left(\frac{1}{R_p^3}\int_0^{R_p} \rho^2 \Delta\mathcal{V}(c_s(\rho,t))d\rho - \frac{\Delta\mathcal{V}(c_s(r,t))}{3}\right). \tag{5.8}$$

The stress distribution across the particle radius is not uniform, making the process of defining a single constraint more complex. Furthermore, mechanical failure and fracture happens with repeated cycling and more often at the particle's surface. The stress at the surface goes from compressive during lithiation to tensile during delithiation. Therefore, to limit the mechanical degradation, a constraint should be considered for the stress both during charging and discharging. Nevertheless, we have only considered a constraint on the absolute value of the stress at the surface during charging:

$$|\sigma_h(R_p,t)| < \sigma_{d,m}, \tag{5.9}$$

where $\sigma_{d,m}$ is the maximum allowable stress that can be defined by the user to limit the aging.

5.4 Results and Discussion

In this section, the ability of the CC-CV$\eta\sigma$T algorithm to limit the aging-related variables is exhibited by utilizing the physics-based model in the appendix Chapter 4 with the aging-related parameters presented in the previous section. The constraints selected for the CC-CV$\eta\sigma$T are as follows:

$$\eta_{pl} > 0 \text{ V}, \tag{5.10a}$$

$$|\sigma_h(R_p, t)| < 92 \text{ MPa}, \tag{5.10b}$$

$$T < 40\,^{o}\text{C}. \tag{5.10c}$$

The maximum voltage is set to 4.2 V, and the maximum current is 8 C (40 A). The simulation is also done once using the CC-CV charging method to compare the results of the CC-CV$\eta\sigma$T. Finally, the approaches to include safety margins for the constraints are discussed by analyzing the lithium plating potential's sensitivity to the active material ratio since the reduction of active material of the graphite electrode during aging can significantly affect the plating potential.

5.4.1 Gain Selection

Determining the gains in Equation (5.4) requires careful consideration of the different operating points and the constraints. The desired response should have minimal oscillation and overshoot. However, since the lithium-ion battery is a highly non-linear system, guaranteeing the desired response with one set of gains is not feasible. Therefore, it is necessary to test the response at the different operating points and re-tune, if needed, in parameter drift or change during aging. Nevertheless, the gains shown in Table 5.1 are found to be highly effective under a wide range of operating points and are used in all the simulations unless specified otherwise.

Figure 5.2 demonstrates the effects of the proportional controller and a possible tuning procedure. Two different scenarios are considered. In the first scenario depicted in Figure 5.2 (a), (b),

Gain	$K_{I,V}$	$K_{I,\eta}$	$K_{I,\sigma}$	$K_{P,\sigma}$	$K_{I,T}$	$K_{P,T}$	K_{aw}
Value	50	$5e4$	200	1	50	500	10
Unit	$\frac{\text{A}}{\text{V.s}}$	$\frac{\text{A}}{\text{V.s}}$	$\frac{\text{A}}{\text{MPa.s}}$	$\frac{\text{A}}{\text{MPa}}$	$\frac{\text{A}}{\text{K.s}}$	$\frac{\text{A}}{\text{K}}$	$\frac{1}{\text{s}}$

Table 5.1: Selected Gains

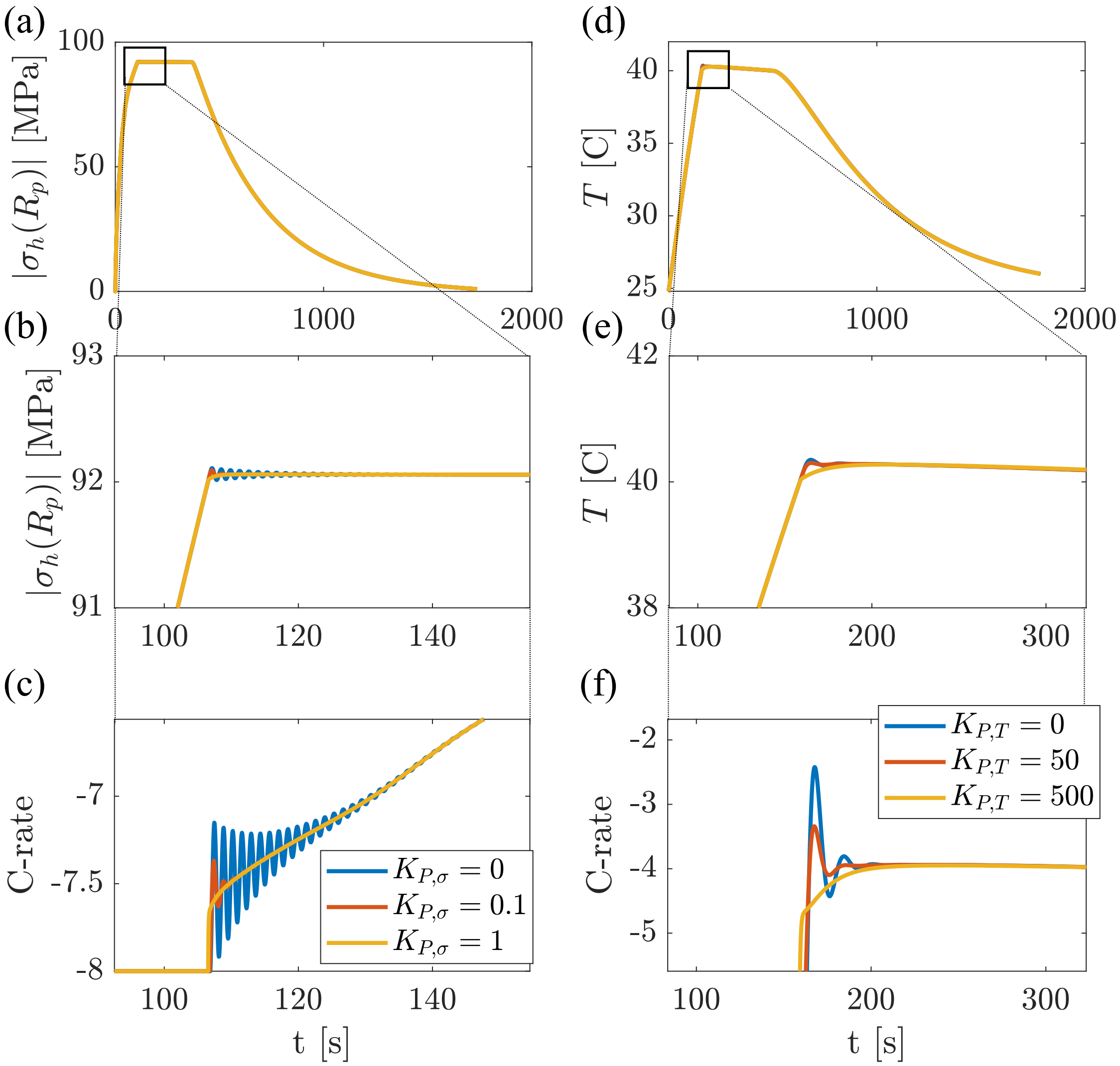

Figure 5.2: a) The mechanical stress, b) the part of the response enlarged for clarity, and c) the controller input signal, simulated with three different proportional gains. In this scenario only mechanical stress and voltage constraints are incorporated. d) The temperature response, e) the enlarged depiction of the highlighted area, and f) the input current with three different proportional gains. In this scenario only temperature and voltage constraints are active. Note that the oscillations are reduced with the proportional controller.

and (c) only the mechanical stress and voltage constraints are incorporated. The portion of the response highlighted in Figure 5.2 (a) is shown in Figure 5.2 (b) and the corresponding input current is shown in Figure 5.2 (c). The simulation was performed with values of $K_{P,\sigma} = [0, 0.1, 1]$. The importance of including the proportional gain is shown, as the oscillations are entirely reduced by selecting an appropriate value for the $K_{P,\sigma}$ gain.

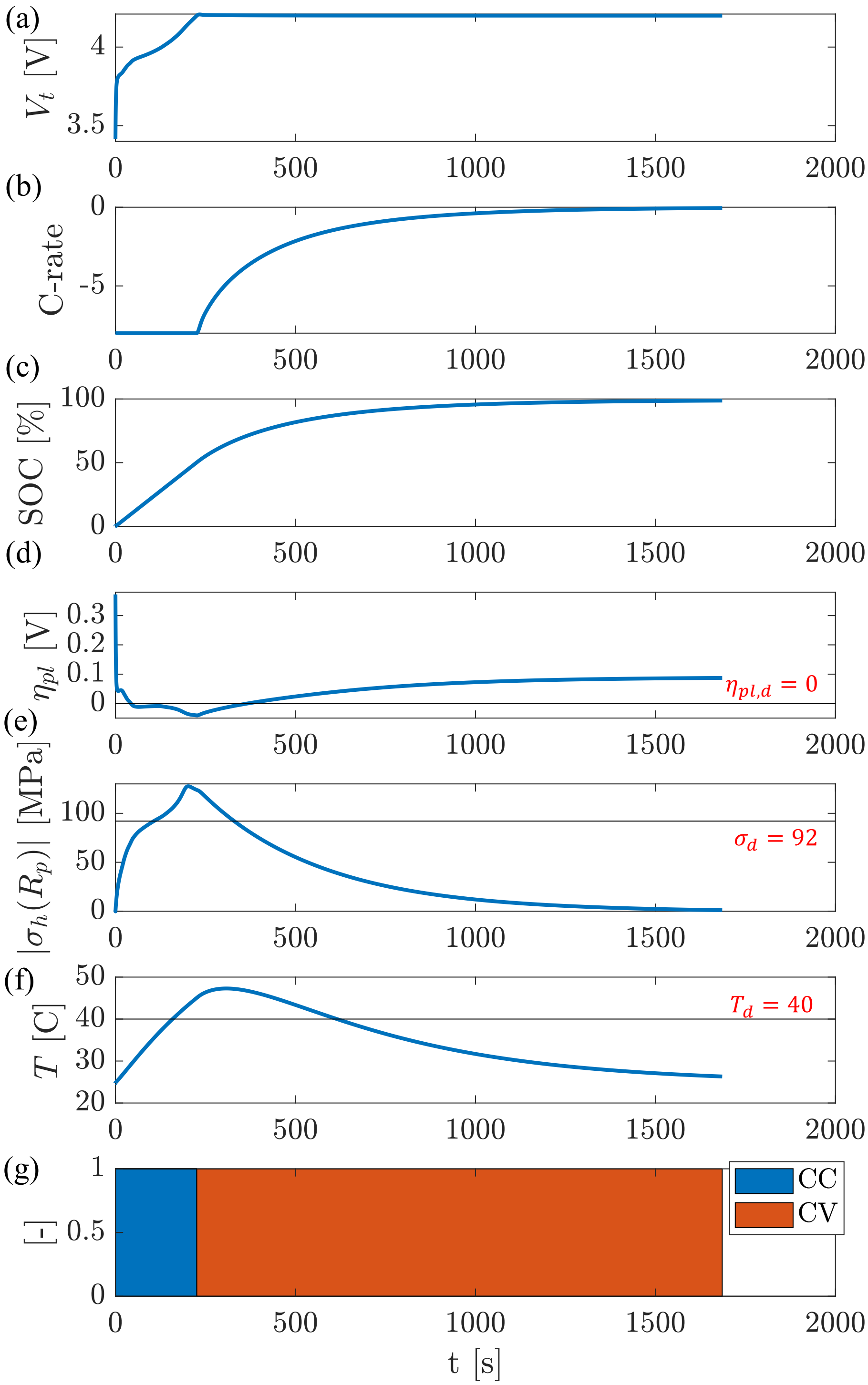

Figure 5.3: The CC-CV charging with 8 C and maximum voltage of 4.2 V. a) the voltage, b) the C-rate, c) the SOC, d) the plating potential, e) the stress, f) the temperature, and g) the charge-phase indicator. The limits shown in the plots for temperature, plating potential, and stress are violated.

In the second scenario, only the temperature and voltage constraints are considered. Similarly to the mechanical stress, the entire response for the temperature is shown in Figure 5.2 (d) with the highlighted region shown in Figure 5.2 (e) and in Figure 5.2 (f) for the input current. The simulation was done with values of $K_{P,T} = [0, 50, 500]$. Again, as can be seen, the oscillations are reduced completely by adding the proportional gain.

5.4.2 CC-CV Charging

The results of charging using the CC-CV method are shown in Figure 5.3. As can be seen, the constraints considered in Equation (5.10) are violated as the CC-CV charging is not aware of these constraints. Therefore, repeated charging under this profile would lead to accelerated aging of the battery.

5.4.3 CC-CV$\eta\sigma$T Charging

The results of charging using the CC-CV$\eta\sigma$T method and the constraints in Equation (5.10) are shown in Figure 5.4. As can be seen, the new algorithm maintained all the variables within the defined limits successfully. The charge-phase indicator shows when the constraints are active, and it is shown in Figure 5.4 (g). At the time t_1, the plating potential reached the minimum, and the plating constraint was active. At the time t_2, the maximum stress was reached, and the stress constraint was active. At the time t_3, the maximum temperature constraint was activated. Finally, at time t_4, the maximum voltage was reached, and the CV phase was active.

The charge times using the CC-CV (Figure 5.3) and CC-CV$\eta\sigma$T (Figure 5.4) algorithms are shown in Table 5.2. The charging time has increased with the new charging algorithm. However, while the charging time is only increased by 100 seconds, it is expected that the aging consequences of fast charging are reduced significantly.

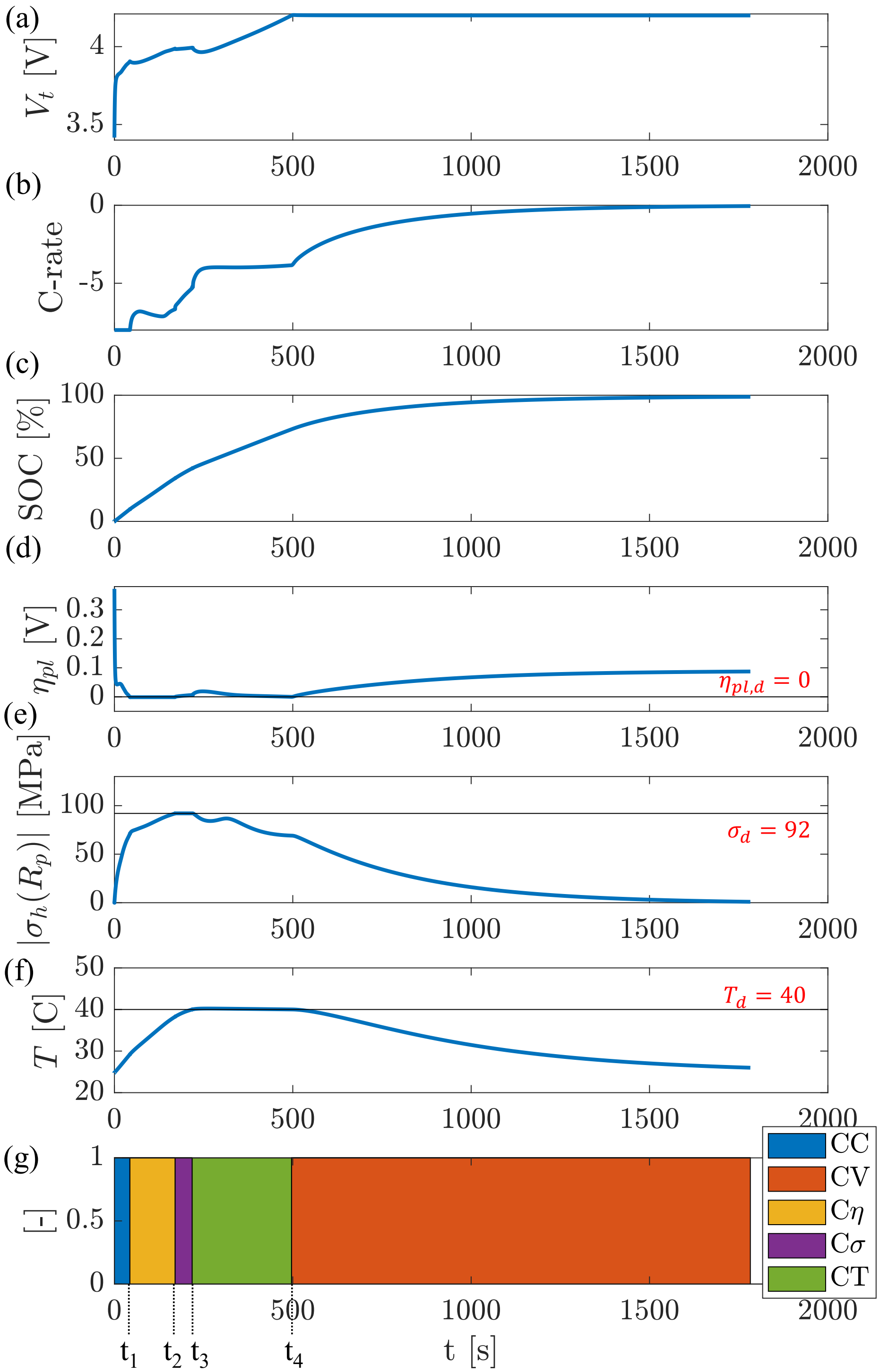

Figure 5.4: The CC-CV$\eta\sigma$T charging with 8 C, maximum voltage of 4.2 V, maximum temperature of 40^oC, minimum plating potential of 0 V, and maximum stress of 92 MPa. a) the voltage, b) the C-rate, c) the SOC, d) the plating potential, e) the stress, f) the temperature, and g) the charge-phase indicator.

SOC range	CC-CV	CC-CV$\eta\sigma$T
0-80%	474 s	580 s
0-100%	1685 s	1783 s

Table 5.2: Charge time

5.4.4 Sensitivity analysis for the plating potential

Errors in estimating the plating potential can stem from uncertainty in model parameters or the reduced-order model itself. Quantifying the effects of all these uncertainties is beyond the scope of this work. Nevertheless, uncertainties can be accounted for by assuming a safety margin for the plating potential. The plating potential's sensitivity during the aging is demonstrated by assuming that the negative electrode's active material ratio, ϵ_s^-, decreases during aging. The current input in Figure 5.5 (a) results from the new charging algorithm with only the plating potential as the constraint. In this case, the fresh active material ratio and a minimum plating potential of zero are utilized. However, as shown in Figure 5.5 (b), when applying this current input to a cell with a reduced active material ratio, the plating potential goes below zero. This means that if the active material ratio is not re-calibrated, the drift in aging parameters can cause an error in the charging algorithm, which leads to more plating.

One way to account for uncertainties is to adjust the constraints. Figure 5.5 (c) shows the input current with a minimum plating potential of 0.02 V as a safety margin. As can be seen in Figure 5.5 (d), the plating potential remains above zero even when the active material ratio is reduce by 10%. Therefore, the plating is prevented even at the aged conditions.

5.5 Summary

In this chapter, we have developed a new charging algorithm based on the CC-CV algorithm. The new algorithm can protect against aging related variables by imposing constraints on them. The new algorithm was used to limit the plating potential, mechanical stress, and temperature during

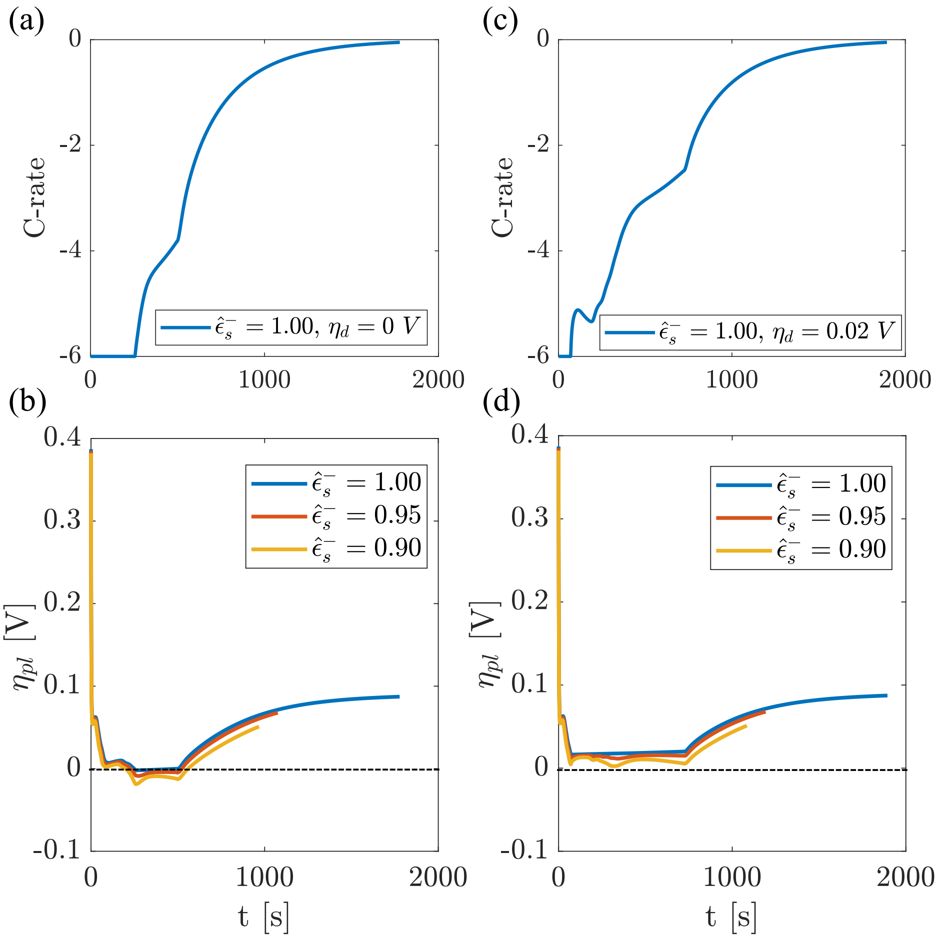

Figure 5.5: a) The input current assuming the active material ratio of fresh cell (normalized active material ratio, $\hat{\epsilon}_s^- = 1$), and a minimum potential of zero. The current was applied to models with the normalized active material ratio of 0.95 and 0.9. b) The plating potential. c) The input current assuming the active material ratio of fresh cell, and a minimum potential of 0.02 V. Similarly this input was applied to models with the normalized active material ratio of 0.95 and 0.9. d) The plating potential response.

charging, and therefore was named CC-CV$\eta\sigma$T (VEST). The new algorithm was tested using an electrochemical model with added mechanical and thermal dynamics. The results showed that new algorithm can limit these parameters successfully. The CC-CV$\eta\sigma$T algorithm is straightforward for implementation since it is based on the CC-CV logic. Additionally, safety margins can be easily considered for each of the parameters.

CHAPTER 6

Conclusions and Future Work

6.1 Results and Conclusions

In this work, using fundamental analysis, the benefits of incorporating cell expansion measurement for the diagnostic algorithm were studied. It was found that for estimating electrode-specific parameters corresponding to the individual electrode capacity and the utilization window, the expansion measurements have several advantages. In order to quantify the benefits of the expansion measurements, the identifiability of individual electrode parameters with measurement noise was performed, and the standard error of the parameters was calculated using the Cramer-Rao bound analysis. The identifiability of the individual electrode parameters using the constrained Cramer-Rao bound formulation was compared for two scenarios of voltage measurement alone and voltage plus expansion measurements. It was shown that for the voltage-only case that the voltage measurements should be taken at a wider range of SOC, across at least two phase transitions, in order to make all the parameters identifiable. However, with the addition of expansion measurements, the parameters were identifiable at the shallower depth of discharges.

The results indicate that the identifiability of the individual electrode parameters is closely related to the slope changes of the open circuit potential and expansion. As a result, for material like LFP that has a flat voltage response at middle SOC regions, the estimation of the individual electrode parameters is only possible with the inclusion of the expansion measurements.

The analysis was based on a set of simplifying assumptions, and the goal was to study the usefulness of the expansion measurements under limited data and the presence of noise. The conclusion was that having the additional expansion information is not only beneficial, but it is also necessary for high-confidence eSOH estimation when the range of available data in SOC is limited.

Furthermore, in this work, an experimental campaign was conducted to characterize battery expansion over the cell life under a variety of conditions. To this end, a number of graphite/NMC pouch cell were fabricated at the University of Michigan Battery Lab. A fixture was designed to measure the expansion of the cell. Periodic characterization tests were also performed, including capacity measurement at C/20, resistance measurement, and charge response with different C-rates. The measurements of expansion and voltage at C/20 from fresh to aged states were used to validate the results of the identifiability analysis.

The measurements of charge response at different C-rates were utilized to develop a capacity estimation method based on voltage and expansion. It was established that the features in the differential voltage (DV), incremental capacity (IC), and differential expansion (DE) signals are great candidates for developing capacity estimation methods. The evolution of the selected features in the DV, IC, and DE signals over time were compared with the battery capacity. The results showed that the identified features have a correlation with capacity that was nearly linear under a wide range of aging conditions. Different linear regression models were fitted to the data by considering all the combinations of the features. It was discovered that utilizing the IC and DE features results in the best method for capacity estimation in terms of accuracy. Also, the expansion feature has several qualities, which makes it more useful for plug-in electric vehicles; namely, the feature occurs in the middle of the SOC range, it is observable up to 1C, and it is robust to a change in the initial SOC.

Moreover, a reduced order model with particle size distribution and mechanical expansion was developed to capture the smoothing of the differential voltage signal at C-rate above 1C. The model consists of an electrochemical model for the porous electrode, mechanical expansion, and energy balance dynamics. A concentration-dependent volume change in the graphite electrode is considered to achieve higher accuracy. The total expansion of the cell was calculated by adding the intercalation expansion and the thermal expansion. It was demonstrated that, unlike differential voltage, the peaks in the differential expansion curve are observable up to 1C rate, and this makes the differential expansion a good candidate method for capacity estimation during fast charging scenarios (above C/2). Unlike the more established single particle model (SPM), the new multi-particle model is able to capture the peak smoothing behavior. The model parameters were identified using experimental data collected from the graphite/NMC pouch cell.

The simulated profiles fit the measured data well after determining the additional thermal expansion by pulse excitation measurements. The experimental and simulated expansion curves for constant current charge rates at C/5, C/2, 1C, and 2C were in good agreement. Both the experimental and simulated data showed the peak smoothing of the cell's differential expansion as the charge rates increases.

It was noted that the multi-particle model with different particle sizes results in a distribution of concentration among the particles. This non-uniform charging of particles can happen at higher rates and is causing the smoothing effect observed in the data. The peaks in the differential expansion are sustained at higher rates, while the differential voltage peaks disappear because the voltage is a function of the surface concentration, while expansion is a function of the average concentration in the particle.

Finally, a new fast-charging algorithm was developed. The new algorithm was established following the logic of the CC-CV charging protocol. However, the new algorithm can also protect against aging-related variables like the plating potential, mechanical stress, and temperature. The new algorithm achieved this goal by imposing constraints on the aging related variables. Since the new algorithm imposed limits on the plating potential, the mechanical stress, and the temperature during charging, it was named CC-CV$\eta\sigma$T (VEST). The new algorithm was tested using an electrochemical model with added mechanical and thermal dynamics developed in this work. The results showed that the new algorithm can limit these parameters successfully. The CC-CV$\eta\sigma$T algorithm is straightforward for implementation, and safety margins can be easily implemented for each of the parameters.

In conclusion, in this thesis, it was shown that cell diagnostics can benefit significantly by incorporating a single sensor measurement of the cell's overall thickness changes. It was demonstrated that using a simple model of the reversible part of the expansion and fundamental identifiability analysis, the expansion measurement improves the estimation confidence levels and drastically reduces the data requirement and diagnostic test time, which is crucial for automotive applications.

6.2 Future Work and Open Challenges

This work showcased the ability to improve the battery diagnostics using expansion measurements. Nevertheless, there are still several challenges that need to be addressed. Overall, our study shows that for health estimation and diagnostics tangible benefits can be gained by including the expansion measurements. These benefits can be in terms of improving the confidence-levels for diagnostics during cycling in the lab, cell screening in a production line, or field applications. However, more work must be done to develop cost effective expansion sensors and also assess the feasibility of the diagnostics using expansion for different chemistries and cell form factors. In the following, an overview of the potential avenues of extending the work of this dissertation in the future is discussed. Moreover, a perspective is given on the open challenges and future opportunities of the expansion measurement utilization.

Temperature effects. The mechanistic model of the open-circuit potentials was done assuming operation at the room temperature. It is known that the open-circuit potential varies with the change in temperature. Future work will address the sensitivity of the eSOH estimation with respect to the temperature. Furthermore, the dynamic model of the expansion was also done at the room temperature. Future work should consider the effects of the operating temperature on the pack/fixture structure and its influence on the expansion measurements.

Model parameter identification. In terms of modeling the expansion, identifying the parameters remains challenging, and the impact of the fixture/pack design on the expansion requires careful modeling and parameter identification. Tracking the changes in the parameters as the cell ages also requires careful consideration of different aspects of cell aging. While in this work, it was shown that with expansion, the frequency of capacity and electrode diagnostics can increase greatly, the calibration of other parameters as the cell ages were not addressed directly. Future work should address the identification of parameters such as film resistance and porosity as the cell ages.

Active pressure control. The fixture utilized in this work was designed to passively maintain a uniform and constant pressure on the cell by using compression springs. This was achieved by using spring modulus that is much lower than the battery's modulus, which ensures almost constant pressure on the cell as it expands. Although the fixture was largely successful in maintaining the pressure for the batteries in this work, there are number of factors that may limits its use in general. For example, the maximum pressure that can be applied is limited by the spring modulus and length. Furthermore, online adjustment of the pressure is not possible. Future work may consider fixture designs with active pressure control using pneumatic actuators and pressure sensor feedback systems.

Quantification of parameters' uncertainty The new CC-CV$\eta\sigma$T fast charging algorithm relies on the accurate knowledge of the model parameters. The uncertainty in model parameters can be considered as additional margins on the aging-related variables, like plating potential and mechanical stress. Future work should address the impact of the parameters' uncertainties on the constraints related to the various aging-related variables in the fast charging algorithm.

Aging models of expansion evolution. Physics-based predictive aging models are mostly concerned with predicting the capacity fade and resistance growth. Although several aging models developed in recent years include dynamics for mechanical degradation and failure, the modeling of the cell expansion and its coupling effect on the mechanical degradation is largely understudied. Future work should examine physics-based approaches for developing predictive models of the cell expansion evolution during aging.

Battery Safety. Battery internal short circuit event results in a high temperature in the cell that triggers side reactions, which produce a large amount of gas [108]. The generated gas leads to sudden swelling of the pouch cell measurable as an increase in the expansion/force at the pack level. It has been shown that the detection of battery failure can benefit from monitoring the expansion force in packs [109]. Therefore, the inclusion of force/expansion sensors can also be motivated from the battery safety perspective.

Instrumentation in large packs. It should also be pointed out that in terms of real-world implementation of expansion measurements, the instrumentation of large battery packs with expansion/force sensors remains challenging. Nevertheless, utilization of thin-film displacement sensors for pouch type cells [110], and strain gauges for cylindrical cells [111] have shown encouraging results to overcome some of these challenges. Therefore, it is anticipated that the efforts to develop cost-effective instrumentation for prismatic and pouch cell configurations in packs intensify in the near future.

Future battery technologies. The next generation anode materials with Si/C composites, the cycle life of these cells is highly dependent on the external pressure [78], and for solid-state batteries with lithium metal as the anode, it is necessary to account for the changes in cell expansion during charging and discharging due to Li plating and stripping, along with the changes during aging and preventing accelerated aging by adjusting the applied pressure [112]. Thus the inclusion and development of expansion sensors and active pressure controls might be necessary for future battery packs.

Appendices

APPENDIX A

Mixed Aging Cycling

An important research question in the area of prognosis is that how we can reliably predict the battery lifetime in the field using the models developed and data gathered in the lab [113]. The field data is irregular and the usage profile can change overtime, for example, for second-life batteries were batteries are re-purposed for electrical energy storage [11].

The impact of changes to the usage profile is explored here experimentally by switching the cycling temperature after a certain number of cycles. This concept is shown schematically in Figure A.1 . The summary of the mixed aging conditions are shown in Table A.1. The first two conditions consist of cycling at the hot temperature and then switch to cold temperature cycling, at cycle 100 and 50, respectively. The subsequent two conditions consist of cycling at the cold temperature and then switch to hot temperature cycling, at cycle 120 and 70, respectively. The details of cycling procedure are as same as the Table 3.2.

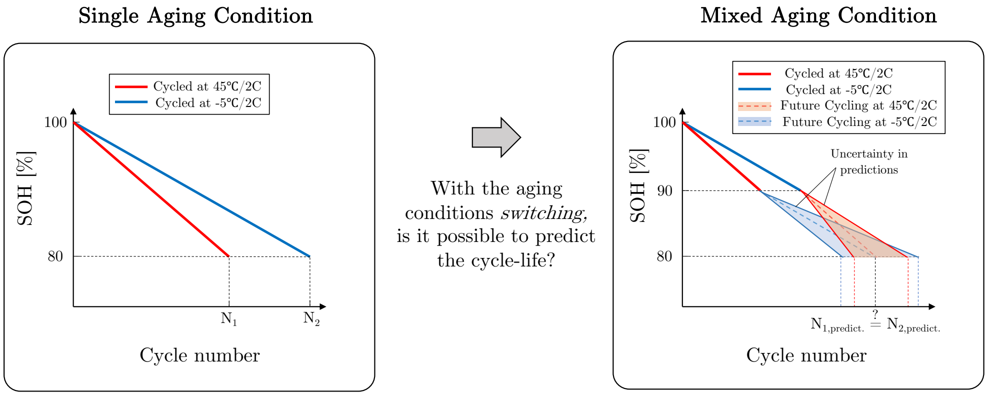

Figure A.1: The schematic of the mixed aging conditions

Mixed aging conditions			
Cell number - charging sequence[a]	DOD	Charge[b]	Discharge
01M | H→C @cycle=100	0-100%	2C	2C
02M | H→C @cycle=50	0-100%	2C	2C
03M | C→H @cycle=120	0-100%	2C	2C
04M | C→H @cycle=70	0-100%	2C	2C

Table A.1: The mixed aging test conditions. [a] The R, C, and H corresponds to room ($25°C$), cold ($-5°C$), and hot ($45°C$) temperature. [b] Constant current until 4.2 V and then constant voltage until ($I < C/50$).

The goal here is to assess the path dependence of cell aging by varying the cycling condition and compare the results with a cell that has been cycled only with one condition until the end of life. The capacity retention results of the mixed aging cells 01M and 02M are shown in Figure A.2 (a). The portion of the line colored in red corresponds to the cycling at the hot temperature, followed by the blue colored section, which represents the cold temperature cycling. In Figure A.2 (b) and (c), the mixed aging cycling is compared with a continuously cycled cell at hot and cold temperatures, respectively. The capacity retention evolution of the initial hot temperature cycles follows closely the continues hot temperature cycling in Figure A.2 (b), and diverges as expected when the cycling conditions switched to the cold temperature. However, as can be seen in Figure A.2 (c), the cold temperature aging doesn't follow the continuously cycled cell at the cold temperature.

Similarly, the capacity retention results of the mixed aging cells 03M and 04M are shown in Figure A.3 (a). The portion of the line colored in blue corresponds to the cycling at the cold temperature, followed by the red colored section, which represents the hot temperature cycling. In Figure A.3 (b) and (c), the mixed aging cycling is compared with a continuously cycled cell at cold and hot temperatures, respectively. Similar to the case in Figure A.2 (b), the capacity retention evolution of the initial cold temperature cycles follows closely the continues cold temperature cycling in Figure A.3 (b), and diverges as expected when the cycling conditions switched to the hot temperature. As can be seen in Figure A.3 (c), the hot temperature aging doesn't follow the continuously cycled cell at the hot temperature.

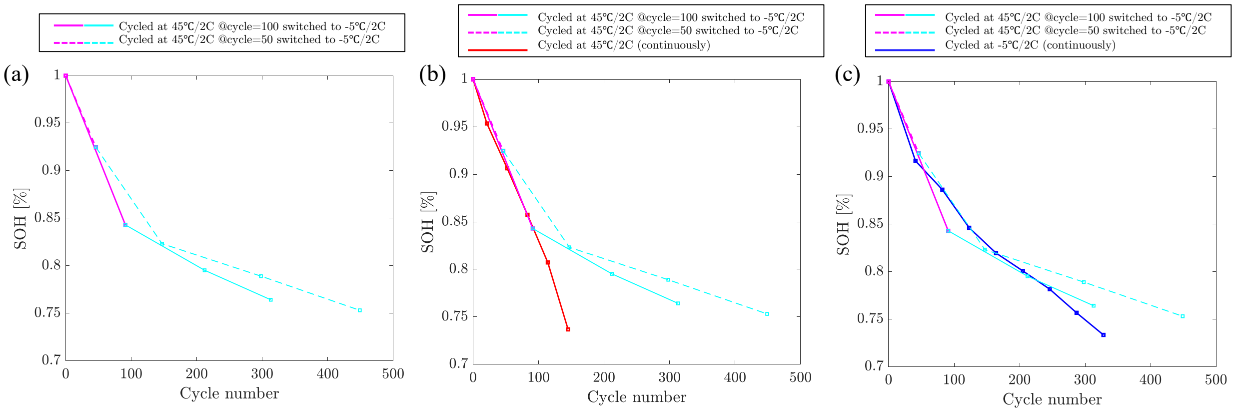

Figure A.2: a) The capacity retention of cells 01M and 02M, b) the comparison with the hot continuously cell, and c) the comparison with the cold continuously cell.

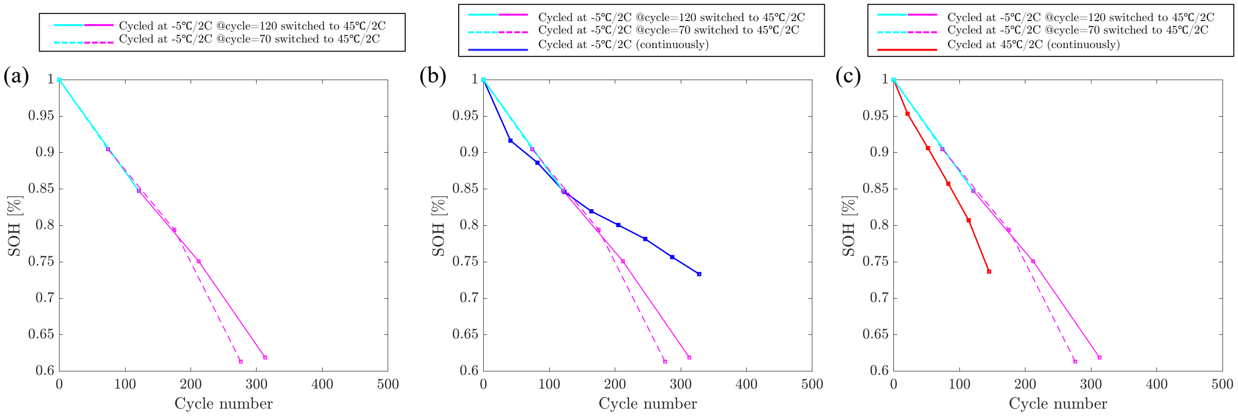

Figure A.3: a) The capacity retention of cells 03M and 04M, b) the comparison with the cold continuously cell, and c) the comparison with the hot continuously cell.

Lastly, the eSOH parameters are estimated for the mixed aging condition cells and the results are shown in Figures A.4 and A.5. The results indicate the similar story of the capacity retention. Meaning, the initial evolution follows the hot continuously cycled cell in Figure A.4 (a), however, the subsequent cold temperature cycles diverge from the continuously cold temperature cycling in Figure A.4 (b). The results in Figure A.5 (a) and (b) also point to the path dependence of the aging since the evolution of eSOH parameters are quite different between the two conditions.

Overall, the results highlights the importance of the inherently non-linear, path-dependent na-

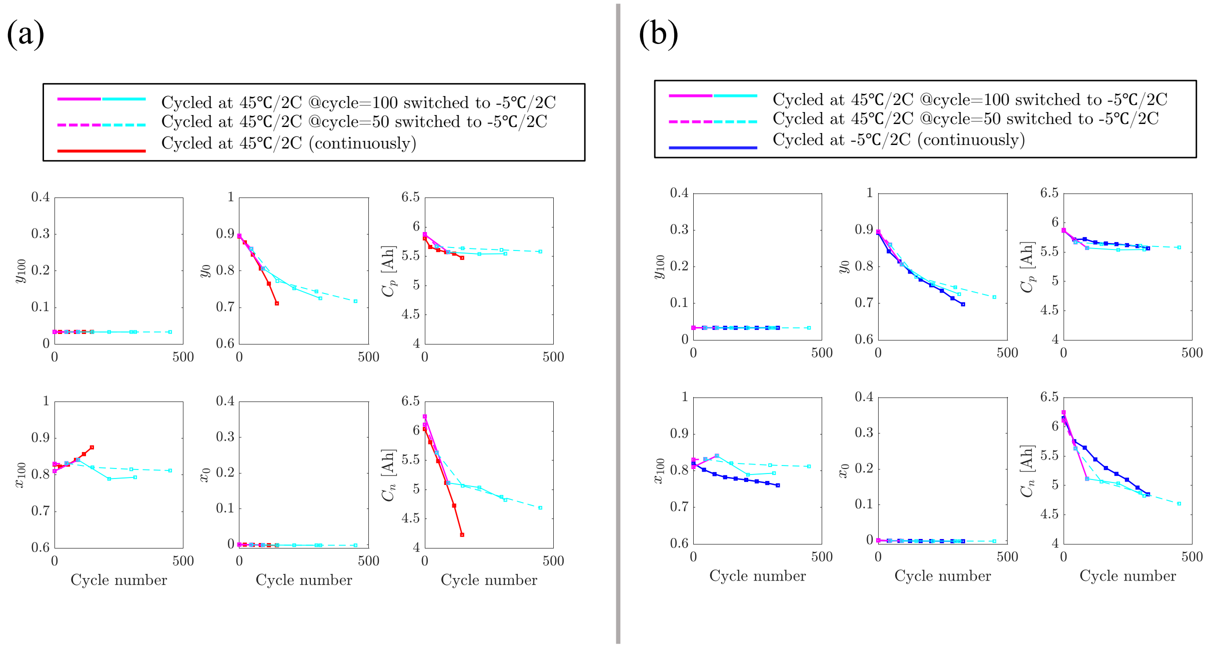

Figure A.4: a) The eSOH parameters of cell 01M and 02M compared to the eSOH parameters of the continuously cycled cell at the hot temperature, and b) cold temperature.

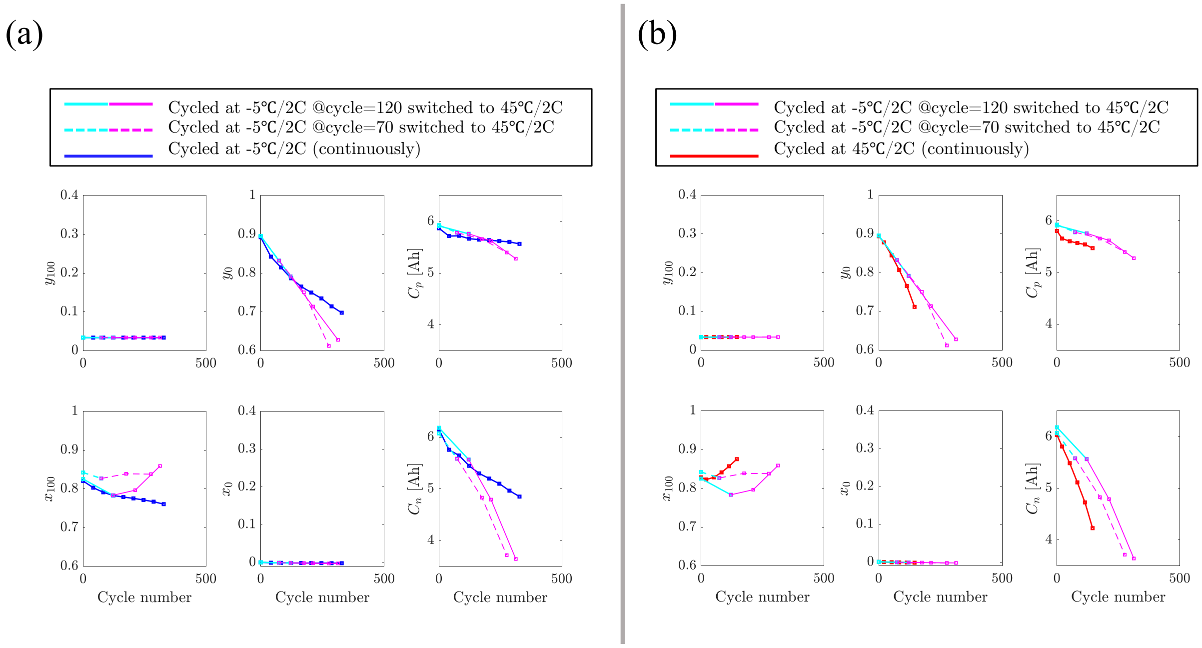

Figure A.5: a) The eSOH parameters of cell 03M and 04M compared to the eSOH parameters of the continuously cycled cell at the hot temperature, and b) cold temperature.

ture of battery degradation [114, 115], which is an important factor for real-world applications with irregular cycling patterns and varying operating conditions. Furthermore, cells in a pack can experience different temperatures in their lifetime due resulting in path-dependence of capacity fade [115]. There are still open challenges regarding the prediction of the remaining useful life of electric vehicle or grid storage systems using real-world data.

BIBLIOGRAPHY

[1] Environmental Protection Agency. *Fast Facts on Transportation Greenhouse Gas Emissions*. Jul 2020.

[2] IEA. *Global EV Outlook 2020 – Analysis*.

[3] Atsuo Yamada, Sai-Cheong Chung, and Koichiro Hinokuma. Optimized lifepo4 for lithium battery cathodes. *Journal of the electrochemical society*, 148(3):A224–A229, 2001.

[4] Norio Takami, Asako Satoh, Michikazu Hara, and Takahisa Ohsaki. Structural and kinetic characterization of lithium intercalation into carbon anodes for secondary lithium batteries. *Journal of the Electrochemical Society*, 142(2):371–379, 1995.

[5] Yue Qi, Haibo Guo, Louis G Hector Jr, and Adam Timmons. Threefold increase in the young's modulus of graphite negative electrode during lithium intercalation. *Journal of The Electrochemical Society*, 157(5):A558, 2010.

[6] Ping Tang and N. A. W. Holzwarth. Electronic structure of fepo_4, lifepo_4, and related materials. *Phys. Rev. B*, 68:165107, Oct 2003.

[7] Sravan Pannala, Puneet Valecha, Peyman Mohtat, Jason B Siegel, and Anna G Stefanopoulou. Improved battery state estimation under parameter uncertainty caused by aging using expansion measurements. *arXiv preprint arXiv:2009.14270*, 2020.

[8] Peyman Mohtat, Suhak Lee, Jason B Siegel, and Anna G Stefanopoulou. Towards better estimability of electrode-specific state of health: Decoding the cell expansion. *J. Power Sources*, 427:101–111, 2019.

[9] IPCC. *Summary for Policymakers*, book section SPM, page 1–30. Cambridge University Press, Cambridge, United Kingdom and New York, NY, USA, 2013.

[10] Karim Hamza, Ken Laberteaux, and Kang-Ching Chu. On modeling the total cost of ownership of electric and plug-in hybrid vehicles. Technical report, SAE Technical Paper, 2020.

[11] E. Martinez-Laserna, I. Gandiaga, E. Sarasketa-Zabala, J. Badeda, D. I. Stroe, M. Swierczynski, and A. Goikoetxea. Battery second life: Hype, hope or reality? A critical review of the state of the art. *Renewable and Sustainable Energy Reviews*, 93(April):701–718, 2018.

[12] Jens Vetter, Petr Novák, Markus Robert Wagner, Claudia Veit, K-C Möller, JO Besenhard, Martin Winter, Margret Wohlfahrt-Mehrens, Christoph Vogler, and Abderrezak Hammouche. Ageing mechanisms in lithium-ion batteries. *Journal of power sources*, 147(1-2):269–281, 2005.

[13] K. B. Hatzell, A. Sharma, and H. K. Fathy. A survey of long-term health modeling, estimation, and control of lithium-ion batteries: Challenges and opportunities. In *2012 American Control Conference (ACC)*, pages 584–591, June 2012.

[14] Christoph R Birkl, Matthew R Roberts, Euan McTurk, Peter G Bruce, and David A Howey. Degradation diagnostics for lithium ion cells. *Journal of Power Sources*, 341:373–386, 2017.

[15] Matthieu Dubarry, Cyril Truchot, and Bor Yann Liaw. Synthesize battery degradation modes via a diagnostic and prognostic model. *Journal of Power Sources*, 219:204 – 216, 2012.

[16] Caihao Weng, Yujia Cui, Jing Sun, and Huei Peng. On-board state of health monitoring of lithium-ion batteries using incremental capacity analysis with support vector regression. *Journal of Power Sources*, 235:36–44, 2013.

[17] Gregory L Plett. Dual and joint ekf for simultaneous soc and soh estimation. In *Proceedings of the 21st Electric Vehicle Symposium (EVS21), Monaco*, pages 1–12, 2005.

[18] Scott J Moura, Miroslav Krstic, and Nalin A Chaturvedi. Adaptive pde observer for battery soc/soh estimation. In *Dynamic Systems and Control Conference*, volume 45295, pages 101–110. American Society of Mechanical Engineers, 2012.

[19] Shyh-Chin Huang, Kuo-Hsin Tseng, Jin-Wei Liang, Chung-Liang Chang, and Michael G Pecht. An online soc and soh estimation model for lithium-ion batteries. *Energies*, 10(4):512, 2017.

[20] Shankar Mohan, Youngki Kim, and Anna G Stefanopoulou. Estimating the power capability of li-ion batteries using informationally partitioned estimators. *IEEE Transactions on Control Systems Technology*, 24(5):1643–1654, 2016.

[21] Ira Bloom, Andrew N Jansen, Daniel P Abraham, Jamie Knuth, Scott A Jones, Vincent S Battaglia, and Gary L Henriksen. Differential voltage analyses of high-power, lithium-ion cells: 1. technique and application. *Journal of Power Sources*, 139(1-2):295–303, 2005.

[22] Xiaoyu Li, Zhenpo Wang, Lei Zhang, Changfu Zou, and David D Dorrell. State-of-health estimation for li-ion batteries by combing the incremental capacity analysis method with grey relational analysis. *Journal of Power Sources*, 410:106–114, 2019.

[23] Suhak Lee, Peyman Mohtat, Jason B Siegel, Anna G Stefanopoulou, Jang-Woo Lee, and Tae-Kyung Lee. Estimation error bound of battery electrode parameters with limited data window. *IEEE Transactions on Industrial Informatics*, 16(5):3376–3386, 2019.

[24] Peyman Mohtat, Farinaz Nezampasandarbabi, Shankar Mohan, Jason B Siegel, and Anna G Stefanopoulou. On identifying the aging mechanisms in li-ion batteries using two points measurements. In *2017 American Control Conference (ACC)*, pages 98–103. IEEE, 2017.

[25] Suhak Lee, Peyman Mohtat, Jason B Siegel, and Anna G Stefanopoulou. Beyond estimating battery state of health: identifiability of individual electrode capacity and utilization. In *2018 Annual American Control Conference (ACC)*, pages 2288–2293. IEEE, 2018.

[26] Dong Zhang, Satadru Dey, and Scott J Moura. Lithium-ion battery state estimation for a single particle model with intercalation-induced stress. In *2018 Annual American Control Conference (ACC)*, pages 2294–2299. IEEE, 2018.

[27] Xin Zhou, Jeffrey L. Stein, and Tulga Ersal. Battery state of health monitoring by estimation of the number of cyclable li-ions. *Control Engineering Practice*, 66:51 – 63, 2017.

[28] Ningxin Zhang and Huaqiong Tang. Dissecting anode swelling in commercial lithium-ion batteries. *Journal of Power Sources*, 218:52–55, 2012.

[29] Xinghua Yu, Zhili Feng, Yang Ren, Daniel Henn, Zhenggang Wu, Ke An, Bi Wu, Christian Fau, Chen Li, and Stephen J Harris. Simultaneous operando measurements of the local temperature, state of charge, and strain inside a commercial lithium-ion battery pouch cell. *Journal of The Electrochemical Society*, 165(7):A1578, 2018.

[30] Jason B Siegel, Anna G Stefanopoulou, Patrick Hagans, Yi Ding, and David Gorsich. Expansion of lithium ion pouch cell batteries: Observations from neutron imaging. *Journal of the Electrochemical Society*, 160(8):A1031, 2013.

[31] Jae Hyun Lee, Hyang Mok Lee, and Soonho Ahn. Battery dimensional changes occurring during charge/discharge cycles thin rectangular lithium ion and polymer cells. *Journal of power sources*, 119:833–837, 2003.

[32] Victor A Agubra, Jeffrey W Fergus, Rujian Fu, and Song-Yul Choe. Analysis of effects of the state of charge on the formation and growth of the deposit layer on graphite electrode of pouch type lithium ion polymer batteries. *Journal of power sources*, 270:213–220, 2014.

[33] Barbara Michalak, Heino Sommer, David Mannes, Anders Kaestner, Torsten Brezesinski, and Jürgen Janek. Gas evolution in operating lithium-ion batteries studied in situ by neutron imaging. *Scientific reports*, 5:15627, 2015.

[34] Claudia Birkenmaier, Bernhard Bitzer, Matthias Harzheim, Andreas Hintennach, and Thomas Schleid. Lithium plating on graphite negative electrodes: innovative qualitative and quantitative investigation methods. *Journal of The Electrochemical Society*, 162(14):A2646, 2015.

[35] Johannes Sturm, Franz B Spingler, Bernhard Rieger, Alexander Rheinfeld, and Andreas Jossen. Non-destructive detection of local aging in lithium-ion pouch cells by multi-directional laser scanning. *Journal of The Electrochemical Society*, 164(7):A1342, 2017.

[36] Marius Bauer, Mario Wachtler, Hendrik Stöwe, Jon V Persson, and Michael A Danzer. Understanding the dilation and dilation relaxation behavior of graphite-based lithium-ion cells. *Journal of Power Sources*, 317:93–102, 2016.

[37] Zachary J Schiffer, John Cannarella, and Craig B Arnold. Strain derivatives for practical charge rate characterization of lithium ion electrodes. *Journal of The Electrochemical Society*, 163(3):A427–A433, 2016.

[38] Shankar Mohan, Youngki Kim, Jason B Siegel, Nassim A Samad, and Anna G Stefanopoulou. A phenomenological model of bulk force in a li-ion battery pack and its application to state of charge estimation. *J. Electrochem*, 161(14):A2222, 2014.

[39] Miriam A Figueroa-Santos, Jason B Siegel, and Anna G Stefanopoulou. Leveraging cell expansion sensing in state of charge estimation: Practical considerations. *Energies*, 13(10):2653, 2020.

[40] John Cannarella and Craig B Arnold. State of health and charge measurements in lithium-ion batteries using mechanical stress. *Journal of Power Sources*, 269:7–14, 2014.

[41] Nassim A Samad, Youngki Kim, Jason B Siegel, and Anna G Stefanopoulou. Battery capacity fading estimation using a force-based incremental capacity analysis. *J. Electrochem*, 163(8):A1584, 2016.

[42] John Cannarella and Craig B Arnold. Stress evolution and capacity fade in constrained lithium-ion pouch cells. *Journal of Power Sources*, 245:745–751, 2014.

[43] Anup Barai, Ravichandra Tangirala, Kotub Uddin, Julie Chevalier, Yue Guo, Andrew McGordon, and Paul Jennings. The effect of external compressive loads on the cycle lifetime of lithium-ion pouch cells. *Journal of Energy Storage*, 13:211–219, 2017.

[44] Abdilbari Shifa Mussa, Matilda Klett, Göran Lindbergh, and Rakel Wreland Lindström. Effects of external pressure on the performance and ageing of single-layer lithium-ion pouch cells. *Journal of Power Sources*, 385:18–26, 2018.

[45] Verena Müller, Rares-George Scurtu, Michaela Memm, Michael A Danzer, and Margret Wohlfahrt-Mehrens. Study of the influence of mechanical pressure on the performance and aging of lithium-ion battery cells. *Journal of Power Sources*, 440:227148, 2019.

[46] Long Zhou, Licong Xing, Yuejiu Zheng, Xin Lai, Jinhuan Su, Cong Deng, and Tao Sun. A study of external surface pressure effects on the properties for lithium-ion pouch cells. *International Journal of Energy Research*, 2020.

[47] Zachary J. Schiffer, John Cannarella, and Craig B. Arnold. Strain derivatives for practical charge rate characterization of lithium ion electrodes. *Journal of The Electrochemical Society*, 163(3):A427–A433, dec 2015.

[48] Peyman Mohtat, Suhak Lee, Valentin Sulzer, Jason B Siegel, and Anna G Stefanopoulou. Differential expansion and voltage model for li-ion batteries at practical charging rates. *J. Electrochem*, 167(11):110561, 2020.

[49] Ki-Yong Oh, Bogdan I Epureanu, Jason B Siegel, and Anna G Stefanopoulou. Phenomenological force and swelling models for rechargeable lithium-ion battery cells. *Journal of Power Sources*, 310:118–129, 2016.

[50] Jake Christensen. Modeling diffusion-induced stress in li-ion cells with porous electrodes. *Journal of the Electrochemical Society*, 157(3):A366, 2010.

[51] Fuqian Yang. Interaction between diffusion and chemical stresses. *Materials Science and Engineering: A*, 409(1-2):153–159, 2005.

[52] Bernhard Rieger, Simon V Erhard, Katharina Rumpf, and Andreas Jossen. A new method to model the thickness change of a commercial pouch cell during discharge. *Journal of The Electrochemical Society*, 163(8):A1566, 2016.

[53] Bala S Haran, Branko N Popov, and Ralph E White. Determination of the hydrogen diffusion coefficient in metal hydrides by impedance spectroscopy. *Journal of Power Sources*, 75(1):56–63, 1998.

[54] Scott J Moura, Federico Bribiesca Argomedo, Reinhardt Klein, Anahita Mirtabatabaei, and Miroslav Krstic. Battery state estimation for a single particle model with electrolyte dynamics. *IEEE Transactions on Control Systems Technology*, 25(2):453–468, 2016.

[55] Scott G Marquis, Valentin Sulzer, Robert Timms, Colin P Please, and S Jon Chapman. An asymptotic derivation of a single particle model with electrolyte. *Journal of The Electrochemical Society*, 166(15):A3693, 2019.

[56] Anna Tomaszewska, Zhengyu Chu, Xuning Feng, Simon O'Kane, Xinhua Liu, Jingyi Chen, Chenzhen Ji, Elizabeth Endler, Ruihe Li, Lishuo Liu, et al. Lithium-ion battery fast charging: A review. *ETransportation*, 1:100011, 2019.

[57] R Klein, N a Chaturvedi, J Christensen, J Ahmed, R Findeisen, and a Kojic. Optimal charging strategies in lithium-ion battery. *American Control Conference*, pages 382–387, 2011.

[58] Hector Eduardo Perez, Xiaosong Hu, Satadru Dey, and Scott J Moura. Optimal charging of li-ion batteries with coupled electro-thermal-aging dynamics. *IEEE Transactions on Vehicular Technology*, 66(9):7761–7770, 2017.

[59] Fredric Lam, Anirudh Allam, Won Tae Joe, Yohwan Choi, and Simona Onori. Offline multiobjective optimization for fast charging and reduced degradation in lithium-ion battery cells using electrochemical dynamics. *IEEE Control Systems Letters*, 2020.

[60] Bharatkumar Suthar, Venkatasailanathan Ramadesigan, Sumitava De, Richard D. Braatz, and Venkat R. Subramanian. Optimal charging profiles for mechanically constrained lithium-ion batteries. *Phys. Chem. Chem. Phys.*, 16(1):277–287, 2014.

[61] Saehong Park, Donggun Lee, Hyoung Jun Ahn, Claire Tomlin, and Scott Moura. Optimal control of battery fast charging based-on Pontryagin's minimum principle. In *2020 59th IEEE Conference on Decision and Control (CDC)*, pages 3506–3513. IEEE, 2020.

[62] Lalit Patnaik, AVJS Praneeth, and Sheldon S Williamson. A closed-loop constant-temperature constant-voltage charging technique to reduce charge time of lithium-ion batteries. *IEEE Transactions on Industrial Electronics*, 66(2):1059–1067, 2018.

[63] Wei-Jen Lai, Mohammed Yusuf Ali, and Jwo Pan. Mechanical behavior of representative volume elements of lithium-ion battery cells under compressive loading conditions. *Journal of Power Sources*, 245:609–623, 2014.

[64] Bernhard Rieger, Steffen Schlueter, Simon V Erhard, and Andreas Jossen. Strain propagation in lithium-ion batteries from the crystal structure to the electrode level. *Journal of The Electrochemical Society*, 163(8):A1595, 2016.

[65] Todd R Ferguson and Martin Z Bazant. Nonequilibrium thermodynamics of porous electrodes. *Journal of The Electrochemical Society*, 159(12):A1967–A1985, 2012.

[66] Martin Winter, Jürgen O. Besenhard, Michael E. Spahr, and Petr Novák. Insertion electrode materials for rechargeable lithium batteries. *Advanced Materials*, 10(10):725–763, 1998.

[67] Bruno Scrosati and Jürgen Garche. Lithium batteries: Status, prospects and future. *Journal of Power Sources*, 195(9):2419–2430, 2010.

[68] Mohammad Farkhondeh, Mark Pritzker, Michael Fowler, Mohammadhosein Safari, and Charles Delacourt. Mesoscopic modeling of li insertion in phase-separating electrode materials: application to lithium iron phosphate. *Physical Chemistry Chemical Physics*, 16(41):22555–22565, 2014.

[69] S Flandrois and B Simon. Carbon materials for lithium-ion rechargeable batteries. *Carbon*, 37(2):165–180, 1999.

[70] Amartya Mukhopadhyay and Brian W Sheldon. Deformation and stress in electrode materials for li-ion batteries. *Progress in Materials Science*, 63:58–116, 2014.

[71] Petre Stoica and Boon Chong Ng. On the cramér-rao bound under parametric constraints. *IEEE Signal Processing Letters*, 5(7):177–179, 1998.

[72] C. Jauffret. Observability and fisher information matrix in nonlinear regression. *IEEE Transactions on Aerospace and Electronic Systems*, 43(2):756–759, April 2007.

[73] Xiaoyu Li, Guodong Fan, Ke Pan, Guo Wei, Chunbo Zhu, Giorgio Rizzoni, and Marcello Canova. A physics-based fractional order model and state of energy estimation for lithium ion batteries. part i: Model development and observability analysis. *Journal of Power Sources*, 367:187 – 201, 2017.

[74] M Safari and C Delacourt. Modeling of a commercial graphite/lifepo4 cell. *Journal of The Electrochemical Society*, 158(5):A562–A571, 2011.

[75] Ira Bloom, Andrew N. Jansen, Daniel P. Abraham, Jamie Knuth, Scott A. Jones, Vincent S. Battaglia, and Gary L. Henriksen. Differential voltage analyses of high-power, lithium-ion cells: 1. technique and application. *Journal of Power Sources*, 139(1):295 – 303, 2005.

[76] PK Leung, C Moreno, Iain Masters, Sumit Hazra, B Conde, MR Mohamed, RJ Dashwood, and Rohit Bhagat. Real-time displacement and strain mappings of lithium-ion batteries using three-dimensional digital image correlation. *Journal of Power Sources*, 271:82–86, 2014.

[77] Ruihe Li, Dongsheng Ren, Dongxu Guo, Chengshan Xu, Xingcun Fan, Zhichao Hou, Languang Lu, Xuning Feng, Xuebin Han, and Minggao Ouyang. Volume deformation of large-format lithium ion batteries under different degradation paths. *Journal of The Electrochemical Society*, 166(16):A4106, 2019.

[78] AJ Louli, LD Ellis, and JR Dahn. Operando pressure measurements reveal solid electrolyte interphase growth to rank li-ion cell performance. *Joule*, 3(3):745–761, 2019.

[79] Katharina Rumpf, Maik Naumann, and Andreas Jossen. Experimental investigation of parametric cell-to-cell variation and correlation based on 1100 commercial lithium-ion cells. *Journal of Energy Storage*, 14:224–243, 2017.

[80] Peyman Mohtat, Jason B Siegel, Anna G Stefanopoulou, and Suhak Lee. UofM Pouch Cell Voltage and Expansion Cyclic Aging Dataset [Data set]. *University of Michigan - Deep Blue*, 2021.

[81] Christoph R Birkl, Matthew R Roberts, Euan McTurk, Peter G Bruce, and David A Howey. Degradation diagnostics for lithium ion cells. *Journal of Power Sources*, 341:373–386, 2017.

[82] Akram Eddahech, Olivier Briat, and Jean-Michel Vinassa. Lithium-ion battery performance improvement based on capacity recovery exploitation. *Electrochimica Acta*, 114:750–757, 2013.

[83] Bernd Epding, Björn Rumberg, Hannes Jahnke, Ina Stradtmann, and Arno Kwade. Investigation of significant capacity recovery effects due to long rest periods during high current cyclic aging tests in automotive lithium ion cells and their influence on lifetime. *Journal of Energy Storage*, 22:249–256, 2019.

[84] Greg Davies, Kevin W Knehr, Barry Van Tassell, Thomas Hodson, Shaurjo Biswas, Andrew G Hsieh, and Daniel A Steingart. State of charge and state of health estimation using electrochemical acoustic time of flight analysis. *Journal of The Electrochemical Society*, 164(12):A2746, 2017.

[85] Y. Kim, N. A. Samad, K. Y. Oh, J. B. Siegel, B. I. Epureanu, and A. G. Stefanopoulou. Estimating state-of-charge imbalance of batteries using force measurements. In *2016 American Control Conference (ACC)*, pages 1500–1505, July 2016.

[86] Madeleine Ecker, Nerea Nieto, Stefan Käbitz, Johannes Schmalstieg, Holger Blanke, Alexander Warnecke, and Dirk Uwe Sauer. Calendar and cycle life study of li (nimnco) o2-based 18650 lithium-ion batteries. *Journal of Power Sources*, 248:839–851, 2014.

[87] Toshiyuki Momma, Mariko Matsunaga, Daikichi Mukoyama, and Tetsuya Osaka. Ac impedance analysis of lithium ion battery under temperature control. *Journal of Power Sources*, 216:304–307, 2012.

[88] Upender Rao Koleti, Truong Quang Dinh, and James Marco. A new on-line method for lithium plating detection in lithium-ion batteries. *Journal of Power Sources*, 451:227798, 2020.

[89] Mathias Petzl, Michael Kasper, and Michael A Danzer. Lithium plating in a commercial lithium-ion battery–a low-temperature aging study. *Journal of Power Sources*, 275:799–807, 2015.

[90] Anup Barai, Kotub Uddin, WD Widanage, Andrew McGordon, and Paul Jennings. A study of the influence of measurement timescale on internal resistance characterisation methodologies for lithium-ion cells. *Scientific reports*, 8(1):1–13, 2018.

[91] Seong Jin An, Jianlin Li, Claus Daniel, Sergiy Kalnaus, and David L Wood III. Design and demonstration of three-electrode pouch cells for lithium-ion batteries. *Journal of the Electrochemical Society*, 164(7):A1755, 2017.

[92] Abraham Savitzky and Marcel JE Golay. Smoothing and differentiation of data by simplified least squares procedures. *Analytical chemistry*, 36(8):1627–1639, 1964.

[93] Zachary J. Schiffer, John Cannarella, and Craig B. Arnold. Strain derivatives for practical charge rate characterization of lithium ion electrodes. *Journal of The Electrochemical Society*, 163(3):A427–A433, dec 2015.

[94] Paul Albertus, Jake Christensen, and John Newman. Experiments on and modeling of positive electrodes with multiple active materials for lithium-ion batteries. *Journal of the Electrochemical Society*, 156(7):A606, 2009.

[95] WB Gu and CY Wang. Thermal-electrochemical modeling of battery systems. *Journal of The Electrochemical Society*, 147(8):2910, 2000.

[96] Valentin Sulzer, S Jon Chapman, Colin P Please, David A Howey, and Charles W Monroe. Faster lead-acid battery simulations from porous-electrode theory: Part i. physical model. *Journal of The Electrochemical Society*, 166(12):A2363, 2019.

[97] S Prussin. Generation and distribution of dislocations by solute diffusion. *Journal of Applied Physics*, 32(10):1876–1881, 1961.

[98] Xiangchun Zhang, Wei Shyy, and Ann Marie Sastry. Numerical simulation of intercalation-induced stress in li-ion battery electrode particles. *Journal of the Electrochemical Society*, 154(10):A910, 2007.

[99] Peyman Mohtat, Jason B Siegel, and Anna G Stefanopoulou. UofM pouch cell voltage and expansion dataset and modeling code [Data set]. *University of Michigan - Deep Blue*, 2020.

[100] Domenico Di Domenico, Anna Stefanopoulou, and Giovanni Fiengo. Lithium-ion battery state of charge and critical surface charge estimation using an electrochemical model-based extended kalman filter. *Journal of dynamic systems, measurement, and control*, 132(6), 2010.

[101] Oleksandr Dolotko, Anatoliy Senyshyn, MJ Mühlbauer, Kristian Nikolowski, and Helmut Ehrenberg. Understanding structural changes in nmc li-ion cells by in situ neutron diffraction. *Journal of Power Sources*, 255:197–203, 2014.

[102] Karen E Thomas and John Newman. Heats of mixing and of entropy in porous insertion electrodes. *Journal of power sources*, 119:844–849, 2003.

[103] W Lu, I Belharouak, D Vissers, and K Amine. In situ thermal study of li1+ x [ni1/ 3co1/ 3mn1/ 3] 1- x o2 using isothermal micro-clorimetric techniques. *Journal of the Electrochemical Society*, 153(11):A2147, 2006.

[104] M Safari and C Delacourt. Modeling of a commercial graphite/lifepo4 cell. *Journal of the Electrochemical Society*, 158(5):A562, 2011.

[105] Lars Ole Valøen and Jan N Reimers. Transport properties of lipf6-based li-ion battery electrolytes. *Journal of The Electrochemical Society*, 152(5):A882, 2005.

[106] M Farkhondeh, M Safari, M Pritzker, M Fowler, Taeyoung Han, Jasmine Wang, and C Delacourt. Full-range simulation of a commercial lifepo4 electrode accounting for bulk and surface effects: A comparative analysis. *Journal of The Electrochemical Society*, 161(3):A201, 2013.

[107] Xiao Guang Yang, Yongjun Leng, Guangsheng Zhang, Shanhai Ge, and Chao Yang Wang. Modeling of lithium plating induced aging of lithium-ion batteries: Transition from linear to nonlinear aging. *Journal of Power Sources*, 360:28–40, 2017.

[108] Ting Cai, Anna G Stefanopoulou, and Jason B Siegel. Modeling li-ion battery temperature and expansion force during the early stages of thermal runaway triggered by internal shorts. *Journal of The Electrochemical Society*, 166(12):A2431, 2019.

[109] Ting Cai, Peyman Mohtat, Anna G. Stefanopoulou, and Jason B. Siegel. Li-ion battery fault detection in large packs using force and gas sensors. *IFAC-PapersOnLine*, 53(2):12491–12496, 2020. 21th IFAC World Congress.

[110] Aaron Knobloch, Chris Kapusta, Jason Karp, Yuri Plotnikov, Jason B Siegel, and Anna G Stefanopoulou. Fabrication of multimeasurand sensor for monitoring of a li-ion battery. *Journal of Electronic Packaging*, 140(3), 2018.

[111] Lisa K Willenberg, Philipp Dechent, Georg Fuchs, Dirk Uwe Sauer, and Egbert Figgemeier. High-precision monitoring of volume change of commercial lithium-ion batteries by using strain gauges. *Sustainability*, 12(2):557, 2020.

[112] Kelsey B Hatzell, Xi Chelsea Chen, Corie L Cobb, Neil P Dasgupta, Marm B Dixit, Lauren E Marbella, Matthew T McDowell, Partha P Mukherjee, Ankit Verma, Venkatasubramanian Viswanathan, et al. Challenges in lithium metal anodes for solid-state batteries. *ACS Energy Letters*, 5(3):922–934, 2020.

[113] Valentin Sulzer, Peyman Mohtat, Antti Aitio, Suhak Lee, Yen T Yeh, Frank Steinbacher, Muhammad Umer Khan, Jang Woo Lee, Jason B Siegel, Anna G Stefanopoulou, et al. The challenge and opportunity of battery lifetime prediction from field data. *Joule*, 2021.

[114] Matthieu Dubarry, George Baure, and Arnaud Devie. Durability and Reliability of EV Batteries under Electric Utility Grid Operations: Path Dependence of Battery Degradation. *Journal of The Electrochemical Society*, 165(5):A773–A783, 2018.

[115] Trishna Raj, Andrew A. Wang, Charles W. Monroe, and David A. Howey. Investigation of Path-Dependent Degradation in Lithium-Ion Batteries. *Batteries & Supercaps*, pages 1–10, 9 2020.